Angular Magnetoresistance Oscillations in the Molecular Organic Conductor (DMET)₂I₃: Experiment and Calculation

Author: Pashupati Dhakal

Boston College
The Graduate School of Arts and Sciences
Department of Physics

ANGULAR MAGNETORESISTANCE OSCILLATIONS IN THE MOLECULAR ORGANIC CONDUCTOR $(DMET)_2I_3$: EXPERIMENT AND CALCULATION

a dissertation by

PASHUPATI DHAKAL

submitted in partial fulfillment of the requirements
for the degree of

Doctor of Philosophy

July, 2010

"This dissertation is based upon work supported by the National Science Foundation under Grant No. 0605339. Any opinions, findings, and conclusions or recommendations expressed in this dissertation are those of the author(s) and do not necessarily reflect the views of the National Science Foundation"

Acknowledgements

The present work could not have been brought to its present level of study without the help, guidance and support of many people. First, I would like to express my deep and sincere gratitude to my supervisor and mentor, Professor Michael J. Naughton. His encouragement, guidance and support, from my first year to the final level of my graduate studies, enabled me to develop a deep and comprehensive understanding of the subject matter, which allowed me to complete my dissertation.

I would also like to thank Professor Harukazu Yoshino from Osaka City University, Japan, for providing samples (synthesized by Koichi Kikuchi, Tokyo Metropolitan University) and his software used for my calculations. His consistent guidance in helping me understand the issues at hand and his computational technique, as well as his willingness to be an external reviewer on my dissertation committee, was a tremendous help to me. Many thanks go to Dr. Jeong Il Oh, as well, for his help during the experimental stages and for teaching me several experimental techniques. Further, I thank Mr. Svet Simidjiyski for his assistance with many mechanical and electrical systems throughout the experiments.

I would like to thank committee members, Professors Michael J. Graf and Willie J. Padilla, for reviewing this dissertation. I also extend my thanks all the faculty members and the members of physics department administration at Boston College, especially Professors Rein Uritam and Kevin Bedell. Although my work in the clean room has not been included in this dissertation, Mr. Steve Shepard and Dr. Greg McMahon were of immense help to me in nano and microfrabication.

I would like to thank to Gisele Byda for initial grammatical correction of this dissertation and Nancy Chevry, for her support and assistance during my time as graduate student. I would like to thank to my lab mates Joydeep, Binod, Tim and Fan as well as friends for making my stay at Boston College so memorable.

I owe my loving thanks to my wife Sangita Khanal, for her support and my special thanks to my brother Ramesh and my sister Sharmila. Lastly, and most importantly, I wish to thank my parents, Tirtha R. Dhakal and Goma D. Dhakal for their unconditional love and support. To them, I dedicate this dissertation.

ANGULAR MAGNETORESISTANCE OSCILLATIONS IN THE MOLECULAR ORGANIC CONDUCTOR $(DMET)_2I_3$: EXPERIMENT AND CALCULATION

By: Pashupati Dhakal

Advisor: Prof. Michael J. Naughton

Abstract

Quasi-one dimensional (Q1D) molecular organic conductors are among the most exciting materials in condensed matter physics, exhibiting nearly every known ground state. They are highly anisotropic, structurally and electronically, and show large oscillatory phenomena in conductivity for magnetic field rotated in different crystalline planes. Several theoretical works have been published to explain these angular magnetoresistance oscillation (AMRO) effects, but the underlying physics remains ill-understood. Here, we present measurements and calculations of magnetotransport in the molecular organic (super)conductor $(DMET)_2I_3$ which detect and simulate all known AMRO phenomena for Q1D systems. Employing, for the first time, the true triclinic crystal structure in the calculations, these results address the mystery of the putative vanishing of the primary AMRO phenomenon, the Lebed magic angle effect, for orientations in which it is expected to be strongest. They also show a common origin for Lebed and so-called "Lee-Naughton" oscillations, and confirm the generalized nature of AMRO in Q1D systems. Furthermore, we report the temperature dependence of the upper critical magnetic field in $(DMET)_2I_3$, for magnetic field applied along the intrachain, interchain, and interplane directions. The upper critical field exhibits orbital saturation at low temperature for field in all directions, implying that superconductivity in $(DMET)_2I_3$ is conventional spin singlet.

Table of Contents

List of Figures

Chapter 1

Introduction

1.1 Molecular Organic Conductors

The study of organic conductors has become an important research area in condensed matter physics, with almost all known electronic and magnetic ground states available [1.1]. By varying temperature, pressure and magnetic field, one can arrange to make a single specimen a superconductor, metal, semimetal, semiconductor, or a correlated insulator, exhibiting single particle, quantum Hall, and sliding density wave transport [1.2]. Organic conductors in this context are crystalline charge transfer salts with carbon-containing (organic) anions and organic or inorganic anions. In general, organic and polymeric compounds have been historically believed to be insulators. The study of conductivity in organic compounds was started almost a century ago by McCoy and Moore [1.3], and Kraus [1.4], if not earlier. These researchers studied a number of amalgams of organic moities and discussed their physical properties, such as crystallinity, metallic luster, and possible electrical conductivity, without making any systematic measurements. In 1948, Eley [1.5] discovered that the electrical conductivity of a number of organic compounds varied exponentially with temperature. Later, Akamatu and Inokuchi [1.6] measured the conductivity of polycrystalline samples of violanthrone and pyranthrone, which followed the same temperature dependence as inorganic semiconductors, namely $\sigma \sim e^{\frac{\Delta}{k_B T}}$ with a semiconducting gap Δ of approximately 0.75 - 1 eV, k_B is Boltzmann constant and T is absolute temperature. In 1960, Kepler *et al.* [1.7]

synthesized a salt of the radical anion formed by an addition of an electron to tetracyanoquinodimethane (TCNQ) [**Fig. 1.1 (a)],** and discovered this had a room temperature conductivity of 100 S/cm.

After the interpretation of superconductivity in inorganic metals by the well-known BCS theory [1.8], Little in 1964 [1.9] proposed the possibility of high temperature superconductivity in linear chain polymers, based on an excitonic mechanism, which depends on the movement of charge along the linear chain of polarizable molecules as shown in **Fig. 1.2**. Thus began the quest for highly conducting molecular superconductors as well as conductors. In the early 1970's, Wudl and co-workers [1.10] synthesized salts of the tetrathiafulvalene (TTF) molecule [**Fig. 1.1 (b)**], and showed they exhibited semiconducting behavior. Shortly thereafter, metallic-like electrical conduction was observed in a well ordered molecular conductor, TTF-TCNQ [1.11, 1.12]. The crystal structure of TTF-TCNQ exhibited stacked segregated columns of donor molecules TTF and acceptor molecules TCNQ. Charge is transferred from donor to acceptor, the amount determined by the overall crystal stability, but typical between 0.5 to 1 electron or hole per molecule. The conductivity of this conductor showed metallic behavior upon cooling down to 60 K, followed by transition to an insulating ground state at low temperature. This discovery opened a vast area for study of conductivity in organic compounds.

(a) (b)

FIG. 1.1 (a) TCNQ and (b) TTF molecule.

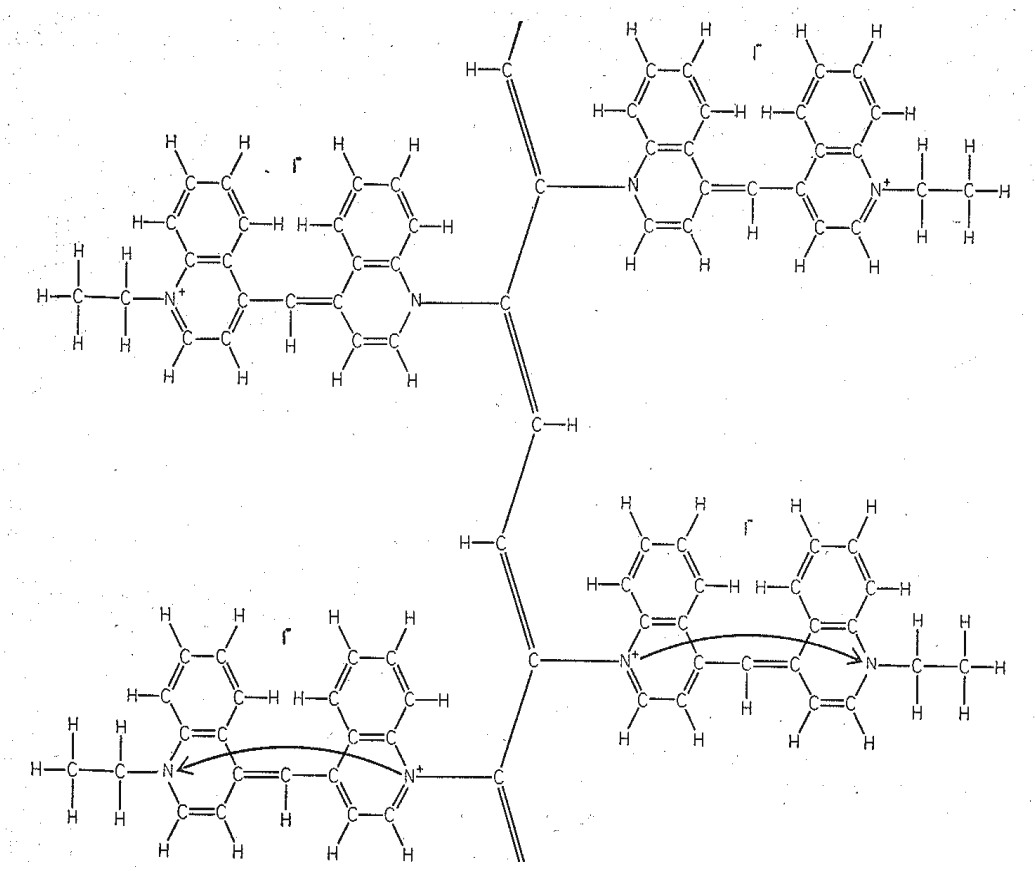

FIG. 1.2 Little's hypothetical superconducting molecule. The molecule is built around a "spine" of carbon atoms connected by alternating single and double bonds. These side-chain molecules are highly polarizable; that is, an electron can move freely from a nitrogen site close to one end of the molecule to another nitrogen site close to the other end [1.13].

In these highly one dimensional systems, for which the term "quasi-one dimensional" (Q1D) term is applied, the conducting state is often found to be unstable against a lattice distortion, which opens an energy gap at the Fermi level. This was almost immediately identified as resulting from a Peierls transition, which until this time was only a theoretical prediction [1.14, 1.15]. The work on organic compounds in the early 1970's suggested that a decrease in Coulomb repulsion between charge carriers boosts

the conductivity of metals [1.16]. The idea to minimize electron-electron interactions and increase electron-phonon interactions, while keeping the overlap between neighboring stacks as large as possible, subsequently led to the synthesis of a new compound, TMTSF-DMTCNQ, which is the tetramethylated derivative of the TSF molecule combined with dimethylated TCNQ. The conductivity of this conductor was found to be quite high ~ 10^5 S/cm at 10 kbar pressure and 1 K [1.17, 1.18, 1.19], comparable to inorganic metals such as Cu, Au, etc.

Following the above work on conducting salts, Jérome and Bechgaard [1.20] succeeded in 1979 in synthesizing the first organic superconductor, $(TMTSF)_2PF_6$ (bistetramethyl-tetraselenafulvalene-hexafluorophosphate). At ambient pressure, this compound undergoes a metal-insulator transition associated with the Peierls transition, into an antiferromagnetic spin density wave (SDW) state. This SDW can be suppressed by pressure, recovering the metallic state, which upon further cooling was found to superconduct at 1.2 K. After the seminal discovery of this first organic superconductor, a series of conducting salts, based on the TMTSF molecule, namely $(TMTSF)_2X$, where X is an inorganic mono-anion with various possible symmetries, such as spherical (PF_6, AsF_6, SbF_6, TaF_6), tetrahedral (BF_4, ClO_4, ReO_4) or triangular (NO_3), were synthesized [1.21]. Of these, only the compound $(TMTSF)_2ClO_4$ exhibited superconductivity at ambient pressure, with T_c = 1.4 K [1.22]. In addition, the basic building block, TMTSF, has itself been modified to make other types of molecular organic conductors and superconductors, such as $(TMTTF)_2X$ (S replacing Se) and $(BEDT\text{-}TTF)_2X$ [1.23]. To date, there have been more than one hundred organic superconductors synthesized.

Finally, the non-symmetrical donor DMET (dimethylethylenedithio-diselenadithiafulvalene), which is a hybrid of TMTSF and BEDT-TTF, yielded several superconductors $(DMET)_2X$, where X = I_3, IBr_2, $AuBr_2$, AuI_2 [1.24]. The conducting and superconducting properties of one of these molecular organic conductors $(DMET)_2I_3$, which superconduct at T_c = 0.58 K at ambient pressure, is the primary subject of this thesis.

1.2 Crystal and Band Structure of Q1D Systems

In the tight binding band approximation [1.25], the electron band energy for a three dimensional system can be written as

$$E(k) = -2t_x \cos(k_x a_x) - 2t_y \cos(k_y a_y) - 2t_z \cos(k_z a_z) \qquad (1.1)$$

where k_x, k_y and k_z are wave vectors along the lattice directions a_x, a_y and a_z, respectively, and t_x, t_y and t_z are transfer (wave function overlap or hoping) integrals along these directions, respectively. The shape of the momentum-space Fermi surface (FS) of a metal with this dispersion relation is governed by the magnitudes and relative ratios of these transfer integrals. For three dimensional (3D) isotropic conductors, this ratio is $t_x : t_y : t_z \sim 1 : 1 : 1$, which in its simplest form gives a spherical FS, as shown in **Fig. 1.3 (a)**. When the transfer integral in one direction is smaller than those in the other two directions (*i.e.*, $t_x \sim t_y > t_z$), the FS distorts in such a way that it looks ellipsoidal [**Fig. 1.3 (b)**]. For further decreases in t_z relative to t_x and t_y, the FS becomes multiply connected across Brillouin zones, and the surface is open at both ends within a given zone [**Fig. 1.3 (c)**]. If, in addition to this biaxial asymmetry, the transfer integrals have uniaxial asymmetry such that $t_x > t_y > t_z$, the FS further disturbs, as shown in **Fig. 1.3 (d)**. In the

highly anisotropic case of $t_x >> t_y >> t_z$, the FS consists of a pair of warped open surfaces, now multiply-connected in both transverse directions k_y and k_z, as shown in **Fig 1.3 (e).** This is the characteristic Fermi surface of a Q1D molecular conductor. Finally, if we consider the perfect one-dimensional (1D) conductor ($t_y = t_z = 0$), the FS is a pair of parallel sheets extended to infinity as shown in **Fig. 1.3 (f)**.

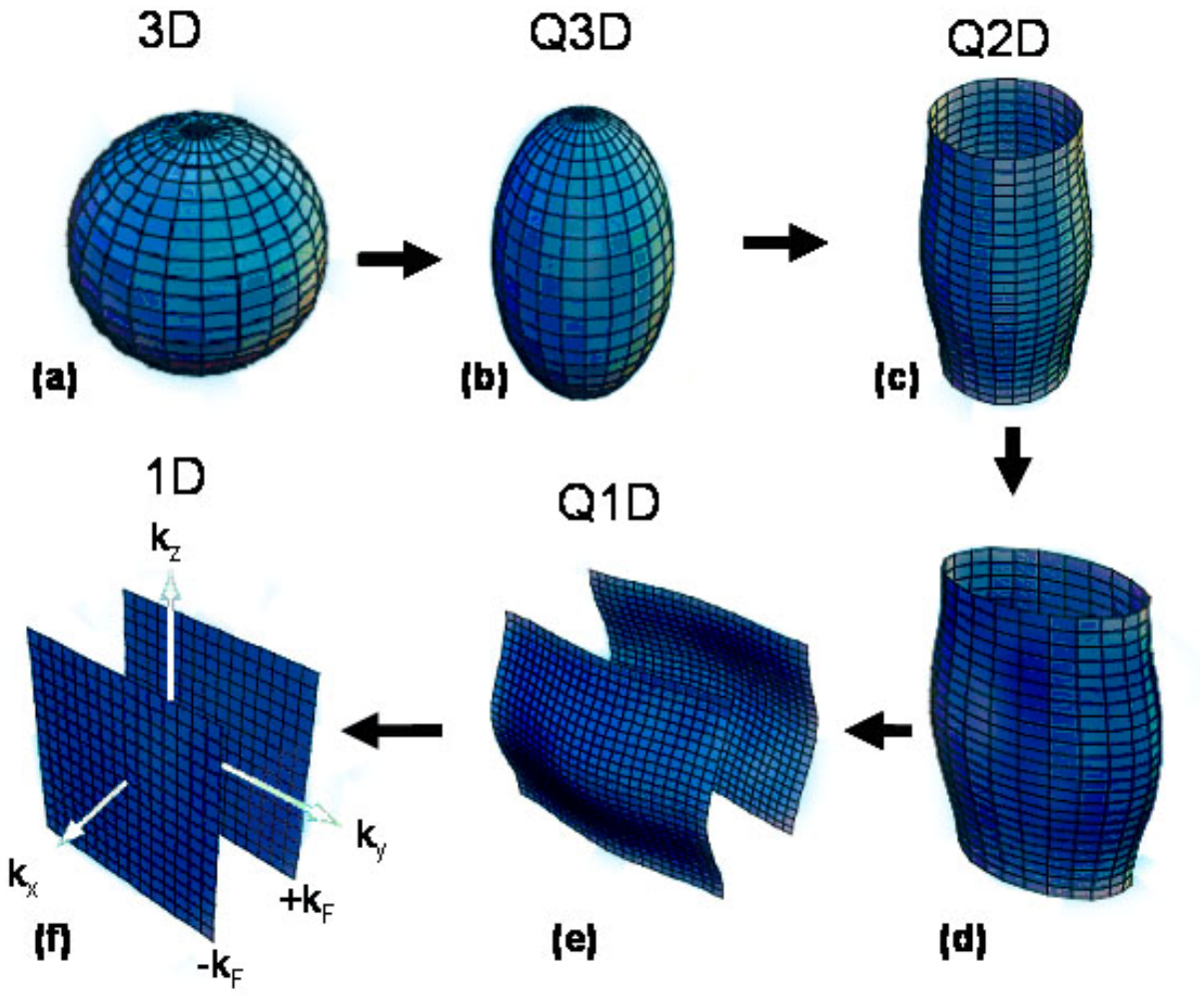

FIG. 1.3 The evolution of a Fermi surface in its first Brillouin zone for a conductor by varying the magnitude of tight-binding transfer integrals. For the isotropic three-dimensional (3D) conductor, the Fermi surface is spherical (**a**). For different transfer integrals, the Fermi surface is ellipsoidal for Q3D (**b**), cylindrical for Q2D (**c**) and (**d**), and a warped pair of Fermi surface sheets for Q1D (**e**). For a completely one dimensional solid ($t_y = t_z = 0$), the Fermi surface is an infinite pair of sheets extended along the *y* and *z*- directions (**f**).

In real space, the building blocks of organic molecular conductors are arranged in linear chains, planes, or stacks of chains and planes. The interactions between the chains or planes are different for different compounds and the resulting electrical conduction in these conductors is also different. In some cases, the electrical conduction takes place, principally, along unique crystalline directions. In Q1D molecular organic conductors, the interactions within the chains are much stronger than those between adjacent chains, which are in torn stronger than between the planes. A schematic diagram is shown in **Fig. 1.4**.

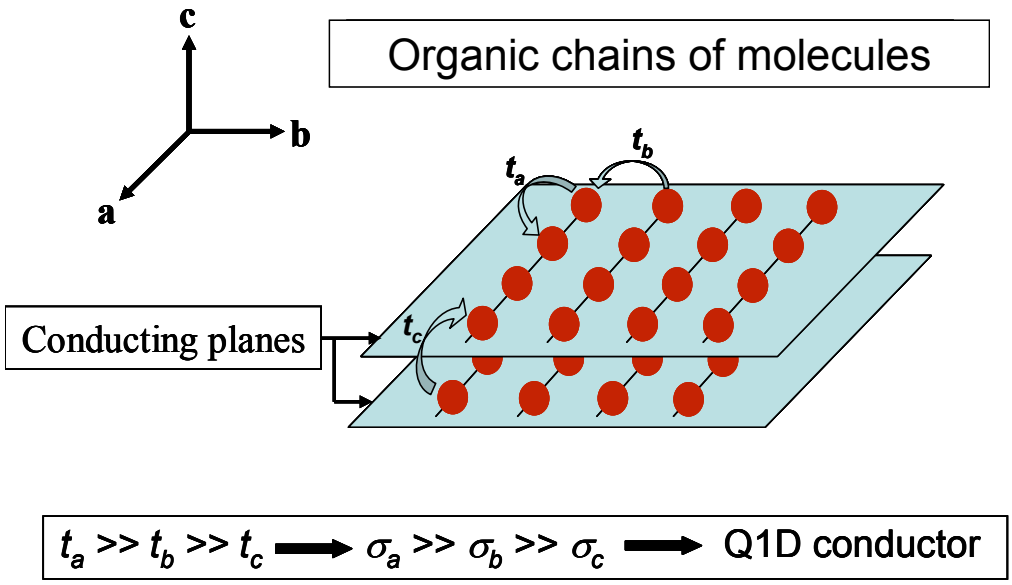

FIG. 1.4 The schematic diagram of organic compound forming the chains and planes. The conductivity of the compound is proportional to the interaction in the chain (t_a), between the chains (t_b) and between the planes (t_c), in their respective directions. In Q1D systems $t_a >> t_b >> t_c$ give the $\sigma_a >> \sigma_b >> \sigma_c$.

In case of $(TMTSF)_2X$, each of the carbon and selenium atom has a perpendicular π-orbital which form the molecular π structures such that all the p-electrons of the molecules are delocalized. The overlap of these orbital along a-direction form a σ-bond, which is responsible for the high conduction along the a-direction. The relatively smaller overlaps along the b and c-directions leads to finite but reduce electron (hole) conduction in these directions. As a result, with $t_a >> t_b >> t_c$, the conductivity scales as $\sigma_i \sim t_i^2$.

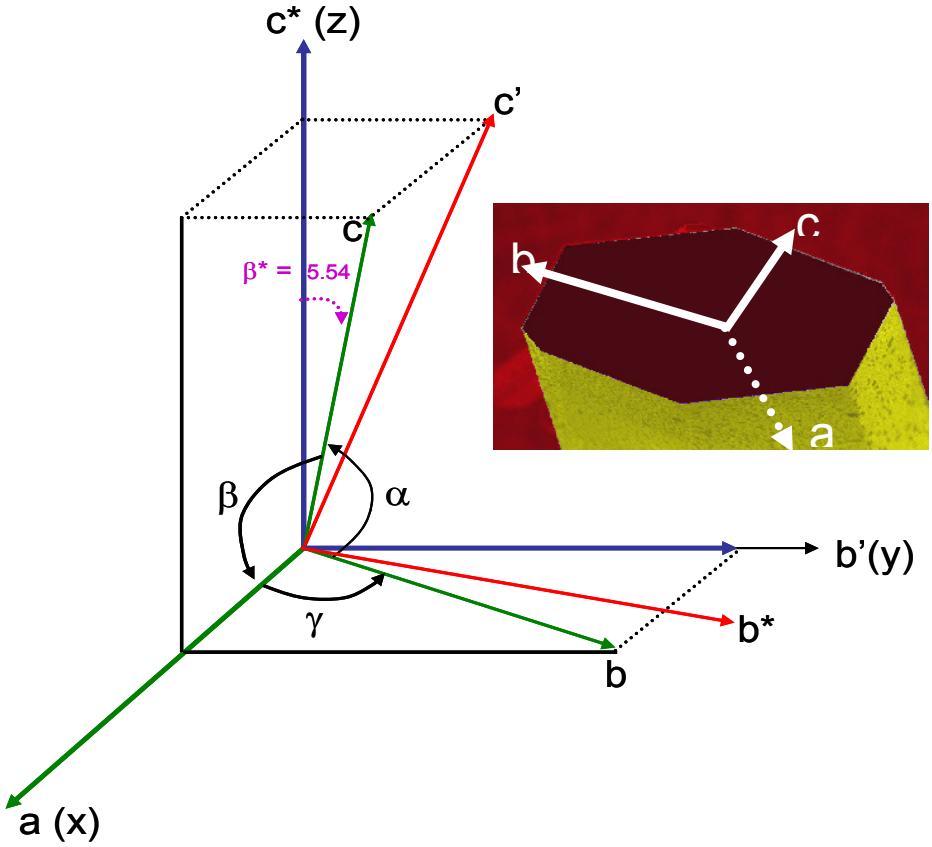

FIG. 1.5 A schematic diagram showing all axes and directions in triclinic $(TMTSF)_2X$. Here, ***b′ (c′)*** is the projection of ***b*** ***(c)*** onto the plane perpendicular to the ***a***-axis, and ***b**** ***(c*)*** is perpendicular to both the ***a*** and ***c***-axes (***a*** and ***b***-axes), in the conventional definition of reciprocal space vectors. Note that the angle between ***b′*** and ***b**** ***(c′ and c*)*** is 5.54° for $(TMTSF)_2ClO_4$ .The inset scanning electron microscope images of a single crystal of $(TMTSF)_2ClO_4$.

Q1D molecular organic conductors as discussed herein are thus highly anisotropic structurally and electronically, with the crystals structures that are triclinic, meaning $\alpha \neq \beta \neq \gamma \neq 90^o$ and $a \neq b \neq c$ (α, β and γ are unit cell angles). **Figure 1.5** depicts a schematic diagram showing all axes and directions in a triclinic system. In **Fig. 1.5**, the triclinic crystallographic axes *a, b* and *c* are transformed to *a, b'* and *c** in a Cartesian coordinate systems, which are then parallel to the *x, y* and *z*-axes. In this transformation, $a \rightarrow a$, $b \rightarrow b' = b\sin\gamma$ and $c \rightarrow c^* = c \sin\alpha \sin\beta^*$ where $\beta^* = \cot^{-1}\{(\cos\gamma\cos\alpha - \cos\beta)/(\sin\alpha \sin\gamma)\}$.

In the case of $(TMTSF)_2X$, the conduction band is three-fourths-filled (or a quarter-filled hole band) with a reduced Brillouin zone of approximate size $(2\pi)^3/(a_s b_s c_s)$, where $a_s = a/2$, $b_s = b$ and $c_s = c$. The dimerization of the TMTSF molecules along the chains is represented by $a_s = a/2$, which opens a gap at the zone boundary, $k_x = \pm \pi/a$, and splits the band into two HOMO (highest occupied molecular orbital) bands per Brillouin zone leaving the upper band half-filled as shown in **Fig. 1.6**.

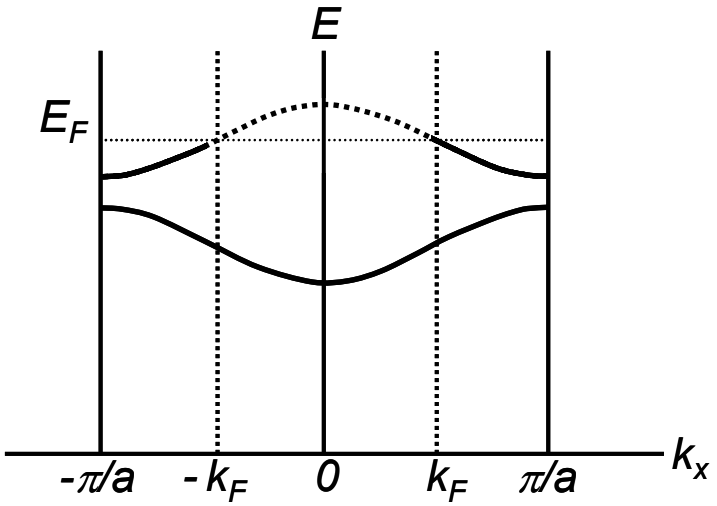

FIG. 1.6 Band structure of Q1D system in the chain direction. The dimerization opens up a gap at the zone boundary ($k_x = \pm \pi/a$). The upper band becomes a half filled.

1.3 Electrical Conductivity in Q1D Systems

Prerequisites for the formation of a molecular conductor are, first, having charged molecules in a solid state system, and second, allowing these charges to delocalize between molecular entities [1.26]. Charging the molecules is achieved by charge transfer reactions. The physical properties of these molecular conductors depend greatly on the amount of charge transferred, δ, between the constituent donor (D) and acceptor (A) molecules:

$$A + D \rightarrow A^{-\delta} + D^{+\delta}$$

and/or on the charge distribution within a conducting column. In case of the $(TMTSF)_2X$ salts, the inorganic anion *X* is singly charged, and owing to the 1:2 stoichiometry, δ = ½ hole per donor molecule. Since there is only one independent anion in this unit cell, each TMTSF molecule receives the same charge, but this may change at low temperature if the material undergoes a phase transition to a superstructure. In TMTSF, the electron transfer energies along the, *b* and *c* directions are estimated to be 0.25, 0.025 and 0.0015 eV, respectively. **Figure 1.7** show the temperature-dependent resistivity of first organic superconductor the resistivity of sample shows metallic behavior on cooling and it goes to SDW transition around 12 K, for all three directions $(TMTSF)_2PF_6$ in ambient pressure. However, the sample goes to superconducting transition at higher pressure. As discussed earlier, the electrical conducting takes place due to the overlap of π orbital of organic molecules forming σ -bond. Furthermore, the resistivity measurement shows the electrical anisotropy, characteristic of Q1D conductors.

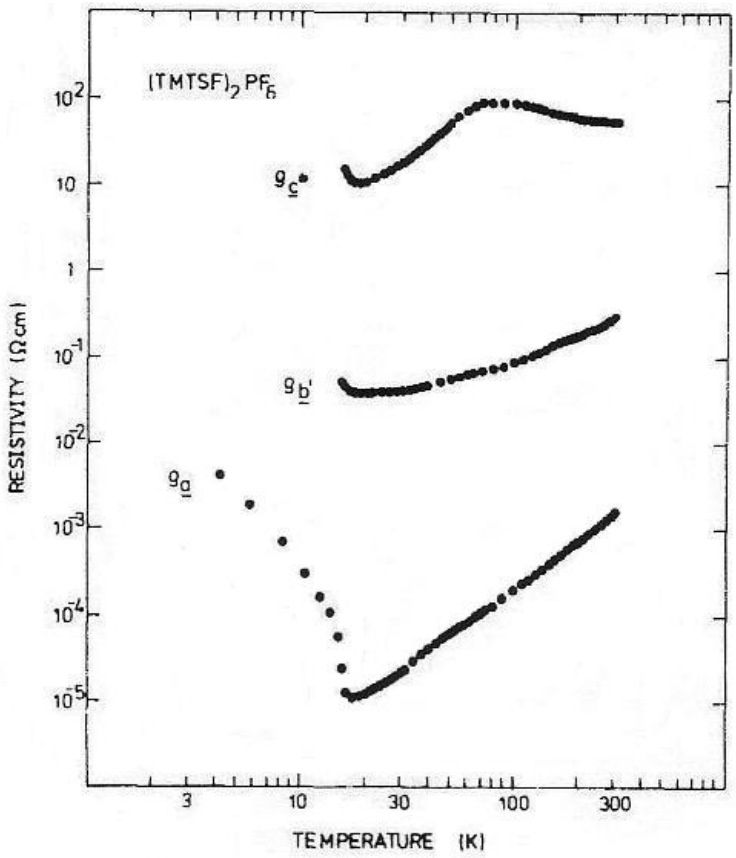

FIG. 1.7 Temperature dependence of resistivity components ρ_{xx} (a-axis) ρ_{yy} (*b*-axis) ρ_{zz} (*c*-axis) of $(TMTSF)_2PF_6$.. The resistivity varies widely from one another along the three principal axes with the lowest resistivity along *a*-axis and highest along *c*-axis [1.27].

As mentioned, $(TMTSF)_2X$ compounds are materials in which a nominally quarter-filled band is created by charge delocalization on the organic chain. At low temperature, the ground state can be insulating, metallic or superconducting. The origin of the insulating ground state is closely related to the choice of anion *X*. In the case of centrosymmetric anions, such as PF_6, AsF_6, and SbF_6, the ground state is due to the formation of a spin density wave phase at $T_{SDW} \sim 12$K. In compounds with non-centrosymmetric anions, such as ClO_4, ReO_4, FSO_3 and BF_4, a metal-to-insulator phase

transition occurs, driven by an ordering of the anions. A generalized temperature-pressure phase diagram for this class of materials is shown in **Fig. 1.8**. Depending upon the temperature and pressure, each compound shows a different ground states, such as spin Peierls (SP), spin density wave (SDW), and superconducting (SC).

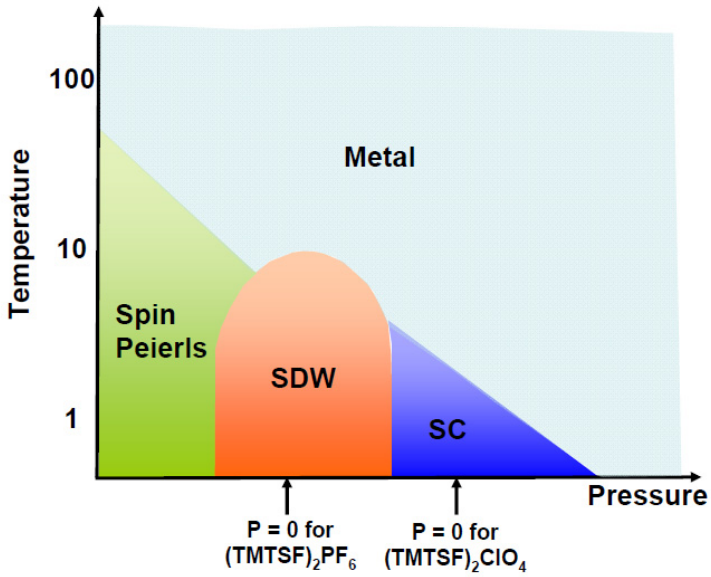

FIG. 1.8 Temperature-pressure (*T*-*P*) phase diagram of $(TMTSF)_2X$ salts.

1.4 Ground States and Instabilities in Q1D Systems

In low-dimensional systems, transitions to many ground states are observed, such as Peierls instabilities, charge-density-waves, spin-Peierls instabilities, antiferromagnetic states, spin-density-waves and singlet and possibly triplet superconductivity states. These ground states are affected by the topology of the Fermi surface. In the case of a strictly 1D Fermi surface, any point on one sheet of Fermi surface can be mapped to the other sheet by the wave vector $Q = 2k_F$, known as a nesting vector. Due to this nesting, correlations of electrons on the FS become divergently strong, leading to a divergence at the response function (dielectric function or susceptibility or phonon dispersion relation)

phenomenon known as the Kohn anomaly. As a result, the electron-phonon interaction becomes divergently strong at the nesting vector $Q = 2k_F$ with decreasing temperature, leading to a soft phonon mode at $Q = 2k_F$ as shown in **Fig. 1.9**. This soft phonon frequency goes to zero at low temperature, resulting in a static lattice distortion with $Q = 2k_F$, called the Peierls distortion, at a temperature T_P. For temperatures $T > T_P$, the system is metallic, and for $T < T_P$, the system is insulating. In other words, the Peierls transition leads to a metal-insulator transition in low-dimensional systems, destroying the high temperature 1D FS. The Peierls transition also can leads to the modulation of charge density, known as a charge density wave state. A similar type of distortion can happen in the electron spin system, known as an SDW state, which is a type of weak antiferromagnetism. **Table 1** summarizes the typical behavior of 1-D instabilities in organic conductors.

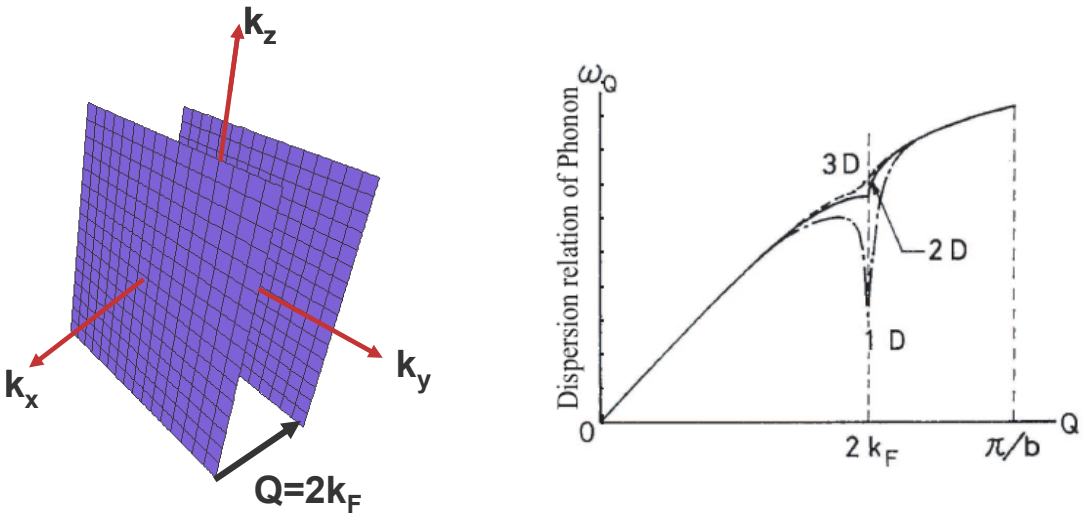

(a) (b)

FIG 1.9 Peierls instability in a 1D system. (a) The FS is represented by a pair of open FS sheets. Any points on one FS can be mapped into the other FS by a single wave vector $Q = 2k_F$, the so-called nesting vector. (b) Kohn anomalies in 1, 2 and 3 dimensional system [1.28].

Table 1 Typical behavior of one-dimensional instabilities in organic conductors

	Peierls (CDW)	**SDW**	**Spin-Peierls (S-P)**
Wave Vector	$2k_F$	$2k_F$	$2k_F$
Lattice distortion	Yes	No	Yes
Interaction	Electron-phonon	Spin-spin	Spin-phonon
Ground state	Nonmagnetic	Antiferromagnetic	Nonmagnetic
Susceptibility	$T > T_P$: Pauli $T < T_P$: activated	$T > T_c$: Pauli $T < T_c$: anisotropic	$T > T_{SP}$: Pauli $T < T_{SP}$: activated
ESR	$\Delta H_{PP(max)}$ at T_P	ΔH_{PP} diverges at T_c	$\Delta H_{PP(max)}$ at T_{SP}
T_1^{-1}	$T > T_P$: ≈ Korringa $T < T_P$: activated	Diverges at T_c	$T > T_{SP}$ ≈ Korringa $T < T_{SP}$: activated
Examples	TTF-TCNQ $(Per)_2[M(mnt)_2]$, M = Cu, Co	$(TMTSF)_2PF_6$	$(BCPTTF)_2PF_6$ $(BCPTTF)_2AsF_6$ MEM-TCNQ

The nesting of the FS is suppressed in the presence of external pressure, but it has been shown to be able to be re-induced by a magnetic field (H), a phenomenon known as the field induced spin density wave. **Figure 1.10** shows the field-temperature-pressure phase diagram of $(TMTSF)_2PF_6$. Here, the SDW transition temperature decreases under increasing pressure and superconductivity appears above 6 kbar. Above a critical pressure around 6 kbar, the cascade of FISDW transitions is observed above a finite threshold field. The initial threshold field increases from 4.5 T at 8 kbar to 8T at 16 kbar pressure. When the magnetic field is applied perpendicular to the highly conducting *ab*-plane, the electron motion tends to be confined to the chains (*a*). For high magnetic field, the width of the electron trajectories between chains becomes smaller and, eventually, the electron trajectory is confined to the Q1D chains, leading to the strong nesting of FS [**Fig. 1.11**].

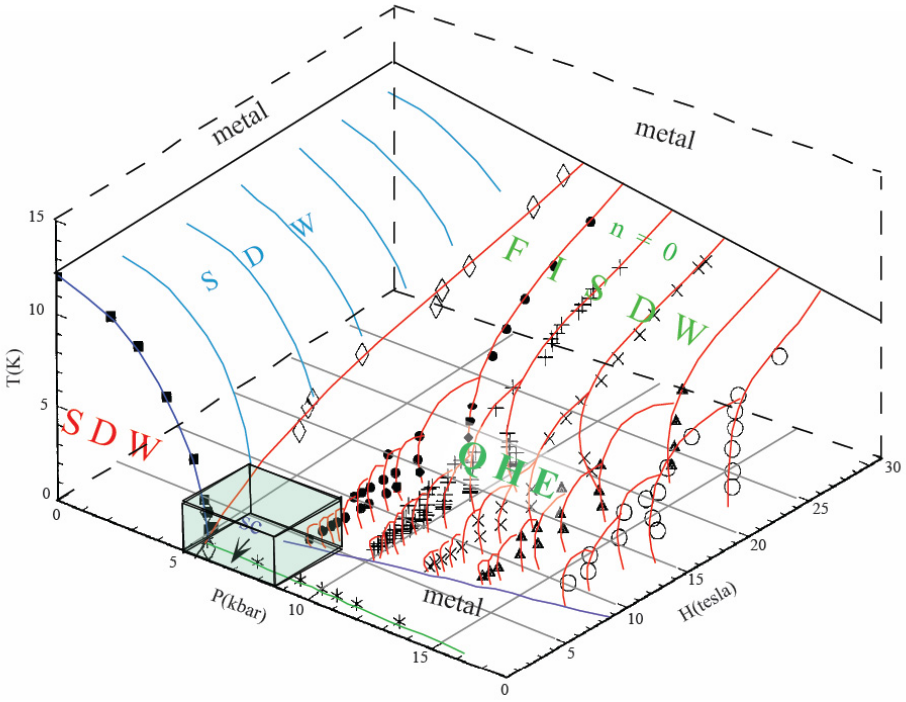

FIG 1.10 T-H-P phase diagram for $(TMTSF)_2PF_6$. The FISDW phase is observed in high magnetic field. The FISDW effect is caused by the field dependent nesting (confinement) effect on the *ab*-plane [1.29].

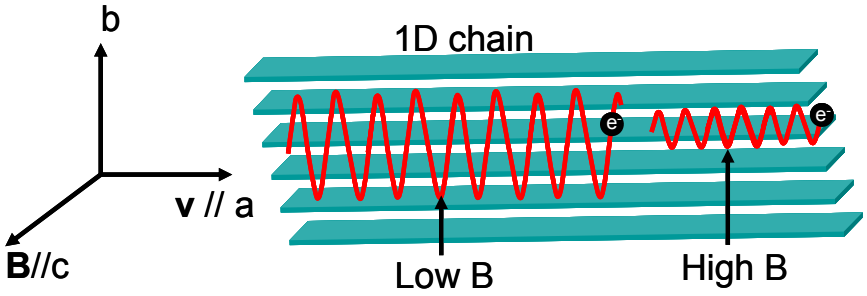

FIG.1.11 Illustration of the confinement effect on the trajectories of electron in a magnetic field. Upon increasing the magnetic field, the transverse width of the trajectories of electrons decreases. This results in an increase in the one-dimensional properties, (*i.e.,* the nesting on the FS becomes stronger).

In the presence of a magnetic field, one can define a magnetic reciprocal lattice vector *G,* and FS nesting can occur at $Q = 2k_F \pm nG$, where *n* is an integer. This leads to a cascade of FISDW transitions, as this new quantum number *n* takes on high values for small field and decreases to the conventional SDW with $n = 0$ at very high field. Due to this quantization, the Hall resistance is also quantized within each FISDW sub-space as experimentally observed in $(TMTSF)_2X$ ($X = ClO_4$ and PF_6) [1.30, 1.31, 1.32].

1.5 $(DMET)_2I_3$

The non-centrosymmetric molecule dimethyldiselenadithiafulvalene (DMET) is formed by combining half of a tetramethyl-tetraselenafulvalene **(**TMTSF) molecule and half of a bis-ethylenedithio-tetrathiafulvalene (BEDT-TTF) also called ET molecule [**Fig. 1.12**]. The TMTSF and the ET ends have different thicknesses, due to the difference in the Van der Waals radii of the constituent atoms. To produce face-to-face stacks, successive molecules must be rotated 180˚ relative to one another. The salt $(DMET)_2I_3$ consists of two donor molecules and three acceptor anions, forming conducting sheets in the *a*-*b* plane which in turn are separated by layers of anions along the *c*-axis. The highest conductivity in DMET is along the *b*-direction, which is the chain direction. The lattices parameters are $a = 6.699$ Å, $b = 7.761$ Å and $c = 15.776$ Å, $\alpha = 89.96^o$, $\beta = 81.81^o$ and $\gamma = 78.19^o$ [3.33]. The band structure is considered to have a pair of Fermi surfaces spread along the $k_a k_{c^*}$ plane (*i.e.* the *b*-axis is the most conducting axis) shown in **Fig 1.2 (e)**.

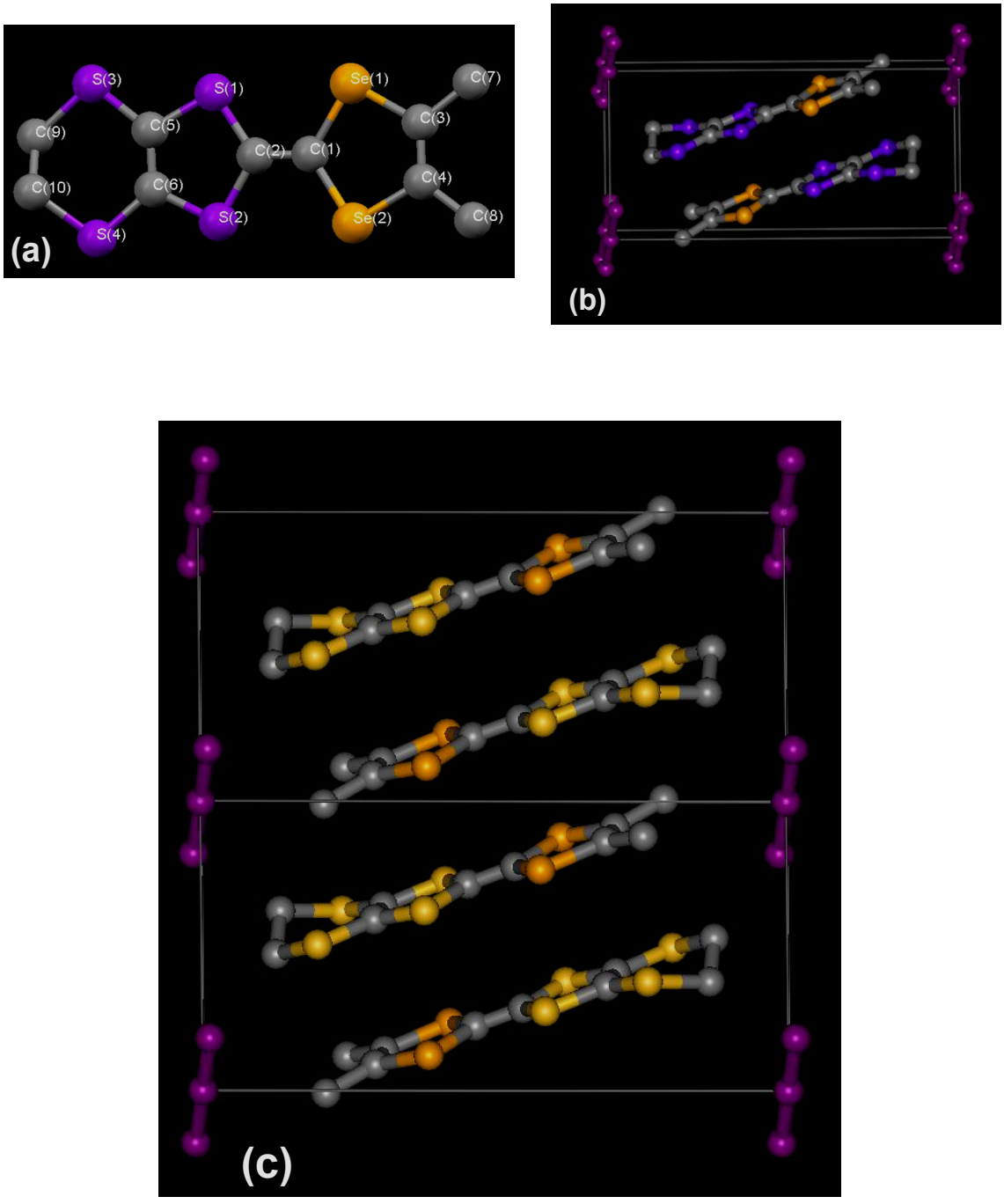

FIG. 1.12 (a) Single DMET molecule. The right half of the molecule resembles the TMTSF structure and the left half is the BEDT-TTF (ET) structure. (b) DMET molecules in a unit cell. The molecules are rotated 180˚ relative to one another to produce a planar stack because of the different thickness on the TMTSF and the ET sides. (c) Crystal structure of $(DMET)_2I_3$ viewed along the *a* axis.

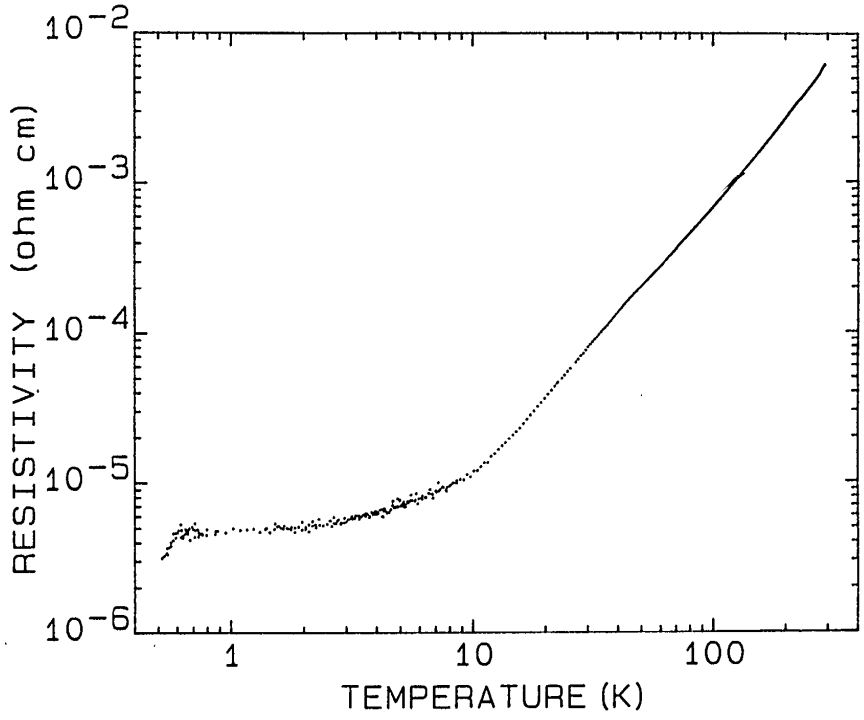

FIG. 1.13 Temperature dependence of resistivity of $(DMET)_2I_3$ showing an onset of superconductivity [1.24].

The DMET salts $(DMET)_2X$ show a rich variety of electron transport properties, ranging from insulator to superconductor, which are classified into five groups. The ones with octahedral anions X = PF_6, AsF_6 exhibit semiconducting behavior with room temperature conductivity in the range of 200 to 300 S/cm. Those with tetrahedral anions like BF_4, ClO_4, ReO_4 have typical room temperature conductivities of ~100 S/cm and show a metal-insulator transition at around 40 K. Salts with gold dihalide anions like $AuCl_2$, AuI_2, and $Au(CN)_2$ have a room temperature conductivity of 230 S/cm and exhibit metallic behavior down to low temperature, before showing a weak increase in resistance below 3K to undergo a superconducting transition. The salts with linear anions like I_3, I_2Br, IBr_2, SCN and $AuBr_2$ have conductivities of 170, 320, 210, and 80 S/cm

respectively. Among these, $(DMET)_2I_3$ and $(DMET)_2IBr_2$ exhibit superconductivity under ambient pressure. **Figure 1.13** shows the temperature dependent resistivity of $(DMET)_2I_3$. It showed the indication of superconducting transition ~ 0.58 K. The clear superconducting transition has been observed in our present work and it will be discussed in Chapter 4.

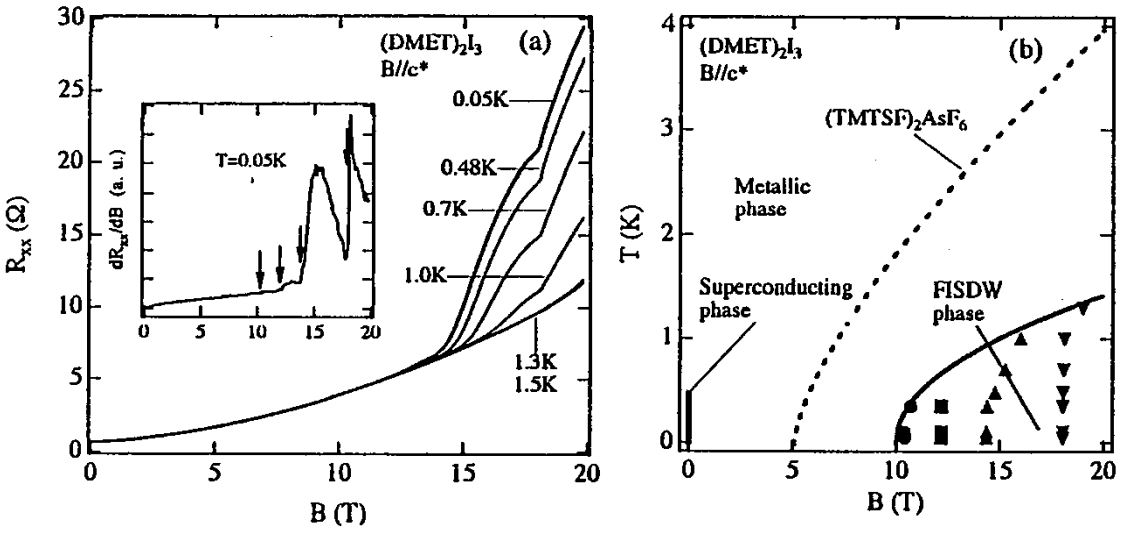

Fig. 1.14 (a) The magnetic field dependence of resistance *(R_{xx})* for the field B//c* at various temperature (inset shows the derivative of data at $T = 0.05$ K). The kink in resistance was observed for the field strength higher then 10 T showing the FISDW transition. (b) The temperature-field *(T-H)* phase diagram for $(DMET)_2I_3$ for *B//c**. The FISDW phase was observed with the threshold field of 10 T. The dotted line was the phase diagram for $(TMTSF)_2AsF_6$ for the direct comparison of FISDW transition [taken from Uji, *et al.*, 1.34]

The study of FISDW in $(DMET)_2I_3$ was carried out by Uji *et al.*, [1.34] for the magnetic field perpendicular to the conduction plane *(B//c*)* showed that the FISDW phases are induced by the magnetic field higher then 10T, which is much higher than in $(TMTSF)_2X$ family of Q1D systems. The magnetic field dependence resistance for *B//c**

at different temperature is shown in **Fig 1.14 (a)** and the temperature-field phase diagram is shown in **Fig. 1.14 (b)**. It showed that the frequency of the successive transitions in about 70T for $(DMET)_2I_3$, smaller than that of $(TMTSF)AsF_6$, which is 83T. It was also found that FISDW transition roughly corresponds to the Shubhnikov-de-Haas frequency of the small pocket formed by the imperfect nesting. Thus, the FS nesting for $(DMET)_2I_3$ is found to be more perfect than that for $(TMTSF)_2AsF_6$.

1.6 Angular Effects in Conductivity

As discussed earlier, the Fermi surfaces of Q1D conductors are open and warped, so conventional Landau quantization is not possible in the presence of magnetic field. This Landau orbital quantization effect is known to lead to large oscillatory effects, such as Shubnikov-de Haas and de Haas-van Alphen effects, which themselves are used as tools to measure the structure of Fermi surfaces. However, in the metallic phase of these Q1D conductors, several other types of magnetoresistance oscillations have been observed experimentally, which are related not to the orbital quantization, but to the shape of Q1D Fermi surfaces. To date, Lebed magic angle resonances [1.35, 1.36, 1.37, 1.38, Danner-Kang-Chaikin (DKC) oscillations [1.40] and the Yoshino angular effect (YAE) [1.41, 1.42], have been observed, in particular, for field rotations about the three principal axes. In addition, more complex oscillations are observed when the magnetic field is rotated through arbitrary (out-of-plane) directions [1.43, 1.44]. These have been refereed to in the literature as Lee-Naughton (LN) oscillations after their discoverers. **Figure 1.15** shows the orientations of magnetic field for which these remarkable AMRO phenomena have been observed.

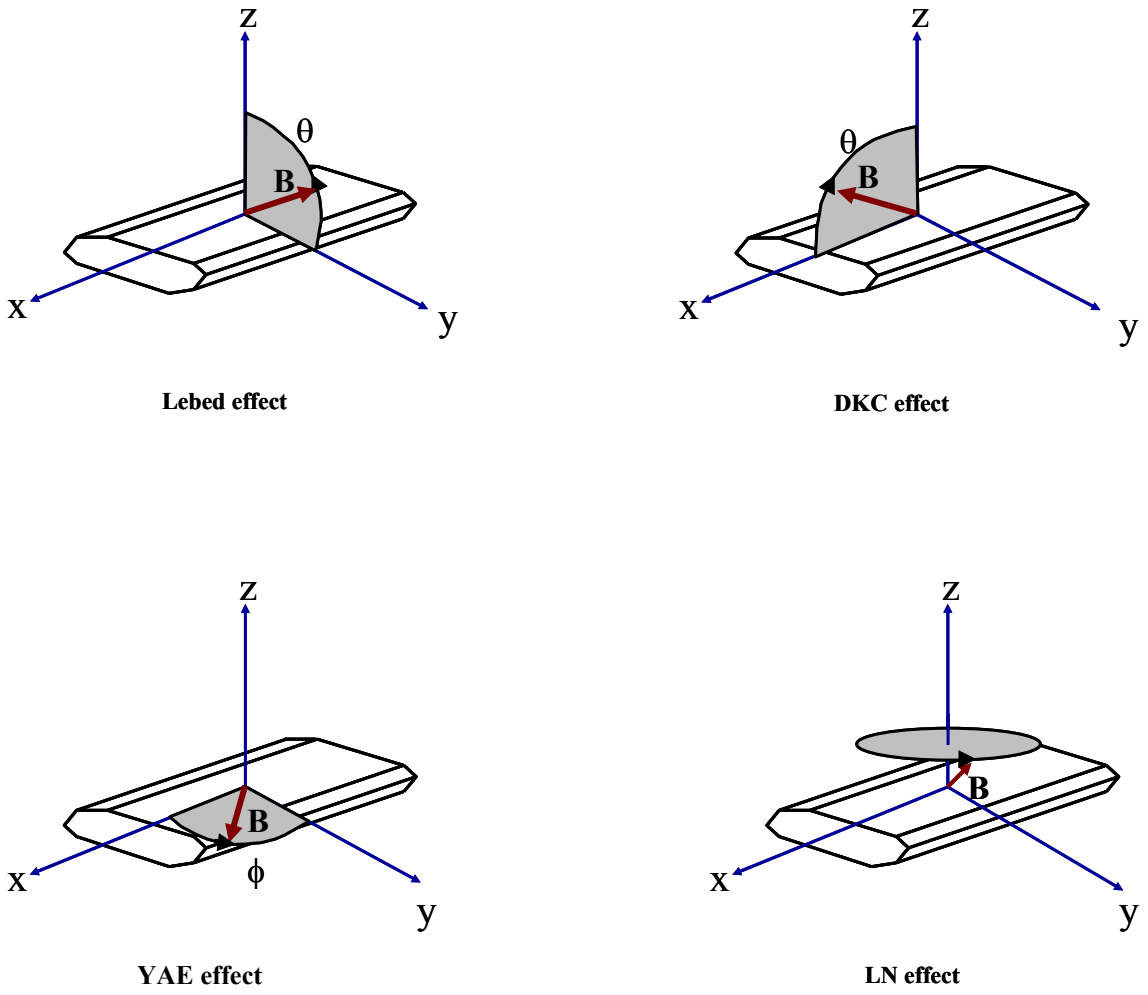

FIG. 1.15 The schematic diagram for the rotation of magnetic field in different plane for which AMRO has been observed. From top left in clockwise direction; Lebed effect (*y*-*z* rotation), DKC (*x*-*z* rotation), YAE (*x*-*y* rotation), and LN (out-of-plane rotation).

While such AMRO effects have been observed in many Q1D materials, their origin(s) and relationships to each other have puzzled researchers for over two decades. This topic is important enough in this thesis that it requires a separate chapter to fully elaborate. AMRO effects will thus be discussed in Chapter 2. Chapter 3 discusses the details of the experimental setup. Chapter 4 discusses the results of experiments on $(DMET)_2I_3$, comparison to available theoretical models, and simulations electrical conductivity and magnetoresistance using the true triclinic crystal structure. In Chapter 5, the superconductivity in $(DMET)_2I_3$ and measurement of its upper critical field will be presented and discussed.

1.7 References

[1.1] T. Ishiguro, K. Yamaji, and G. Saito, *Organic Superconductors*, 2nd Edition, Springer Verlag, (1998).

[1.2] S. E. Brown, P. M. Chaikin, and M. J. Naughton. *The Physics of Organic Superconductors and Conductors*, edited by A. G. Lebed, Springer, 2008.

[1.3] H. N. McCoy and W. C. Moore, J. Am. Chem. Soc. **33**, 273 (1911).

[1.4] H. J. Kraus, J. Am. Chem. Soc. **34**, 1732 (1913).

[1.5] D. D. Eley, Nature, **162**, 819 (1948).

[1.6] H. Akamatu and H. Inokutchi, J. chem. Phys. **18**, 810 (1950).

[1.7] R. G. Kepler, P. E. Bierstedt, and R. E. Merrifield*.,* Phys. Rev. Lett. **5**, 503 (1960).

[1.8] J. Bardeen, L. N. Cooper, and J. R. Schrieffer., Phys. Rev., **108**, 1175 (1957).

[1.9] W. A. Little, Phys. Rev. **134**, A1416 (1964).

[1.10] F. Wudl, D. Wobschall, and E. J. Hufnagel, J. Am. Chem. Soc., **94**, 670 (1972).

[1.11] J. Ferraris, D. O. Cowan, V. Walatka, Jr., and J. H. Perlstein, J. Am. Chem. Soc, **95**, 948 (1973).

[1.12] L. B. Coleman, M. J. Cohn, D. J. Sandman, F. G. Yamagishi, A. F. Garito and A. J. Heeger, Solid State Commun., **12**, 1125 (1973).

[1.13] W. A. Little, Sci. Am.,**212**, 21 (1965).

[1.14] R. E. Peierls, *Quantum Theory of Solids*, Clarendon, Oxford (1955).

[1.15] H. Frohlich, Proc. R.Soc. London **A223**, 296 (1954).

[1.16] W. A. Little, *Organic Conductors: Fundamentals and Applications*, edited by Jean-Pierre Farges, Marcel Dekker Inc. NY, 1994.

[1.17] J. R. Andersen, K. Bechgaard, C. S. Jacobsen, G. Rindorf, H. Soling, and N. Thorup, Acta Crys., **B34**,1901 (1978).

[1.18] A. Anderieux, P. M. Chaikin, C. Duroure, D. Jerome, C. Weyl, K. Bechgaard, and J. R. Andersen, J. Phys. Paris, **40**, 1199(1779).

[1.19] J. L. Galigne, B. Liautard, S. Peytavin, G. Brun, J. M. Fabre, E. Torreilles, and L. Giral, Acta Crystallogr. B, **34**, 620(1978).

[1.20] D. Jérome, A. Mazaud, M. Ribault, and K. Bechgaard, J. de Physique Lett. **41**, L95 (1980).

[1.21] K. Bechgaard, C. S. Jacobsen, K. Mortensen, H. J. Pedersen, and N. Thorup, Solid State Commun. 33, 1119-1125 (1980).

[1.22] K. Bechgaard, K. Carneiro, M. Olsen, F. B. Rasmussen, and C. S. Jacobsen, Phys. Rev. Lett. **46**, 852 (1981).

[1.23] G. Saito, T. Enoki, K. Toriumi and H. Inokuchi, Solid State Commun. **42**, 557 (1982).

[1.24] K. Kikuchi, *K*. Murata, Y. Honda, T. Namiki, *K*. Saito, *K*. Kobayashi, T. Ishiguro and I. Ikemoto, J. Phys. Soc. Jpn. **56**, 3436 (1987).

[1.25] N. W. Ashcroft and N. D. Mermin, *Solid State Physics*, Brooks Cole; 1st edition (1976)

[1.26] P. Auban-Senzier and D. Jerome, Synth. Met. **133**, 1, 1236 (1981).

[1.27] C. S. Jacobsen, K. Mortensen, M. Weger, and K. Bechgaard, Solid State Commun., **38**, 423 (1981).

[1.28] S. Kagoshima, Jpn. J. Appl. Phys. **20**, 1617 (1981).

[1.29] W. Kang, S.T. Hannahs, and P. M. Chaikin, Phys. Rev. Lett. **70**, 3091 (1993).

[1.30] S. T. Hannahs, J. S. Brooks, W. Kang, L. Y. Chiang, and P. M. Chaikin*.,* Phys. Rev. Lett. **63**, 1988 (1989).

[1.31] J. R. Cooper, W. Kang, P. Auban, G. Montambaux, D. Jerome, and K. Bechgaard*,* Phys. Rev. Lett. **63**, 1984 (1989).

[1.32] H. Cho and W. Kang, Phys. Rev. **B59**, 9814 (1999).

[3.33] Y. Oshima, M. Kimata, K. Kishigi, H. Ohta, K. Koyama, M. Motokawa, H. Nishikawa, K. Kikuchi, and I. Ikemoto, Phys. Rev. B **68**,054526 (2003).

[1.34] S. Uji, C. Terakura, T. Terashima, H. Aoki, H. Nishikawa, I. Ikemoto, and K. Kikuchi*, Proceeding of Physical Phenomena at High Magnetic Fields III* (World Scientific, London, 1998), p 227.

[1.35] A.G. Lebed, JETP Lett. **43**, 174 (1986).

[1.36] T. Osada, A. Kawasumi, S. Kagoshima, N. Miura, and G. Saito, Phys. Rev. Lett. **66**, 1525 (1991).

[1.37] M. J. Naughton, O. H. Chung, M. Chaparala, X. Bu, and P. Coppens, Phys. Rev. Lett. **67**, 3712 (1991).

[1.38] W. Kang, S. T. Hannahs, and P. M. Chaikin, Phys. Rev. Lett. **69**, 2827 (1992).

[1.40] G. M. Danner, W. Kang, and P. M. Chaikin, Phys. Rev. Lett. **72**, 3714 (1994).

[1.41] H. Yoshino, K. Saito, K. Kikuchi, H. Nishikawa, K. Kobayashi, and I. Ikemoto, J. Phys. Soc. Jpn. **64**, 2307 (1995).

[1.42] T. Osada, S. Kagoshima, and N. Miura., Phys. Rev. Lett. **77**, 5261 (1996).

[1.43] I.J. Lee and M. J. Naughton, Phys. Rev. B **57**, 7423 (1998).

[1.44] H. I. Ha, A. G. Lebed, and M. J. Naughton, Phys. Rev. B **73**, 033107 (2006).

Chapter 2

Angular Magnetoresistance Oscillations in Q1D Organic Conductors

2.1 Introduction

The effect of a magnetic field on the physical properties of solids, especially on their electrical conductivity, started as a field of research when William Thompson (later Lord Kelvin) discovered in 1856 that the resistance of iron and nickel changed when placed in a magnetic field [2.1]. The resistivity of iron increases when the magnetic field is applied along the direction of current. Such changes in resistance (increase or decrease) with magnetic field are referred to as magnetoresistance. Theoretically, the conductivity σ of solids in the free electron model is directly proportional to the density of carriers n and in the relaxation time approximation, inversely proportional to a constant scattering time τ. When the magnetic field B is applied, charge carriers experiences a Lorentz force such that electron trajectories bend their paths into helices, with a angular velocity given by the cyclotron frequency $\omega_c=eB/m$, where e is electronic charge. The average angle turned between collisions is $\omega_c\tau$ and, unless $\omega_c\tau > 1$, no significant magnetoresistance effects are expected. However $\omega_c\tau >1$ is not the only requirement to observe magnetoresistance.

Magnetic field is also known to be a useful tool in exploring the Fermi surface (FS) of conductors, especially metals [2.2]. When a strong magnetic field is applied in a conductor, Landau quantization of electron orbits gives rise to oscillations of the Fermi energy and thus various thermodynamic properties, such as heat capacity, magnetization, sound velocity, and electrical conductivity. This is essentially a macroscopic realization

of the Bohr-Summerfield quantization of action $\oint pdq = n\hbar$, where p is momentum; dq is line element along the close path, n in an integer.

In the presence of perpendicular magnetic field, the orbit of an electron quantized in such a way that

$$\oint pdq = \frac{e}{c}\Phi = 2\pi n\hbar \tag{2.1}$$

where $\Phi = 2\pi\hbar c / e$ = 4.14 x 10^{-7} gauss cm^2, is the flux unit, and n is an integer corresponds to the Landau Level.

When the magnetic field is increases, the Landau level approaches an extremal cross-section of Fermi surfaces A_F and then the free energy increases to a maximum. On further increase in field, the highest Landau level with n becomes depleted, causing a sudden decrease of the free energy. The free energy then increases again until the next maximum is reached. The maximum occur whenever the area of orbit is equal to A_F, which is equally spaced with intervals periodic in 1/B,

$$\Delta\left(\frac{1}{B}\right) = \frac{2\pi e}{\hbar}\frac{1}{A_F} = \frac{1}{A_F\Phi} \tag{2.2}.$$

This quantization lead to the remarkable magneto-oscillations in in resistivity and magnetization are referred to as the Shubnikov-de Haas (SdH) and de Haas-van Alphen (dHvA) effects, respectively. Experimental methods to detect these effects are used to explore the FS of conventional metals. The first observation of such oscillations in the magnetization and resistivity, were seen in three-dimensional (3D) metal (semi-metal) bismuth in 1930 [2.3 and 2.4]. Also, when a magnetic field is applied perpendicular to the plane of a two-dimensional electron gas (2DEG), Landau quantization gives rise to quantization of the transverse resistivity of the system, yielding the integer quantum Hall

Effect (QHE) [2.5]. Under special conditions where there are strong correlations between electrons in a 2DEG, another related quantizing phenomenon occurs called the fractional quantum Hall effect (FQHE) [2.6].

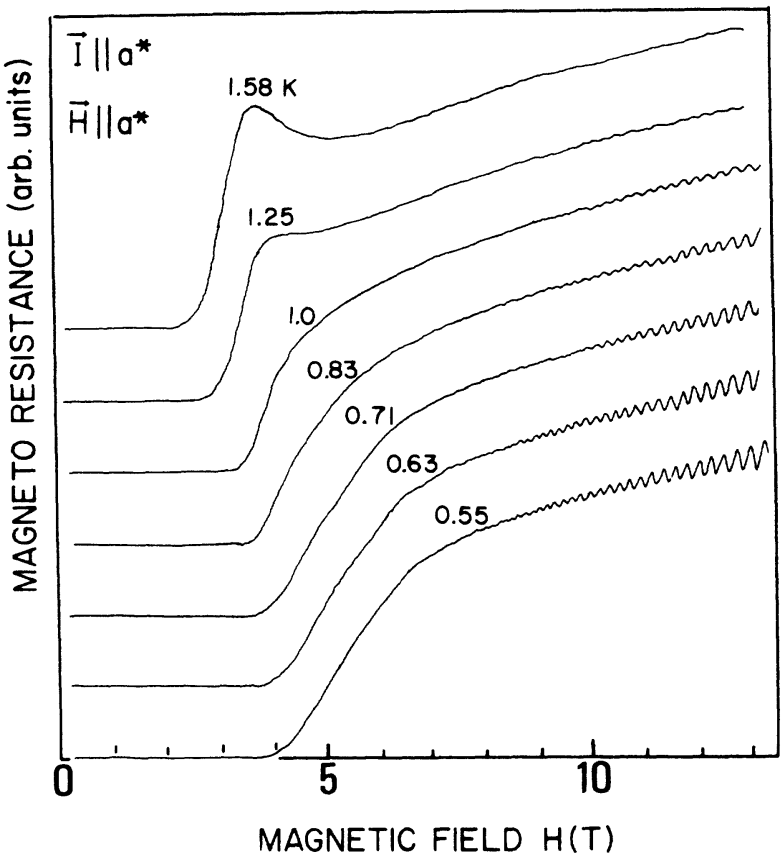

FIG. 2.1 The magnetoresistance of κ-$(ET)_2Cu(NCS)_2$ as a function of magnetic field. Clear SdH oscillations are observed at temperature below 1K and higher magnetic field [2.7].

A prerequisite for the application of magnetic field techniques for the study FS properties of conductors is high crystal quality. This requirement is fulfilled most explicitly by the expression $\omega_c \tau >> 1$, meaning an electron is able to complete several cyclotron orbits before scattering. Due to the self selecting nature of growth process, crystals of molecular organic conductors can be of high qualities, with low defect and

impurity concentrations and the requirement $\omega_c \tau >> 1$, is often easily met. An example of SdH oscillations in an organic conductor κ-$(ET)_2Cu(NCS)_2$, reported by Oshima *et al.* in 1988, is shown in **Fig. 2.1** [2.7]. SdH and dHvA oscillations observed in κ-$(ET)_2I_3$ as shown in **Fig. 2.2** [2.8].

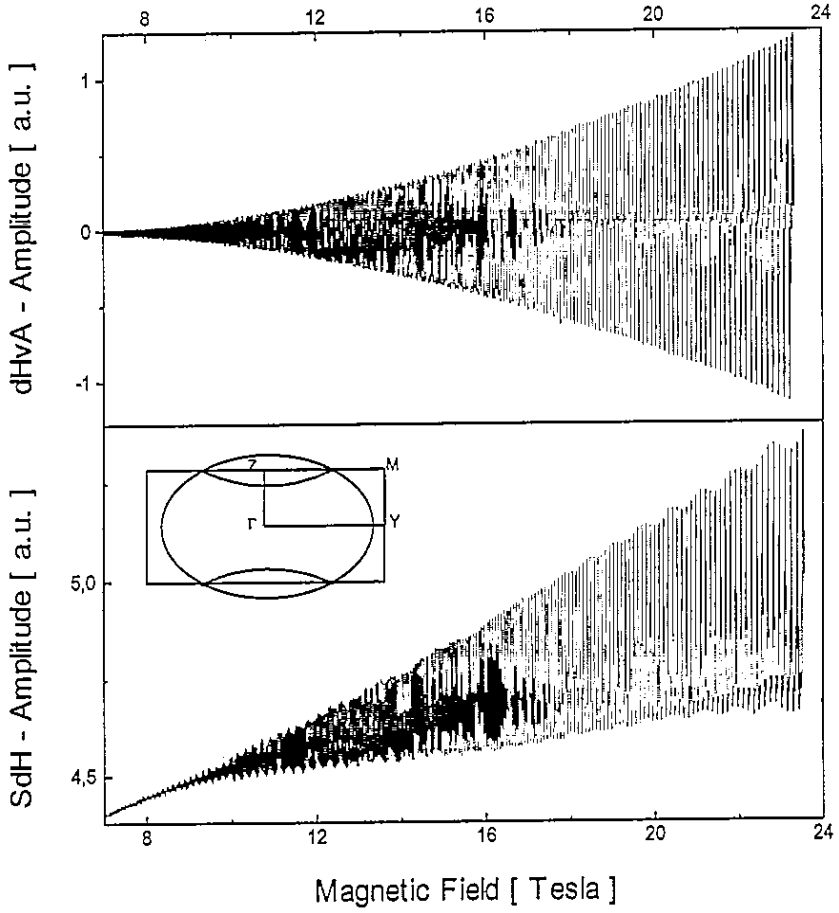

FIG. 2.2 Typical dHvA (top) and SdH (bottom) oscillations of a single crystal of κ-$(ET)_2I_3$ at 0.5 K in the magnetic field range 7 - 23.5 T ; inset: FS of κ-$(ET)_2I_3$ [2.8].

In addition to these orbital quantization-based magnetic oscillations, another kind of oscillation in magnetoresistance is observed in certain crystalline materials when they are rotated in a strong magnetic field. In fact, it can be said that there are two distinct

classes of such angular magnetoresistance oscillations (AMRO), depending on the dimensionality of the crystals. For Q2D systems, Katrsovnik *et al.*, [2.9] observed the magnetoresistance oscillate as a magnetic field is rotated in a plane perpendicular to the most conducting plane as shown in **Fig. 2.3 (a)**. It was soon thereafter noted that the angles where minima in magnetoresistance occurred were well defined by the relation $\tan\theta = sN$ (s = 0.39 and N = 0,1, 2, 3…..). Immediately, these oscillations were explained by Yamaji [2.10] in terms of semi-classical electron orbits in the reciprocal lattice in a magnetic field. They are now generally known as Yamaji oscillations. Again, Landau quantization of these close orbits gives rise to increases in magnetoresistance, but now only in the vicinity of certain angles due to the vanishing of electron group velocity along the field direction. Based on this analysis, the transverse cross section of the FS of the Q2D organic conductor β-(BEDT-TTF)$_2$IBr$_2$ was obtained as shown in **Fig. 2.3 (b).**

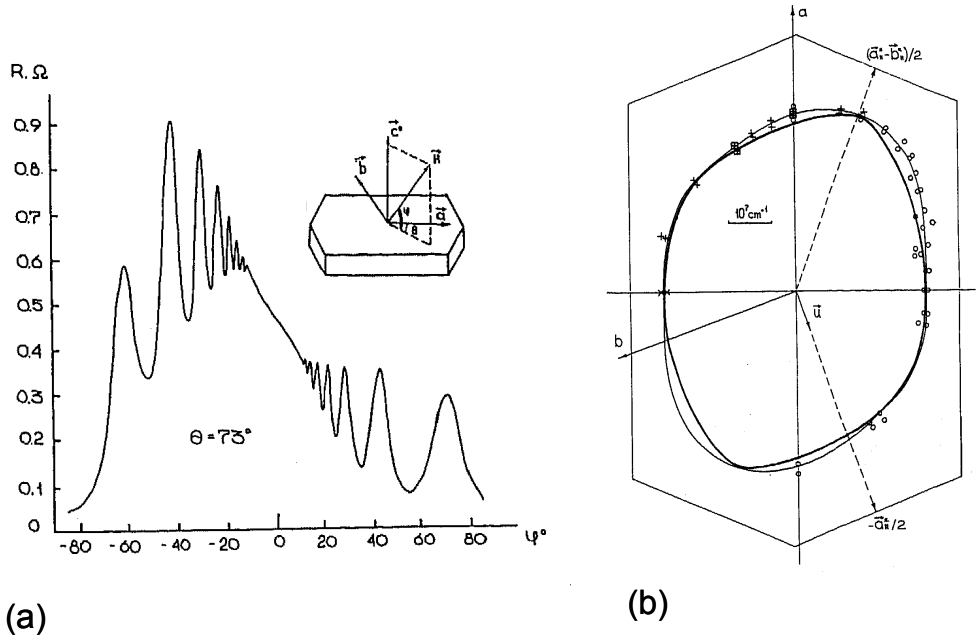

FIG. 2.3 (a) Angle dependence magnetoresistance oscillation (AMRO) in β-(ET)$_2$IBr$_2$. (b) Transverse cross-section of the Fermi surface (thick line) deduced from the angular magnetoresistance oscillations [from Kartsovnik *et al.,* 2.9]

The conductor under study in this thesis, $(DMET)_2I_3$, belongs to the other class of materials exhibiting AMRO effects, beside Q2D systems, that of the layered, quasi one-dimensional conductors. Its FS consists of a pair of corrugated sheets that are open in the plane of the layers as shown in **Fig. 1.2 (e)**. This unique characteristic of the FS leads to new features in magnetoresistance, as compared to 2D and 3D FS's, which are closed surfaces. Those Q1D molecular conductors are highly anisotropic materials, leads to the presence of a remarkable number of oscillatory magnetoresistance phenomena with respect to magnetic field orientation [2. 11]. For examples, Lebed magic angle resonances (LMA) [2.12, 2.13, 1.14, 2.15, 2.16, 2.17], Danner-Kang-Chaikin (DKC) oscillations [2.18] and the Yoshino angular effect (YAE) [2.19 and 2.20], have been observed for field rotations about the three principle axes, *a//x*, *b'//y* and $c^*//z$, respectively. In addition, more complex Lee–Naughton (LN) oscillations have been observed when the magnetic field is rotated through arbitrary (out-of-plane) directions [2.21, 2.22, and 2.23].

In this Chapter, we will discuss these four AMRO effects, models developed to explain them, and their relationships to each other.

2.2 Lebed Magic Angle (LMA) Oscillations

The study of the orientation dependence of a magnetic field on the conductivity of Q1D molecular organic conductors started in the early 1980's. Measurements of the magnetoresistance anisotropy in $(TMTSF)_2ClO_4$ and $(TMTSF)_2PF_6$ showed dramatic deviations from a simple sinusoidal behavior that might be due to the three-dimensional effects, even though the interplane integral t_c is very small [2.24, 2.25, 2.26]. However,

in 1986 Lebed showed that in a tilted magnetic field, the electron motion in the *y*-*z* plane is quasiperiodic, and a type of low dimensional limit is reached *i.e.,* for the fields for which the cyclotron frequency $\omega_c = eB/mc$ exceeds the band with, $\hbar\omega_c \geq 4t_c$. This corresponds to the limit where the amplitude of electron motion along the *z*- direction becomes smaller than the lattice parameter *c* [2.12]. Lebed's original paper contradicted on the effects that this tilted field would have the threshold field for which metal-FISDW transitions. It predicted that at certain "magic" angles give by $\tan\theta = \frac{p}{q}\frac{b}{c}$ where *p* and *q* are integers; *b* and *c* are lattice parameters, these fields would collapse to zero, meaning the electronic system was susceptible to a Fermi surface unstable in any finite magnetic field. The experimental search of such an effect was performed by the Yan, Naughton and others in the Chaikin group at Princeton [2.27]. They studied the angular dependence of FISDW states, as well as the frequency of the unexplained so-called rapid magnetic oscillations in the $(TMTSF)_2ClO_4$. As B was rotated away from the *z*-axis, the transition field positions and the oscillation frequency were found increased, exhibiting conventional $1/\cos\theta$ behavior expected for an anisotropic electronic system, verifying both effects were orbital and two dimensional in nature. However, no evidence for nonmonotonic behavior of the threshold field with angle was found (though in retrospect, it may have been present) for the angular range the experiment was performed.

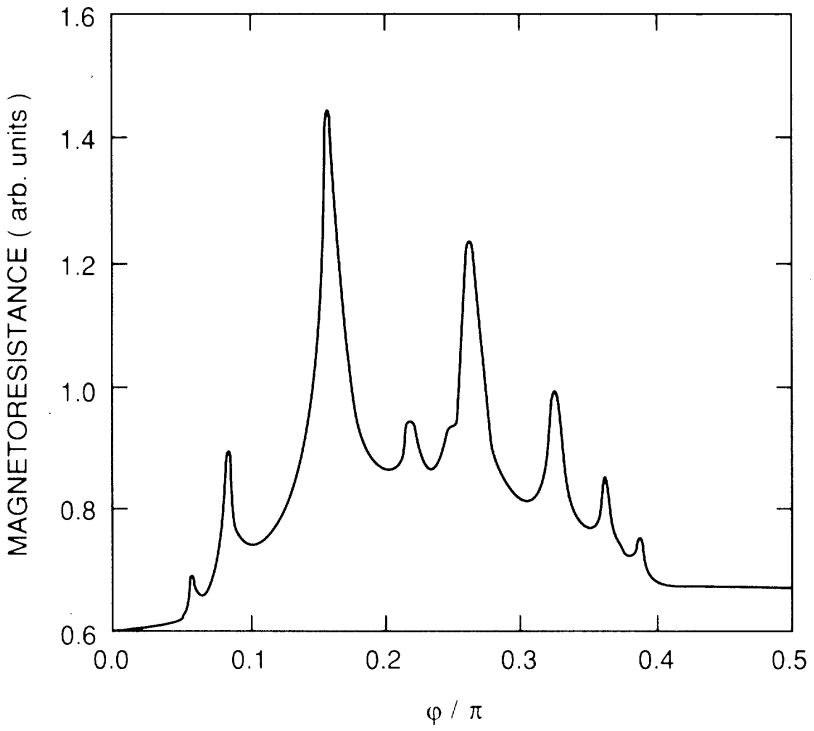

FIG. 2.4 Angular dependence of magnetoresistance calculated by Lebed and Bak for the magnetic field rotating in the *y-z* plane at B = 4T and at temperature 0.2K [2.28].

Shortly thereafter (1989) Lebed and Bak, showed that the quasiperiodic motion of electrons leads to a complicated angular dependence of the magnetoresistance in the *normal* state of Q1D conductors as shown in **Fig 2.4** [2.28]. They calculated that the magnetoresistance has prominent peaks at certain angles (magic angle) given by the same equation as the Lebed predicted for FISDW states,

$$\tan\varphi = \frac{p}{q}\frac{b}{c^*}\sin\gamma \qquad (2.3)$$

Boebinger *et al.* [2.29] reported oscillations in the transverse magnetoresistance in $(TMTSF)_2ClO_4$ in both the metallic and FISDW phases. In the metallic phase, the magnetoresistance varied as B^{α}, where $\alpha < 2$ and decreasing as the magnetic field was

tilted from the *z*- axis. In the FISDW states, there was an enhancement of the magnetoresistance anomalies at the FISDW phase transitions as the magnetic field was tilted, with particular angles for stronger and weaker enhancement. However, there was no clear correlation between these results and Lebed's or Lebed and Bak's predictions.

Further experimental search for features in magnetoresistance at certain magic angles were observed on the Bechgaard salt $(TMTSF)_2ClO_4$ followed by Naughton *et al*. and [2.13. 2.14] Osada *et al.* [2.15]. Each group found magnetoresistance minima, however, rather then the maxima predicted by Lebed. **Figure 2.5** shows the initial results from both groups. It is thought that, at these magic angles, the periods of electron orbits along the k_y and k_z directions on an open FS sheet are commensurate, as shown in **Fig 2.6**. The electrons have non-zero average velocity along the direction of the field at these special angles, which leads to an increase in conductivity along the field direction. As a result, when the magnetic field is rotated from the *y* to the *z*-axis, a series of minima in the interlayer resistance is expected at those angles. These angles for a triclinic system are given by $\tan\theta = \frac{p}{q}\frac{b\sin\gamma}{c\sin\alpha\sin\beta^*} + \cot\beta^*$ (2.4)

p and *q* are an integer, and β^* is give by $\cos\beta^* = \frac{\cos\gamma\cos\alpha - \cos\beta}{\sin\alpha\sin\gamma}$, in which θ denotes the angle that the magnetic field makes from the z-direction, α, β, γ, *b* and *c* are the lattice parameters.

A similar effects has since been found in several other Q1D organic conductors, such as $(TMTSF)_2PF_6$ [2.30, 2.31], $(TMTSF)_2ReO_4$ [2.32], $(DMET\text{-}TSeF)_2X$ ($AuCl_2$, AuI_2, I_3) [2.33, 2.34,2.35], $(DMET)_2CuCl_2$ [2.36], $(DMET)_2I_3$ [2.17], and (BEDT-

TTF)(TCNQ) [2.37]. In general, it seems that effects are seen at integral values of the ratio p/q = 0, 1, 2, 3, …… *i.e.*, p = integer and q = 1.

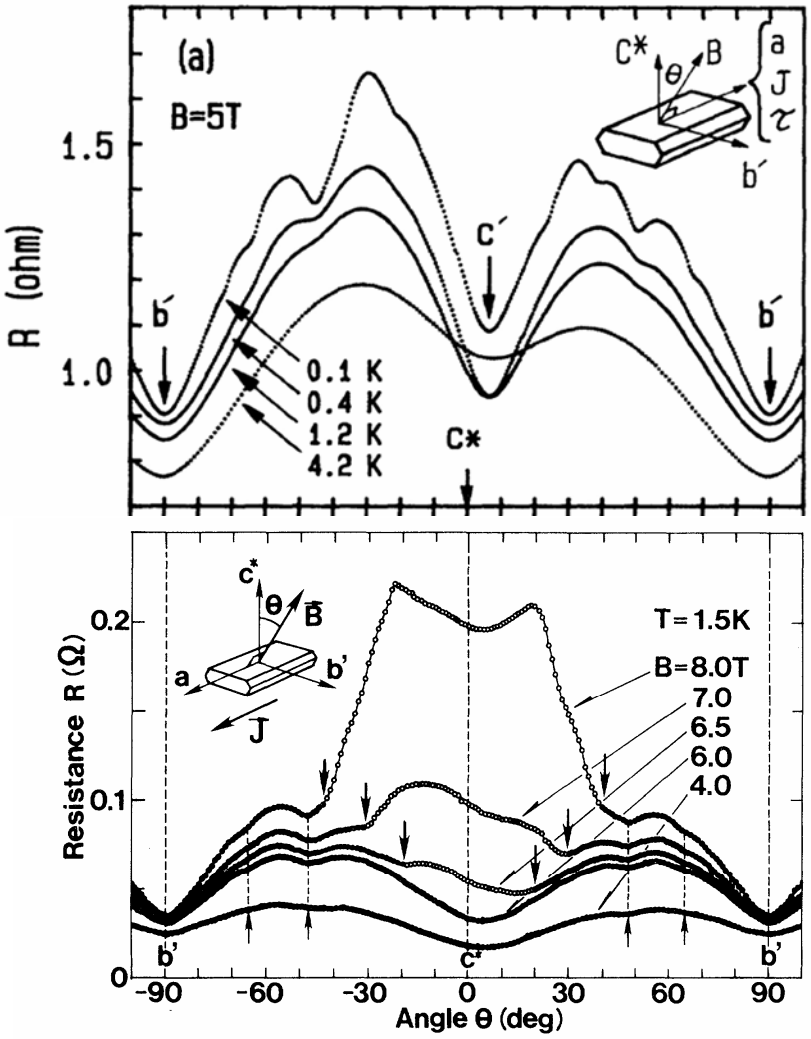

FIG. 2.5 The first experimentally observed Lebed magic angle (LMA) effect in $(TMTSF)_2ClO_4$ (a) from Naughton *et al.* [2.14] and (b) from Osada *et al.* [2.15].

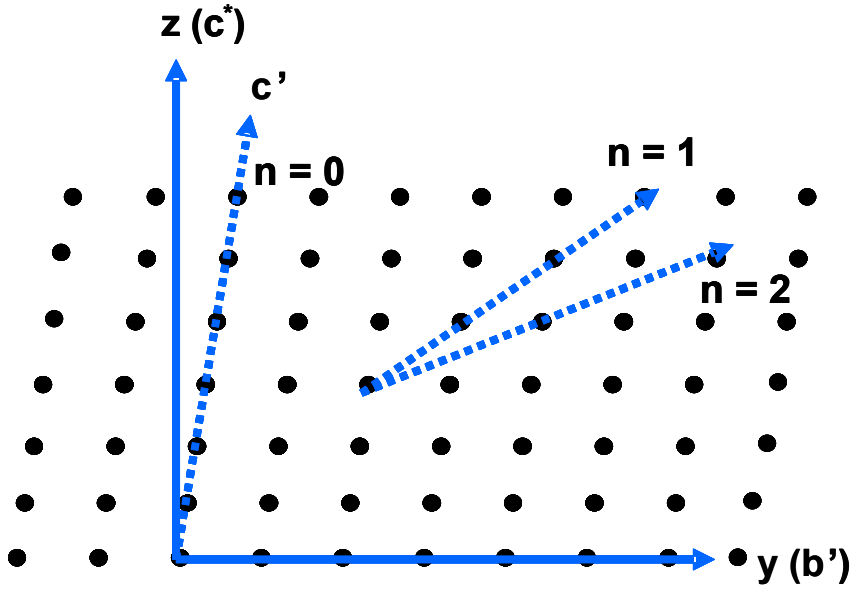

FIG. 2.6 Commensurate conditions are shown in real space. Resistance will have minima when the field is oriented along the real space lattice vector. The first minimum with $n = 0$ will occur ~ 6° $(TMTSF)_2ClO_4$ and ~ 8.5° for $(DMET)_2I_3$ away from the *z(c*)*-axis, the *c'*-direction.

2.3 Danner-Kang-Chaikin (DKC) Oscillations

The second AMRO effect on Q1D organic conductors was discovered by Danner, Kang and Chaikin in 1994, when the magnetic field is rotated in the *x*-*z* plane (rather than *y*-*z* plane), a series of peak structures in resistivity is observed for fields near *x*-axis. The positions of these structures were found to be independent of the magnetic field strength as shown in **Fig. 2.7**. These oscillations in magnetoresistance have been interpreted in terms of the semiclassical orbital averaging of the *z*-axis electron velocity given by $v_z = 2ct_c\sin(k_z c)$. For field along the *x*-axis, there is no Lorentz force from the velocity along x-axis and the velocities are only finite away from the extrema of the FS and the largest v_y is found along the lines at $k_y = \pm \pi/2b$. There are orbits traversing up and down k_z at, or near, these lines as shown by the dotted lines in **Fig. 2.8**. There are some close orbits,

but these do not go from inside to outside of a closed FS and therefore, do not contribute to the oscillations (*i.e.* they are not extremal orbits). The open orbits which traverse the FS in the *z* direction tend to average v_z to zero, hence, contributing to a nonsaturating magnetoresistance.

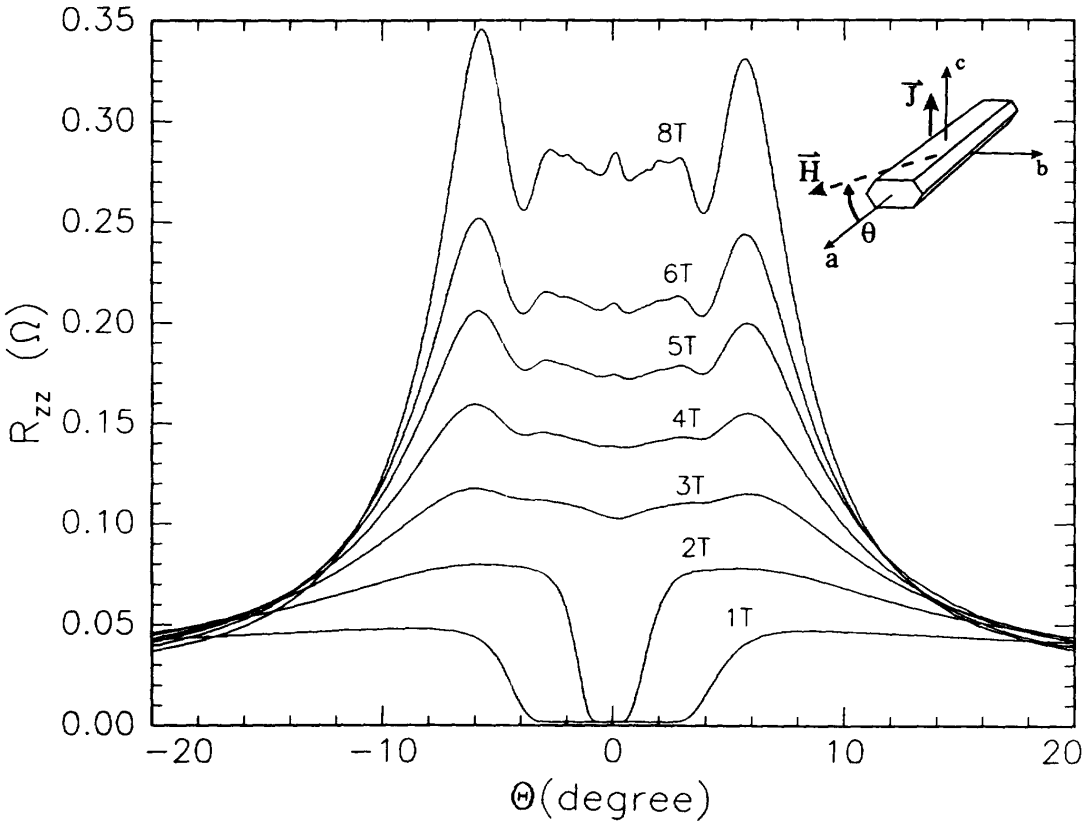

FIG 2.7 The angle dependence of interlayer resistance of $(TMTSF)_2ClO_4$ for magnetic field rotation in the *x-z* plane measured at *0.5K* At low fields (*1T* and *2T*) and small angle, the resistance goes to zero due to superconductivity [2.18].

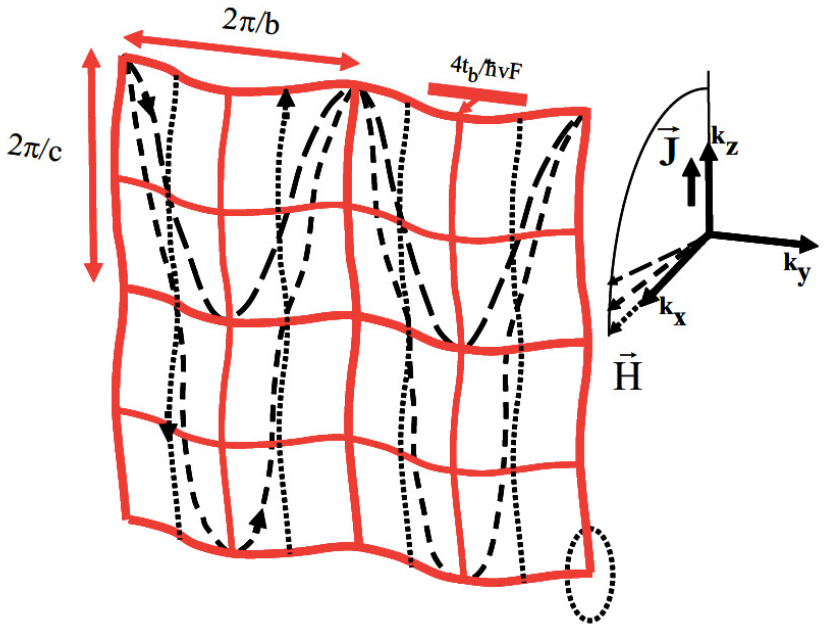

FIG 2.8 The Fermi surface for $(TMTSF)_2ClO_4$.Orbits (dotted) show the trajectory of electrons when the field is parallel to *x* for closed and open orbits. Here the angles for the peak resistance are directly related to the band parameters. The fastest averaging of $\langle v_z \rangle$ is when an orbit sweeps across the FS crossing an integral number of $2\pi/c$'s for each $2\pi/b$ [from Danner *et al.*, 2.18].

When the magnetic field is tilted, there becomes finite component along the *z*-axis, such that the orbit trajectories move along both *y* and *z* directions as shown in **Fig. 2.8**. There is averaging of v_z, particularly, if an orbit sweeps periodically over an integral number of reciprocal lattice along *c*, then $\langle v_z \rangle = 0$ for all orbits. This condition for maxima in magnetoresistance along *z,* corresponds to the tilt angle, which is proportional to t_b. Thus, measuring the field angle along the *c* direction allows for a determination of the warping of the FS. In the case of $(TMTSF)_2ClO_4$, the maxima in the magnetoresistance is found to be $\theta = \pm 6^o$, which corresponds to the $t_b = 0.012 \pm 0.001$ *eV* in the anion ordered state of ClO_4 [2.18].

2.4 Yoshino Third Angular Effects (YAE)

When the magnetic field is rotated in the most conducting *x-y* plane of Q1D systems, the magnetoresistance was found to exhibit a pair of minima centered at the angle $\phi = \pm 15^{o}$. This phenomenon was called the "third angular effect", with the LMA and DKC oscillations being the first two effects. The first TAE was initially observed in $(DMET)_2I_3$ by Yoshino *et. al*, [2.19] as shown in **Fig. 2.9.** Here, we call this third angular effect as "Yoshino third angular effect" (YAE) after it was discovered. It has been observed in many Q1D conductors, such as $(TMTSF)_2ClO_4$ [2.21, 2.22, 2.23], $(TMTSF)_2PF_6$ (0.85 GPa) [2.38], $(DMET)_2AuBr_2$ [2.38], $(DMET)_2AuCl_2$ [2.39] and $(DMET)_2CuCl_2$ [2.40].

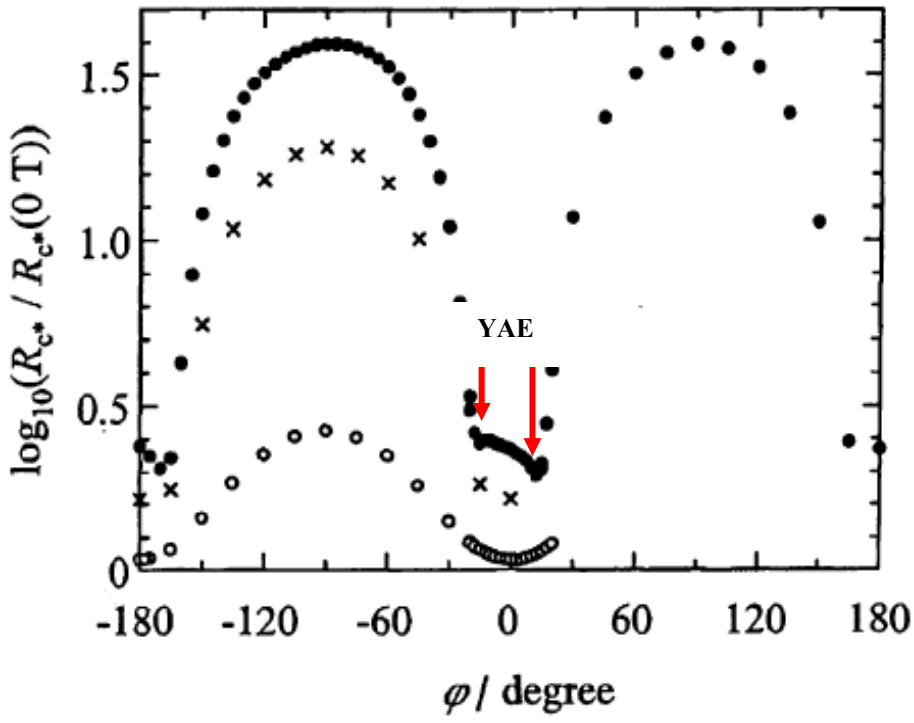

FIG. 2.9 Angle dependence of magnetoresistance of $(DMET)_2I_3$ for the current along the *(c*)* z-axis . For the value of higher magnetic field, a pair of minima are observed at an angle ~ ± 15° [2.19].

In a semiclassical framework, Osada *et al.* has proposed an explanation of the YAE based on small closed electronic orbits becoming open orbits as the field is rotated away from the *x*-axis, where the motion of the carriers on the FS is affected by the Lorentz force [2.41]. They claimed that the carriers drawing the close orbits then have no contribution to the conductivity along the *z*-axis (that being measured), such that the electrical resistivity shows a slight increase in the angle region where the closed orbital motion exists. While rotating the magnetic field in *x*-*y* plane, the closed orbits were claimed to disappear at an angle where magnetoresistance shows a minimum. However, Lebed and Bagmet [2.42] proposed that the YAE can be explained without the closed orbits. In their interpretation, the YAE is ascribed to the velocity-preserving nature of "effective" electrons, via their proximity to geometrical inflection points on the Fermi surface. These electrons are free from the Lorentz force because their carrier velocity is parallel to the magnetic field. The Lorentz force, acting on such electrons, is therefore vanishingly small, such that their momentum is conserved and the interlayer velocity does not oscillate. As a result, these electrons (*i.e.* electrons near particular sections of the Fermi surface) are the most "effective" in interlayer charge transport, which gives large contributions to the conductivity. At an inflection point of the Q1D Fermi surface, the number of carriers which are so effective is maximum. Since the density of the effective carriers diverges at the angle where the velocity is normal to the Fermi surface, when the inflection point matches with the magnetic field direction, there is a significant magnetoresistance drop. In other words, as shown by Lebed and Bagmet, when the direction of the magnetic field approaches an inflection point, more and more electrons

become effective, leading to a localized angular region of enhanced conductivity, and thus a local minima in the resistivity.

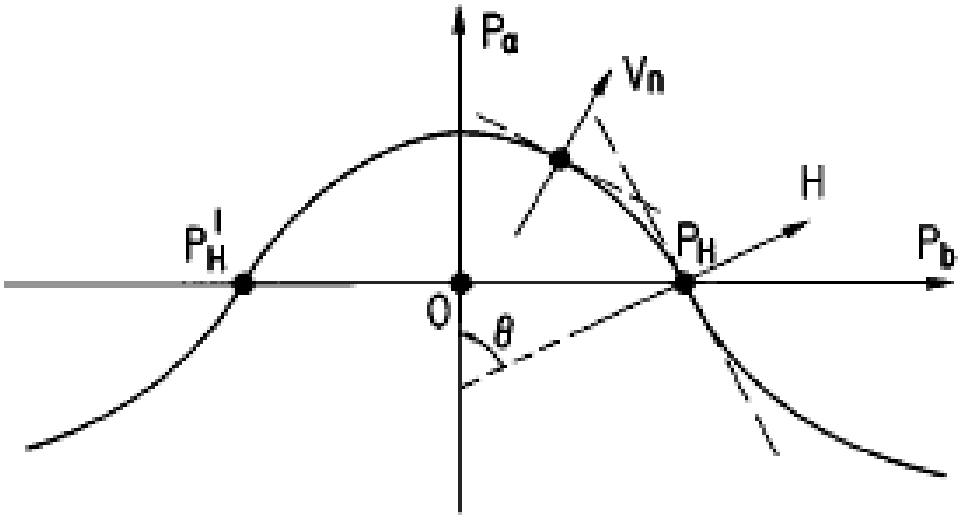

FIG. 2.10 The in-plane magnetic field is normal to the cross-section $p_a - p_f = 2tbcos(p_b b^*)/v_F$ [2.47].

Figure 2.10 show the side of the typical Q1D Fermi surface, with the magnetic field H oriented along θ as shown. At the geometrical inflection point P_H, the largest number of electrons becomes effective, giving rise to the resistance minimum. Lee and Naughton directly calculated the angle at which the previously mentioned open-closed event occurs, and showed it to be distinct from the angle at which the YAE is both characterized via the "*effective electron*" model and observed in $(TMTSF)_2PF_6$ [2.23].

Nevertheless, the origin of the YAE is closely related to the corrugation of the Q1D FS within the *x-y* plane and the critical angle ϕ_c (where the minima in magnetoresistance are observed). The in-plane anisotropy ξ can be defined as the ratio of t_y to t_x, and can be measured using the TYAE. Yoshino *et. al.,* [2.38, 2.39] numerically

calculated ξ dependence of $\Delta\phi$ (angular width of the two minima in magnetoresistance in either side of the *x*-axis) and compared it to the estimated values of ξ from experiment for several Q1D conductors. The dimensionality for $(DMET)_2I_3$ at ambient pressure was estimated to be 1/9.7, for $(TMTSF)_2PF_6$ under pressure to be 1/8.6, for $(DMET)_2AuBr_2$ to be 1/10, for $(DMET)_2AuCl_2$ is 1/9.8 and 1/10 for $(DMET)_2CuCl_2$. Furthermore, Yoshino *et al.,* measured the pressure dependence of $\Delta\phi$ from YAE data on $(TMTSF)_2PF_6$ [2.43], $(DMET)_2I_3$ [2.43] and $(TMTSF)_2ClO_4$ [2.44]. It was found that $\Delta\phi$ increases with pressure, corresponding to an increase in ξ. Thus, the YAE gives direct experimental evidence of the dimensionality enhancement in Q1D conductors by pressure.

2.5 Lee-Naughton (LN) Oscillations

Finally, when a Q1D crystal is rotated along an arbitrary magnetic field plane, in particular nearly about the *z*-axis and close to the *x*-*y* plane, far more complex magnetoresistance oscillations are observed. These were first observed in $(TMTSF)_2PF_6$ [2.23] by Lee and Naughton, and therefore came to be known as Lee-Naughton or LN Oscillations. The original LN data for (TMTSF)2PF6 is shown in **Fig. 2.11.** Similar LN oscillations were later observed in $(TMTSF)_2ClO_4$, [2.45] by Ha and Naughton and in $(DMET)_2I_3$ by Yoshino *et al.* [2.20].

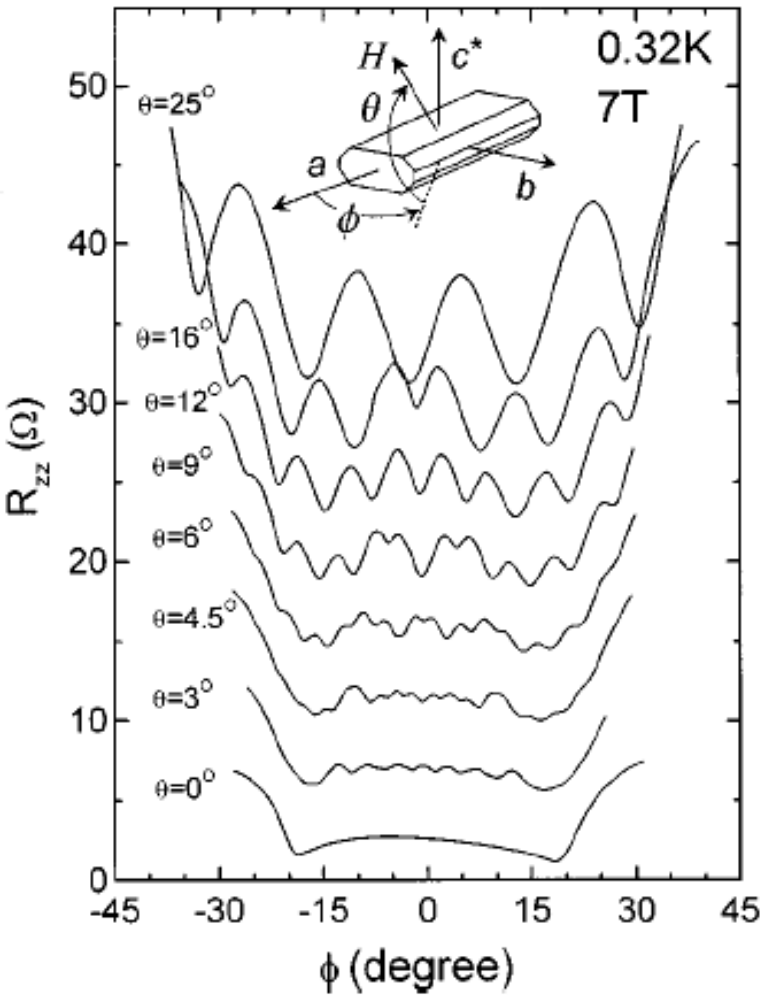

FIG. 2.11

Angle dependence of transverse resistance, R_{zz}, in $(TMTSF)_2PF_6$ with y-axis offset for various tilt angles θ. At θ=0°, the TAE is observed, while the extra oscillations associated with the LN-effect occur for finite angles θ. The inset shows the sample orientation in magnetic field [2.23].

As discussed earlier, for the field rotated in the x-y plane, the YAE is observed. In case of $(TMTSF)_2PF_6$, additional small oscillations appear for the field rotation in a plane slightly off the x-y plane (~ 3°), second curve from the bottom in **Fig. 2.11**. At higher tilt angles, more pronounced oscillations are observed. Initially, these oscillations were conjectured to be projections of the LMA in to the rotation plane employed.

However, more oscillations are observed in off-angle rotations than in a pure Lebed (*y-z* plane) rotation of the magnetic field. Lebed and Naughton [2.46] provided an alternate explanation, known as the "interference commensurate effect" (IC) , which refers to the interference between electron waves from adjacent Brillouin zones at particular field orientations, give either local maxima or local minima in resistivity, depending on the orientation of the magnetic field.

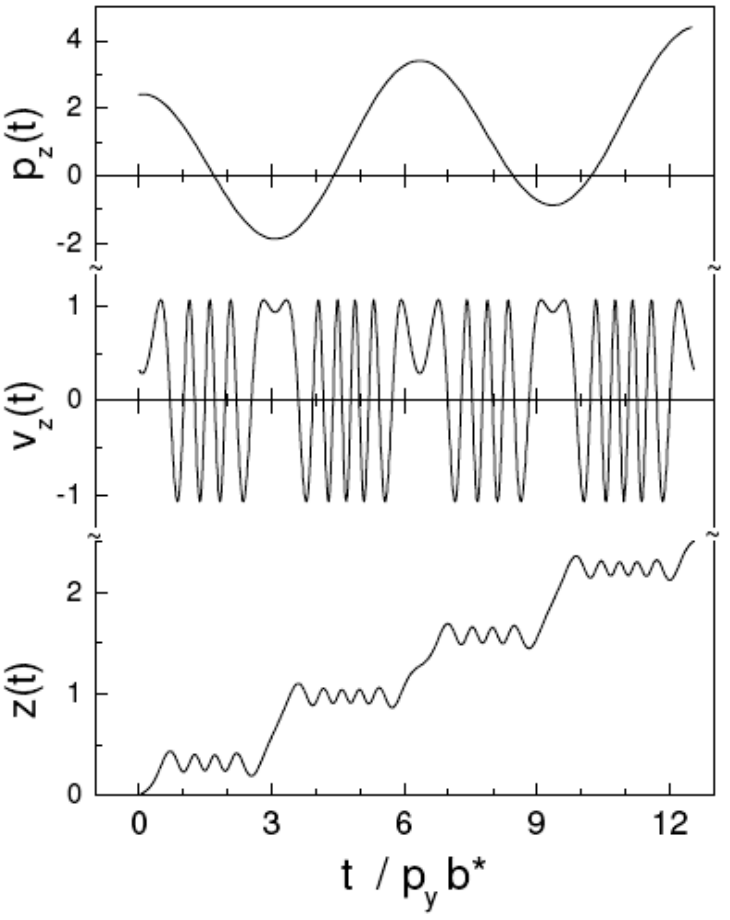

FIG. 2.12 Electron trajectory, interlayer velocity $v_z(t)$ and coordinate $z(t)$ under a magnetic field [2.47].

This IC effect can be elaborated as follows. As shown in the upper curve in **Fig. 2.12**,momentum-space electron trajectories in the $p_y p_z$-plane are no longer straight lines, but oscillate with an amplitude $\Delta p_z = 4t_y \tan\theta \cos\phi / v_F$, where v_F is the Fermi velocity. At an LMA field direction, an electron, following the trajectory is displaced along p_z by an integer number of unit cell, $N(2\pi\hbar/c)$, during one oscillation period $T_y = 2\pi/\omega_y$. The interlayer velocity is then a periodic function of time; its average, contributed mainly by the trajectory parts near extremal values of $p_z(t)$, is generally nonzero. Thus, the electron acquires a finite shift along the z-axis, as shown in lower curve in **Fig. 2.12**. As a result, the resistivity ρ_{zz} exhibits local minima.

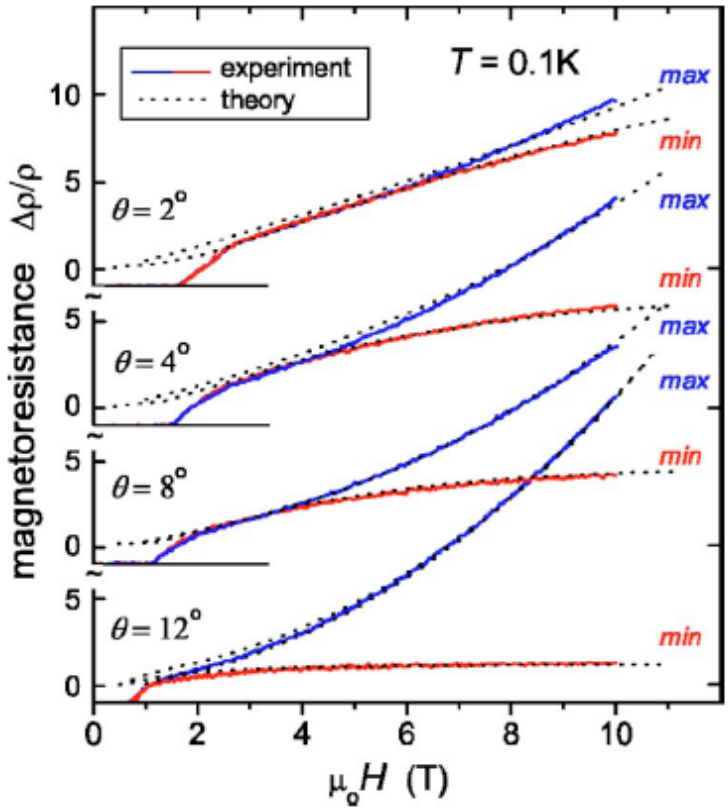

FIG. 2.13 1D⟶2D dimensional crossovers as revealed by $R_{zz}(B)$ at certain commensurate and non commensurate orientations. For each angle θ indicated, ϕ was adjusted to reach a resistance maximum or minimum [2.45].

A particular manifestation of the IC effect was found in fixed angle measurements, where the magnetoresistance displays qualitatively different behavior at field orientations when the resistance is at a local minimum versus a local maximum. As discussed by Ha, Lebed and Naughton [2.45], these behavior are associated with 1D and 2D transport. A key point is that the LN magnetoresistance oscillations can be then interpreted in terms of these 1D to 2D crossovers. In the absence of close orbits for Q1D Fermi surfaces, in stead of Landau quantization, the quantum effect in a magnetic field is that of Bragg reflections which the authors of Ref. 2.45 suggest, resulting in a series of 1D to 2D crossovers at the minima of the LN oscillations. In other words, electron wave functions, localized on the 1D chain at arbitrary field directions, become delocalized on 2D planes at the commensurate directions. This dimensional crossover notion was used to investigate electron motion in the Q1D metal $(TMTSF)_2ClO_4$ in a strong magnetic field [2.45]. In this model $\rho_{zz}(B,\theta,\varphi)$ is expected saturate at high field for commensurate orientations. However, away from these special directions, it should follow B^2 dependence as shown in **Fig. 2.12**. ρ_{zz} indeed saturates at commensurate directions (minima), while at non-commensurate directions (maxima) it exhibits a non-saturating behavior. Thus, the prediction of saturating magnetoresistance at commensurate angles (minima in angle sweeps) and non-trivial, non-saturation otherwise, seems to be borne out in the experiments.

Lee and Naughton defined the position of minima observed in terms of the angle α in terms of θ and ϕ by the relation

$$\tan\alpha = \sin\phi / \tan\theta \qquad (2.5)$$

where $\tan\theta$ is given by Eq. (2.4). It is found that the numbers of minima in oscillations in LN-orientations are higher than the pure Lebed orientations [2.23].

In next section, we will discuss some available theoretical models to explain these experimentally observed AMROs.

2.6 Some Theoretical Models on AMRO

When a magnetic field is applied to a conducting material, Lorentz force isexperienced by an electron, given by

$$F_L = \frac{d\vec{p}}{dt} = e\vec{v} \times \vec{B} \tag{2.6}$$

where *p*, *v*, and *e* are the electron's momentum, velocity, and charge, respectively. In Q1D systems, the FS consists of the sheets extended perpendicular to the *x*-axis and wrapped along the *y*-axis [Fig. 1.3 (e)]. For such a system, the electron dispersion relation in the lowest order tight-binding approximation was provided in Eq. (1.1).

When a strong magnetic field $\vec{B} = (0, B\sin\theta, B\cos\theta)$ is applied in a plane perpendicular to the chains in such systems, the Lorentz force makes electrons move along the Fermi sheets, crossing many Brillouin zones. One can define a frequency with which an electron crosses a given Brillouin zone in the k_y and k_z directions is, respectively, as

$$\omega_y = b\left|\frac{dk_y}{dt}\right| = \frac{ev_F b}{\hbar} B\cos\theta \tag{2.7}$$

and $$\omega_z = c\left|\frac{dk_z}{dt}\right| = \frac{ev_F c}{\hbar} B\sin\theta \tag{2.8}.$$

For the field along the direction given by

$$\tan\theta = \frac{p}{q}\frac{b}{c} \tag{2.9}$$

where p and q are integers, these frequencies are commensurate and the motion in momentum space becomes periodic. In other words, orientations given by Eq. (2.9) yield commensurability resonances. This results in the oscillations of the magnetoresistance with the sharp minima observed at the angle given by Eq. (2.9). As discussed in Section 2.2, this was first suggested Lebed [2.12], and is the Lebed magic angle (LMA) effect and was experimentally reported by Naughton *et al.* [2.13, 2.14] and Osada *et al.* [2.15] in the metallic state of $(TMTSF)_2ClO_4$. For a triclinic crystal structure, the Eq. (2.9) is modified to the Eq. (2.4).

There exist several theoretical models to explain this LMA effects in Q1D conductors in terms of the field-induced density-wave instability [2.12, 2.48, 2.49], electron-electron interactions [2.50, 2.51,2.52] and non Fermi liquid behavior [2.53, 2.54]. In one of the model, Osada *et al.,* [2.55] proposed a dispersion relation with higher order interchain transfer integrals, as

$$\mathrm{E}(\vec{p}) = -2t_x\cos(p_x a/\hbar) - \mathrm{E}_F - 2(\sum_{m,n} t_m\cos(mp_y b/\hbar) + t_n\cos(np_z c/\hbar)) \tag{2.10}$$

where m and n are integers. The conductivity calculated using this dispersion relation gives the correct condition for the observed magnetoresistance minima; however, an explanation for the physical significance of this extra mixed m-n term added to the dispersion relation has yet to be preferred.. Furthermore, in the case of $(TMTSF)_2X$ (X = ClO_4 and PF_6), the experimentally observed minima in magnetoresistance are observed for q = 1, meaning p/q takes only integer values n. It is suspected, however that the

LMA oscillations observed in $(TMTSF)_2ReO_4$ [2.56] may be attributed to the existence of such high-order interchain transfer terms [2.57].

When the magnetic field is applied in the direction defined by $\vec{B} = (B\sin\theta,\ 0,\ B\cos\theta)$, the trajectories of electrons are extended along the k_y-axis and the interlayer momentum k_z oscillates as

$$k_z(t) = k_z(0) + \frac{2t_y}{\hbar v_F}\tan\theta\sin(\omega_y t) \tag{2.11}$$

where ω_y is given by Eq. (2.5). The amplitude of this oscillation is given by $4t_y\tan\theta/\upsilon_F$. When θ is close to zero, the amplitude of this oscillation is smaller than the size of the Brillouin zone in the k_z-direction, and $\langle v_z \rangle$ has a non-zero value. When θ increases, the amplitude is equal to the $2\pi\hbar/c$ and $\langle v_z \rangle$ vanishes, giving rise to the maxima in resistivity. The series of magnetoresistance peaks (DKC oscillations) thus occur every time the electron orbit crosses the Brillouin zone. The period of the DKC oscillations in magnetoresistance can be expressed as

$$\Delta(\tan\theta) = \frac{\pi\hbar v_F}{2t_y c}, \text{ and} \tag{2.12}$$

the condition for the $\langle v_z \rangle = 0$ is determined by the zeros of the Bessel function $J_0[2t_y c\tan\theta/\hbar v_F]$. McKenzie and Moses [2.58] calculated the interlayer conductivity for coherent and incoherent transport for a tilted magnetic field for such a system and their results are similar to the experimentally observed DKC oscillations.

A general quantum picture for magnetoresistance angular effects in Q1D conductors was given by Osada and coworkers [2.59, 2.60]. They considered the incoherent limit where in-plane scattering happens more often than interlayer tunneling,

such that the tunneling between adjacent layers leads to all the angular effects, except the a "peak effect" caused by closed orbits. The LMA is described as resulting from resonant magnetotunneling between adjacent layers, and the DKC oscillations and YAE are just modulations of this tunneling amplitude. In this model, the expression for the DC conductivity using the Kubo formula with the lowest order contribution for t_c is written as

$$\sigma_{zz} = \frac{4}{2\pi bc\hbar v_F}\left(\frac{et_z c}{\hbar}\right)^2 \sum_{\pm,n} J_n\left(\frac{4t_y}{v_F beB_z}\sin\left(\frac{ebcB_x}{2\hbar}\right)\right)^2 \times \frac{\tau}{1+v_F^2\left(n\frac{beB_z}{\hbar} \pm \frac{ceB_y}{\hbar}\right)^2\tau^2} \tag{2.13}$$

When the field is rotated in the *y*-*z* plane, the denominator of last term gives in Eq. 2.13, $\frac{B_y}{B_z} = \pm n\frac{b}{c}$, which is the same as Eq. [2.7], with *n* being an integer. However, when the field is rotated in the *y*-*z* plane, higher order Bessel functions vanish, with only $J_0(0) = 1$ remaining giving rise to a smooth variation in resistivity with no oscillations. This expression for the conductivity, qualitatively explains the experimentally observed AMRO in Q1D systems as shown in **Fig. 2.13, 2.14 and 2.15**. **Figure 2.13** is the three dimensional plot of the calculated magnetoconductivity using eq. (2.13) for the Q1D conductor $(TMTSF)_2PF_6$ with anisotropy t_x:t_y:y_z = 300:30:1 at magnetic field strength of 9T. The spikes like structures developed towards the center of the plot, are called LN–oscillations. **Figure 2.14** shows the density plot of the interlayer magnetoconductivity calculated using the same Eq. (2.13). It is seen that the features in plot developed with the increase in the magnetic field strengths and becomes sharper at higher magnetic field. The horizontal line for B_x/B_z = 0 represents the Lebed plane of field rotation, having the

single peak structure at the center. The features developed along the diagonal lines in **Fig. 2.15** are LN–oscillations.

A similar expression was derived by Lebed and Naughton [4.47], assuming that the origin of the oscillations observed for the field rotating along an arbitrary direction is related to interference effects resulting from Bragg reflections, which occur as electrons move along quasi-periodic and periodic ("commensurate") electron trajectories in the extended Brillouin zone. This expression qualitatively explains the YAE and LN oscillations, but fails to reproduce the LMA. Alternately, Lebed *et al.* [2.61] proposed that an interference effect between the velocity of electrons and the density of states, gives rise to 1D and 2D crossover, which appear to result in peaks of the interlayer conductivity at magic angles.

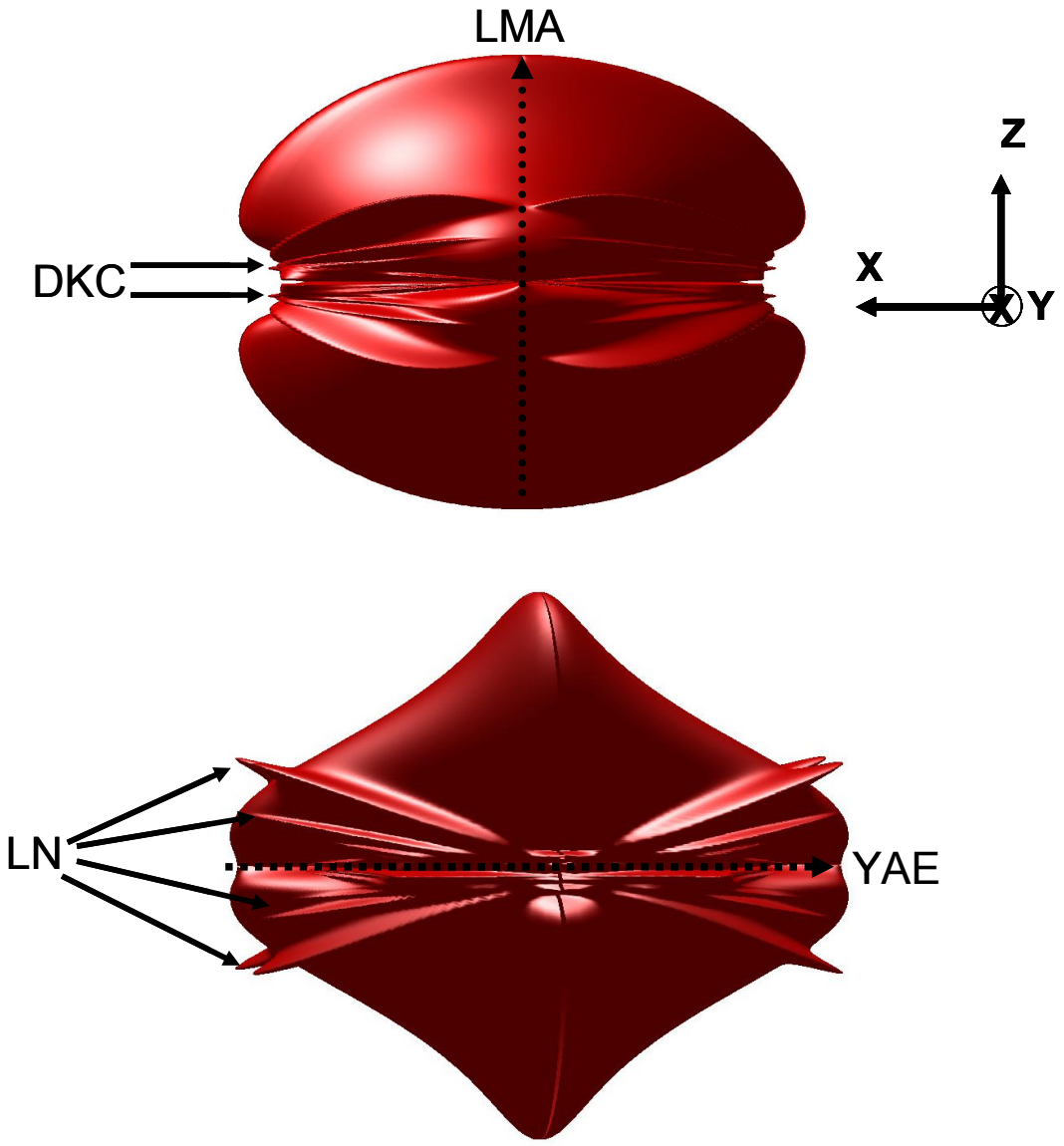

FIG. 2.14 Three-dimensional (3D) plot of the calculated magnetoresistance using Eq. (2.13) for Q1D conductors with $t_x:t_y:t_z = 300:30:1$ at magnetic field $9T$. The upper figure is viewed along the y-axis. The left and right structures are the DKC oscillations, which are observed for the field rotated in the x-z plane. The spike-like structures developed towards the center which is the LN oscillations. The lower figure is viewed along the x-axis. Again the spike-like features developed while going away from the center (LN oscillations). These spike features are discontinuous at the y-z plane shown by vertical dotted line. Also, the horizontal dotted line represents the YAE.

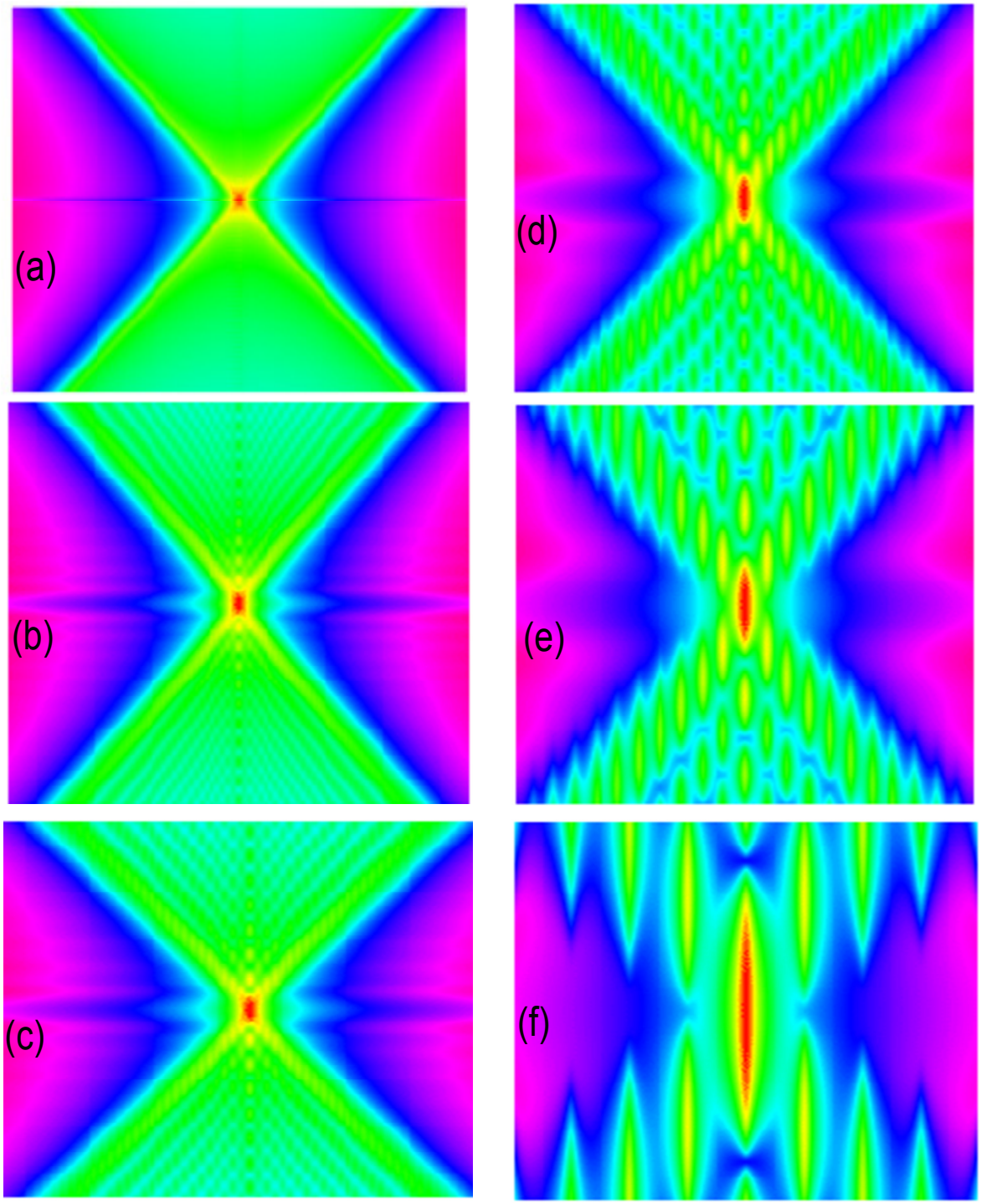

FIG. 2.15 The density plot of the interlayer conductivity calculated using Eq. (2.13) for Q1D (parameter used in calculation are for $(TMTSF)_2PF_6$). The plots (a)-(f) are for different magnetic field 0.1, 2, 5, 10, 15, and 20T. The AMRO becomes sharper and broader while increasing magnetic field.

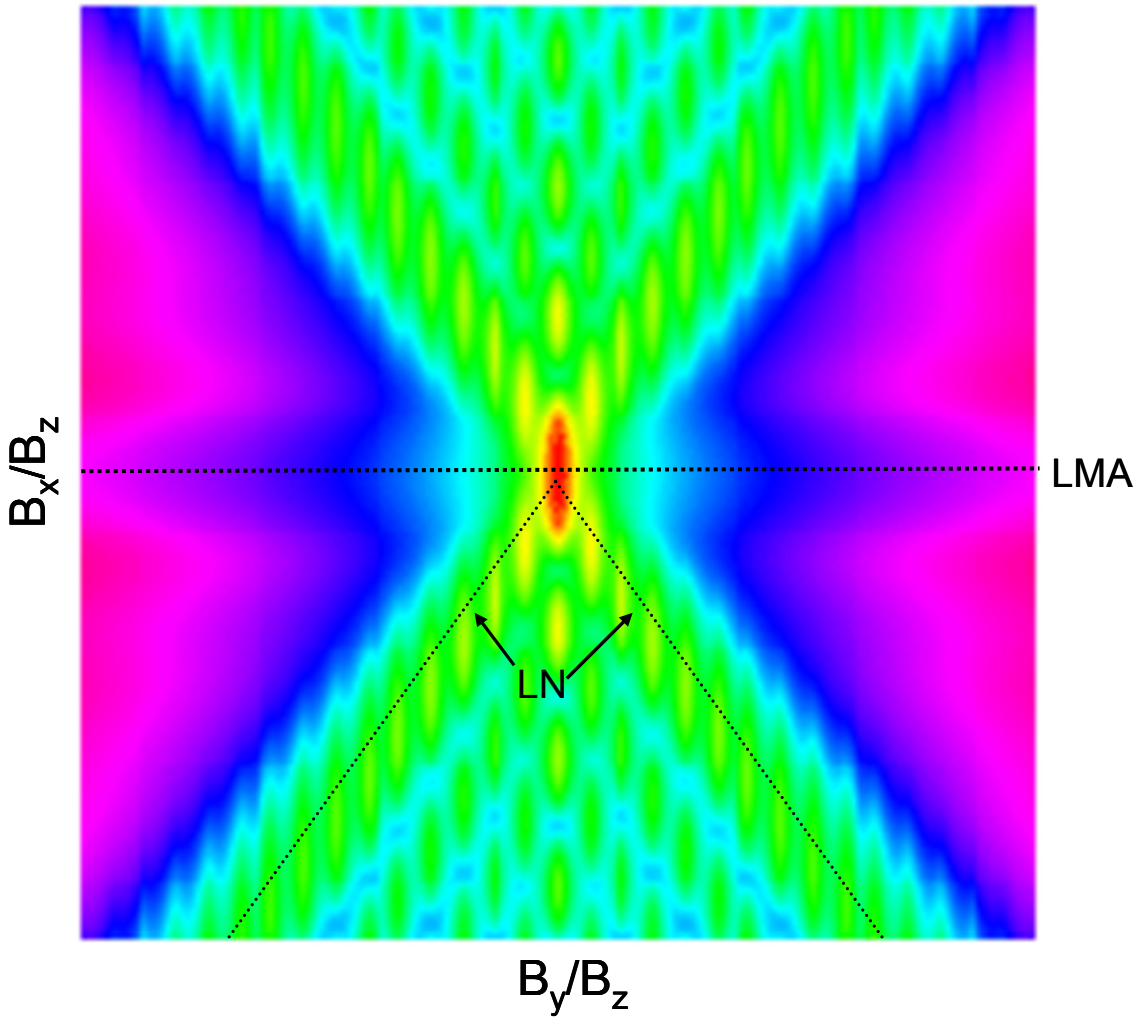

FIG. 2.15 The density plot of the interlayer conductivity calculated using Eq. (2.13) for Q1D (parameter used in calculation are for $(TMTSF)_2PF_6$). The black horizontal dotted line represents the LMA, where as the diagonal dotted represents the LN oscillations.

In a very intriguing interpretation of AMRO in Q1D, Cooper and Yakovenko [2.62] derived an expression which is also similar to the Kubo-based expression of **Eq. 2.11** by considering Aharonov-Bohm interference in interlayer electron tunneling. This interpretation also qualitatively explains the experimentally-observed effects but again fails to reproduce the *yz*- plane Lebed effect.

All theoretical models explained above are based on an orthorhombic approximation to the actual triclinic crystal structure of the materials, in which the AMRO effects have been seen. Osada *et al.* [2.21], calculated the interlayer magnetoresistance using Boltzmann transport equation with constant relaxation time and found the oscillations in magnetoresistance for the field rotation in *x*-*y*, *y*-*z* and *z*-*x* planes for cubic Q1D system.

In summation, each of models qualitatively explains some of the experimentally-observed angular magnetoresistance oscillations in Q1D systems, but not all. However, the question is still debatable, whether these angular effects are independent or these are the modulation of one effect. Kang *et al.,* [2.63] measured the magnetoresistance of $(TMTSF)_2PF_6$ for all possible angular orientations of magnetic field of 8T at 1.5K under pressure 8.4 kbar. They have presented their data in a 3D plot and compared the data with the similar plot obtained using **Eq. 2.11**. The experimental data and calculated magnetoconductivity for $(TMTSF)_2PF_6$ has similar 3D structures, however, the calculated data has no oscillating features for the field rotated in the *yz*-plane. Based on the experimental results and calculated data, the authors of Ref. 2.63 concluded that the LMA is the only "fundamental effects," where as all remaining effects are the modulations of LMA. This contention is arguable, since, experimentally, the oscillation amplitudes

decrease as the field direction approaches the *y-z* plane, where the Lebed effect is expected to be strongest. Furthermore, higher order oscillations vanish when the field direction approaches the *y-z* plane. This led us in the direction to search the origin of these magnetoresistance oscillations and their relationships (if any) to other Q1D system $(DMET)_2I_3$ which has similar crystals structure as $(TMTSF)_2X$ and crystal anisotropy. Are all four (LMA, DKC, YAE and LN) independent phenomenon observed in Q1D systems? Are they related to each other? Is one of the effect fundamental and all others are the modulations of one effect?

In the present work, we have measured the magnetoresistance of the different kind of Q1D conductor, namely $(DMET)_2I_3$, for all possible angular orientation of magnetic field with higher magnetic field and very low temperature (100mK). This allows us to achieve B/T = 90 T/K, and explore the magnetoresistance oscillations more accurately, whether or not these oscillations have field and temperature dependence. Furthermore, the material $(DMET)_2I_3$ itself appears to be a suitable candidate to explore AMRO, because of the absence of any phase transitions at low temperature. Also, we have simulated the magnetoresistance of $(DMET)_2I_3$ using true triclinic crystals structures where all previously discussed models were approximated to orthorhombic crystal structures.

References

[2.1] W. Thompson, Math. And Phys. Papers, **2**, 267 (1856).

[2.2] A. B. Pippard, *Magnetoresistance in Metals*, Cambridge University Press, Cambridge, (1989).

[2.3] W. Shubnikov and W. J. de Haas. Proc. Neth. Roy. Acad. Sci. **33,** 130 (1930) .

[2.4] W. J. de Haas and P. M. van Alphen. Proc. Neth. Roy. Acad. Sci. **33,** 1106(1930).

[2.5] K.V. Klitzing, G. Dorda, and M. Pepper, Phys. Rev. Lett. **45**, 6, 494 (1980).

[2.6] D. Tsui, H. Stromer and A. Gossard, Phys. Rev. Lett., **48**, 1599 (1982).

[2.7] K. Oshima,T. Mori, H. Inokuchi, H. Urayama, H. Yamochi, and G. Saito, Phys. Rev. B **38**, 938 (1988).

[2.8] D. Schweitzer, E. Balthes, S. Kahlich, I. Heinen, H. J. Keller, W. Strunz, W. Biberacher, A. G. M. Jansen, and E. Steep, Synth. Met. **70**, 857 (1995).

[2.9] M. V. Kastronovik, P. A. Kononovich, V. N. Laukhin, and I. F. Shchegolev, JETP Lett. **48**, 541 (1988).

[2.10] K. Yamaji, J. Phys. Soc. Jpn. **58**, 1520 (1989).

[2.11] T. Ishiguro, K. Yamaji, and G. Saito, *Organic Superconductors*, Second Edition Springer Verlag, (1998).

[2.12] A.G. Lebed, JETP Lett. **43**, 174 (1986).

[2.13] M.J. Naughton, O. H. Chung, L. Y. Chiang, and J. S. Brooks, Mater. Res. Soc. Symp. Proc. **173**, 257 (1990).

[2.14] M. J. Naughton, O. H. Chung, M. Chaparala, X. Bu, and P. Coppens, Phys. Rev. Lett. **67**, 3712 (1991).

[2.15] T. Osada, A. Kawasumi, S. Kagoshima, N. Miura, and G. Saito, Phys. Rev. Lett. **66**, 1525 (1991).

[2.16] W. Kang, S.T. Hannahs, and P.M. Chaikin, Phys. Rev. Lett. **69**, 2827 (1992).

[2.17] S. Uji, C. Terakura, T. Terashima, H. Aoki, H. Nishikawa, I. Ikemoto, and K. Kikuchi,, *Proceeding of Physical Phenomena at High Magnetic Fields III* (World Scientific, London, 1998), p 227.

[2.18] G. M. Danner, W. Kang, and P. M. Chaikin, Phys. Rev. Lett. **72**, 3714 (1994).

[2.19] H. Yoshino, K. Saito, K. Kikuchi, H. Nishikawa, K. Kobayashi, and I. Ikemoto, J. Phys. Soc. Jpn. **64**, 2307 (1995).

[2.20] H. Yoshino, K. Saito, H. Nishikawa, K. Kikuchi, K. Kobayashi, and I. Ikemoto, J. Phys. Rev. Soc. Jpn. **66**, 2248 (1997).

[2.21] T. Osada, S. Kagoshima, and N. Miura, Phys. Rev. Lett. 77, 5261 (1996).

[2.22] M. J. Naughton, I. J. Lee. P. M. Chaikin, and G. M. Danner, Synth. Met. **85**, 1481 (1997).

[2.23] I. J. Lee and M. J. Naughton, Phys. Rev. B 57, 7423 (1998).

[2.24] J. F. Kwak, J. E. Schirber, R. L. Greene, and E. M. Engler, Mol. Cryst. Liq. Cryst. **79**, 111 (1982).

[2.25] R. Vrusetti, K. Bechgaard, G. C. Lonzarich, and R. H. Friend, J. Phys, Colloq. **44**, C3-1055 (1983).

[2.26] K. Murata, H. Bando, K. Kajimura, T. Ishiguro, H. Anzai, S. Kagoshima, and G. Saito, Mol. Cryst. Liq. Cryst. **119**, 131 (1985).

[2.27] X. Yan, M. J. Naughton, O. S. Cheema, R. V. Chamberlin, S. Y. Hsu, L. Y. Chiang, and P. M. Chaikin Solid State Commun., **66**, 905 (1988).

[2.28] A. G. Lebed and P. Bak, Phys. Rev. Lett., **63**, 1315 (1989).

[2.29] G. S. Boebinger, G. S. Boebinger, G. Montambaux, M. L. Kaplan, R. C. Haddon, S. V. Chichester,and L. Y. Chiang, Phys. Rev. Lett., **64**, 591 (1990).

[2.30] W. Kang, S. T. Hannahs, P. M. Chaikin, Phys. Rev. Lett., **69**, 2827 (1992).

[2.31] E. I. Chashechkina and P. M. Chaikin, Phys. Rev. Lett., **80**, 2181 (1998).

[2.32] H. Kang, Y. J. Jo, S. Uji, W. Kang, Phys. Rev. B **68**, 132508 (2003).

[2.33] N. Biskup, J. S. Brooks, R. Kato, K. Oshima, Phys. Rev. B. **62**, 21 (2000).

[2.34] Y. Shimojo, M. A. Tanatar, T. Ishiguro, R. Kato, J. Phys. Soc. Jpn. **71**, 393 (2002).

[2.35] K. Oshima, T. Kambe, T. Sasaki, and R. Kato, Synth. Met. **154**, 259 (2005).

[2.36] H. Ito, Y. Yokochi, D. Suzuki, H. Tanaka, S. Kuroda, K. Enomoto, S. Uji, M. Umemiya, H. Miyasaka, K. I. Sugiura, M. Yamashita, Synth. Met. **156**, 162 (2005).

[2.37] S. Yasuzuka, C. Terakura, T. Yakabe, Y. Terai, H. M. Yamamoto, R. Kato, S. Uji, Synth. Met. **135-136**, 647 (2003).

[2.38] H. Yoshino, K. Saito, H. Nishikawa, K. Kikuchi, K. Kobayashi, and I. Ikemoto, J. Phys. Soc. Jpn, **66**, 2410 (1997).

[2.39] H. Yoshino, K. Murata, K. Saito, H. Nishikawa, K. Kikuchi, and I. Ikemoto, Phys. Rev. B **67**, 035111 (2003).

[2.40] H. Ito, D. Suzuki, Y. Yokochi, S. Kuroda, M. Umemiya, H. Miyasaka, K.I. Sugiura, M. Yamashita, and H. Tajima, Phys. Rev. B **71**, 212503 (2005).

[2.41] T. Osada, Synth. Met. **86**, 2143 (1997).

[2.42] A. G. Lebed and N. N. Bagmet, Phys. Rev. B **55**, R8654 (1997).

[2.43] H. Yoshino, A. Oda, K. Murata, H. Nishikawa, K. Kikuchi, and I. Ikemoto, Synth. Met. **120**, 885 (2001).

[2.44] H. Yoshino, S. Shodai, and K. Murata, Synth. Met. **133-134**, 55 (2003).

[2.45] H. I. Ha, A. G. Lebed, and M. J. Naughton, Phys. Rev. B **73**, 033107 (2006).

[2.46] A. G. Lebed and M. J. Naughton, Phys. Rev. Lett. **91,** 187003 (2003).

[2.47] A. G. Lebed and M. J. Naughton, cond-mat/0304591 (unpublished).

[2.48] G. Montambaux and P. B. Littlewood, Phys. Rev. Lett. **62**, 953 (1989).

[2.49] L. Chen and K. Maki, Synth. Met. **29**, F493 (1989).

[2.50] A. G. Lebed and P. Bak, Phys. Rev. Lett. **63**, 1315 (1989).

[2.51] V. M. Yakovenko, Phys. Rev. Lett. **68**, 3607 (1992).

[2.52] P. M. Chaikin, Phys. Rev. Lett. **69**, 2831 (1992).

[2.53] S. P. Strong, S. P. Strong, and P. W. Anderson, Phys. Rev. Lett. **73**, 1007 (1994).

[2.54] G. M. Danner and P. M. Chaikin, Phys. Rev. Lett. **75**, 4690 (1995).

[2.55] T. Osada, S. Kagoshima and N. Miura, Phys. Rev. **B 46**, 1812 (1992).

[2.56] H. Kang, Y. J. Jo, S. Uji, and W. Kang, Phys. Rev. **B 68**, 132508 (2003).

[2.57] M. V. Kartsovnik, Chen. Rev. **104**, 5737 (2004).

[2.58] R. H. Mckenzie and P. Moses, Phys. Rev. Lett. **81**, 4492 (1998).

[2.59] T. Osada, Physica E , ***12***, 272 (2002).

[2.60] T. Osada, M. Kuraguchi, Synth. Met., **133-134**, 75 (2003).

[2.61] A.G. Lebed, N.N. Bagmet, and M.J. Naughton, Phys. Rev. Lett. **93**,157006 (2004).

[2.62] B. K. Cooper and V. Yakovenko, Phys. Rev. Lett. **96**, 037001 (2006).

[2.63] K. Wang, T. Osada, Y. J. Jo, and H. Kang, Phys. Rev. Letts. **99**, 017002 (2007).

Chapter 3

Experimental Setup

3.1 Introduction

All experimental work was carried out in a dilution refrigerator with horizontal magnetic field. The four-terminal resistance measurement technique was employed to measure magnetoresistance of the $(DMET)_2I_3$ samples. In this Chapter, we discuss a brief-working principle of the dilution refrigerator, the measurement technique, and the two rotators used for sample alignment.

3.2 Dilution Refrigerator

H. London in 1951 proposed the principle of operation of the dilution refrigerator based on the phase diagram of ^{3}He-^{4}He mixture. The phase diagram of ^{3}He-^{4}He mixture is shown in [**Fig. 3.1**]. There exists the tricritical point, below which the mixture will separate into two liquid phases divided by a phase boundary. One phase is ^{3}He rich phase and mostly contains ^{3}He, whereas the other is ^{4}He phase (the "dilute" phase). The two phases are maintained in liquid-vapor form. Since there is a boundary between them, extra energy is required for particles to go from one phase to the other. When the mixture is pumped, most of the ^{3}He will be removed, upsetting the equilibrium. To restore equilibrium, ^{3}He must cross the phase boundary from the rich side to the dilute side at the expense of energy. This energy is in the form of heat, which is taken off through the walls of the mixing chamber that is thermally in contact to the sample space. With this,

the continuous circulation of the ^{3}He (*i. e.*, evaporation of ^{3}He carries heat) removes heat from the sample space and cools it down.

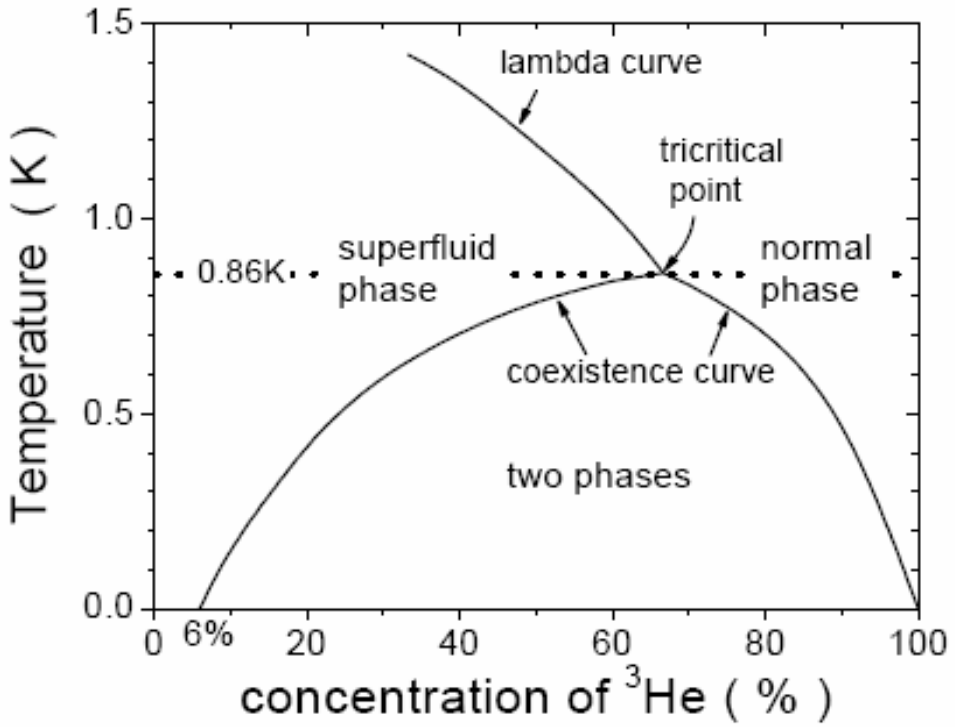

FIG 3.1 Phase diagram of ^{3}He-^{4}He mixture.

The dilution refrigerator employed for the present work is the Oxford Instruments Kelvinox system, including HE-100 insert and IGH intelligent gas handling system. The system can reach a base temperature of ~10 mK without any load. **Fig. 3.2** shows the schematic diagram of the dilution refrigerator in the full circulating mode and **Fig. 3.3** shows the setup of the dilution refrigerator.

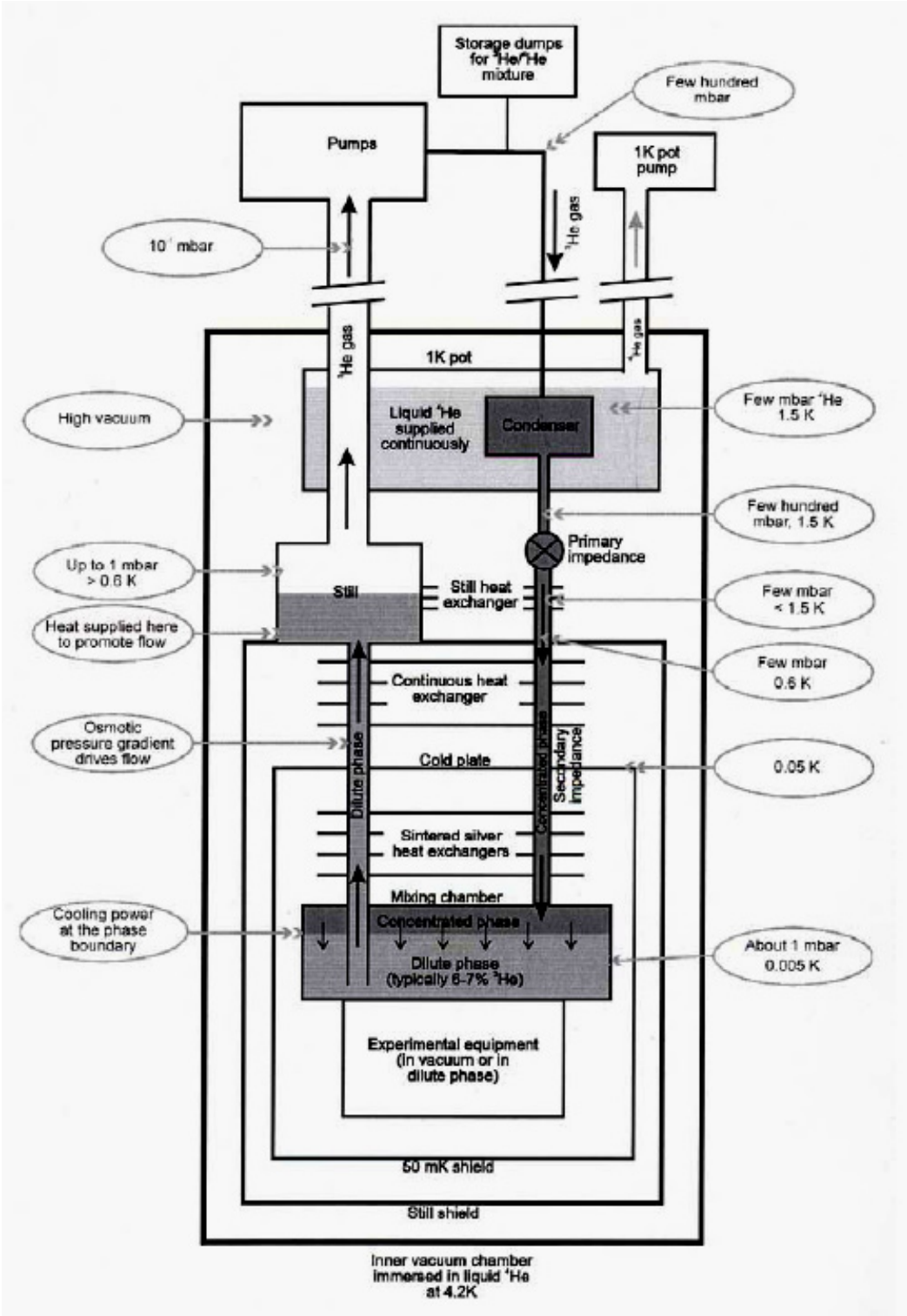

FIG. 3.2 Schematic diagram of the dilution refrigerator [3.1].

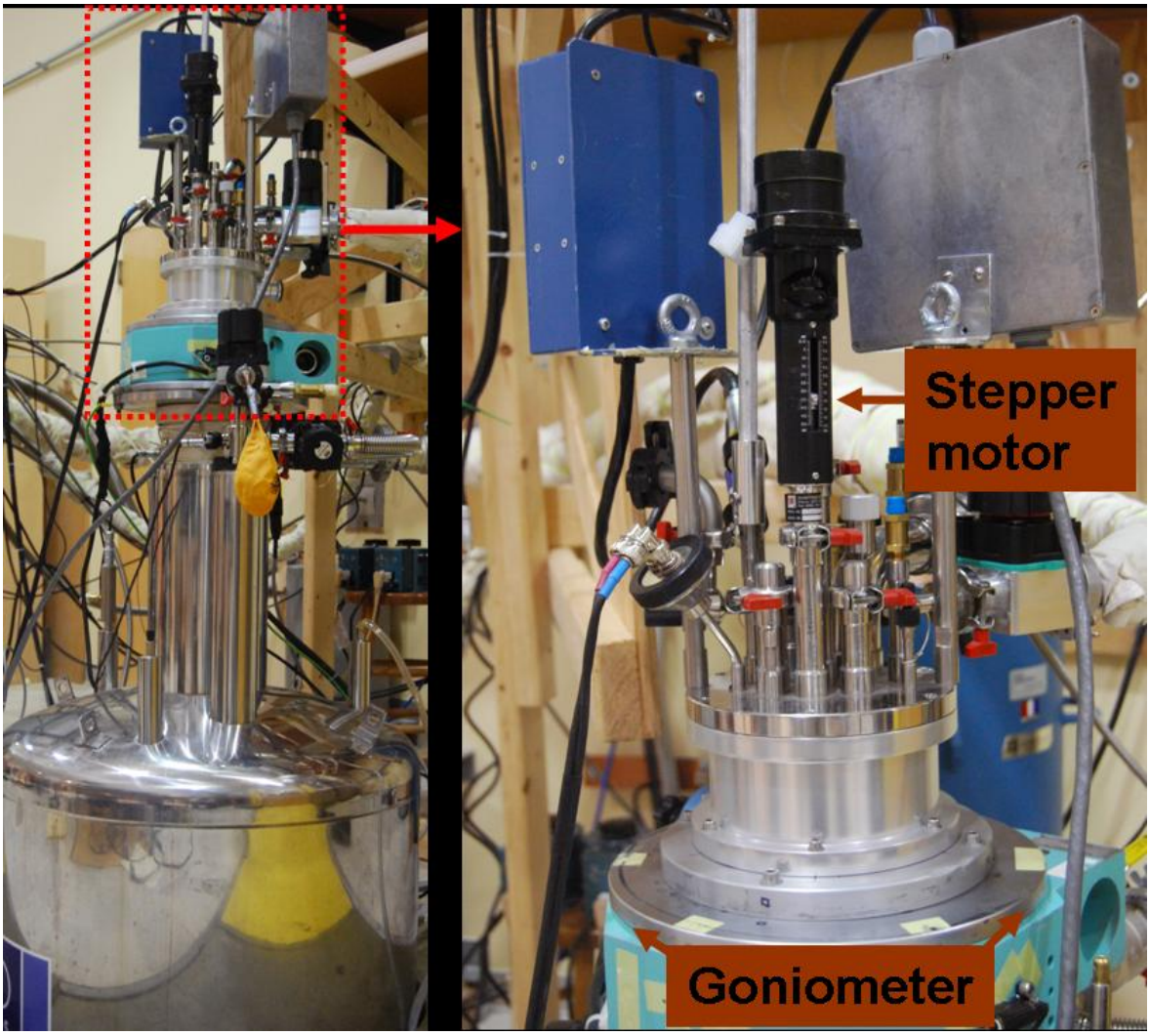

FIG. 3.3 The dilution refrigeration setup used for the present work. The dil-fridge is situated on the goniometer as shown. All possible rotation of steradian of 4π in (θ and ϕ) can be achieved with the combination of stepper motor and goniometer. To avoid any restriction to rotate the fridge, the turntable (not shown in figure) is designed such that, when the *ex situ* goniometer is rotated in one direction, the turntable allow the cryogenic Dewar to simultaneously rotate in the opposite direction, to keep the fridge at the same orientation.

The mixture which is stored in the dumped vessel may contain some impurities (such as N_2, O_2, H_2O vapors etc). This contaminated mixture is thus purified by liquid nitrogen and liquid helium cold traps. When passed through the cold trap, these impurities are condensed on the wall of the traps, not causing any problems in running the dilution refrigerator. The system is pre-cooled down to 77 K with LN_2 and then to ~10 K with the liquid helium. When the system if ~ 10 K, the mixture is condensed into the mixing chamber through the 1K pot that is maintained at a temperature of about 1.6K with the ^{4}He pump. This condensed mixture of about 2.0 K can be further cooled by slowly being pumped with a ^{3}He pump. When the mixture temperature reaches at least 0.86 K (triclinic point), the phase separation of ^{3}He-^{4}He takes place. With the full circulation of ^{3}He, using the ^{3}He pump, the sample space cools down to the base temperature. The detailed operational procedure of Kelvinox^{HE-100} can be found elsewhere [3.1, 3.2].

There are some important factors that make dilution refrigerator work for laboratory uses. Firstly, the amount of ^{3}He and ^{4}He in the mixture need to be chosen properly so that the phase boundary of the two phases is inside the mixing chamber and the liquid phase is in the still pot. Usually, the concentration of ^{3}He is 10-20 %, and total volume of mixture depends on the size of the mixing chamber. In our case, the ^{3}He concentration and the total volume are set to be about 14 % and 53.5 liters, respectively. Secondly, a flow-impedance, denoted as the primary impedance in the figure, is placed underneath the 1 K pot. The primary impedance is usually made of a stainless steel thin rod of about 2 inches long and a little smaller diameter than that of the condensing capillary, and is tightly fitted in the capillary. It plays a role in keeping the pressure of the

condenser in the 1 K pot high enough for 3He gas to condense. Cooperating with the capillary line, denoted as the secondary impedance in **Fig. 3.2**, between the primary impedance and the mixing chamber, it also prevents hot ^{3}He from being fed too fast into the mixing chamber.

The ^{3}He leaving the mixing chamber is used through them to cool the ^{3}He returning into the mixing chamber. While conventional coiled tubular heat exchangers are very effectively used for both the still heat exchanger and the continuous heat exchanger, located above the 50 mK shield, they turned out to be ineffective at very low temperatures because of significant increase of the Kapitza resistance (the thermal boundary resistance) between the liquid mixture and the solid wall of the heat exchanger [3.3]. This shortage is well known to be overcome by coating sintered metals on the solid wall, which can increase the surface area of the solid wall by a factor of 10^5, leading to a great decrease in the Kapitza resistance between the liquid and the solid wall. [3.4] In fact, a sintered silver heat exchanger is used inside the 50 mK shield. Also, silver sinters are coated on the inner surface of the mixing chamber. The use of silver sinters appears to be the most important key element to building modern dilution refrigerators. Caution is made that the dilution unit has to be vented, if necessary, only with a high purity ^{4}He gas since a little contamination of these silver sinters by the atmosphere may result in severe deterioration of the dilution refrigerator. At last, emphasis is made on the still heater that supplies heat on the still pot to keep the still temperature at 0.6 ~ 0.7 K. In doing so, a proper ^{3}He flow maintains to keep the dilution refrigerators in dynamic equilibrium while circulating. Moreover, the still heater can be employed to adjust the cooling power of the dilution refrigerators.

3.3 Operation of Kelvinox^{HE-100}

The first step in the operation of the dilution refrigerator is to make all the electrical connections ready and to evacuate any vacuum parts on the system such as the mixture circulation line, outer vacuum jacket of the Dewar, and so on. The sample was mounted in the rotating platform that is vacuum sealed with indium and all of the electrical connections were then checked. It is always good to monitor the sample while preparing to run the system. If the rotating sample platform is used, it is recommended to check the rotation of the platform before indium sealed. Note that when sealed with the radiation shield and the vacuum can, the sample space must be thermally isolated from the radiation shield and the vacuum can. Also note that the system needs to be helium leak checked after pumped out. Once the leak check is done, the refrigerator is ready to be inserted into the Dewar.

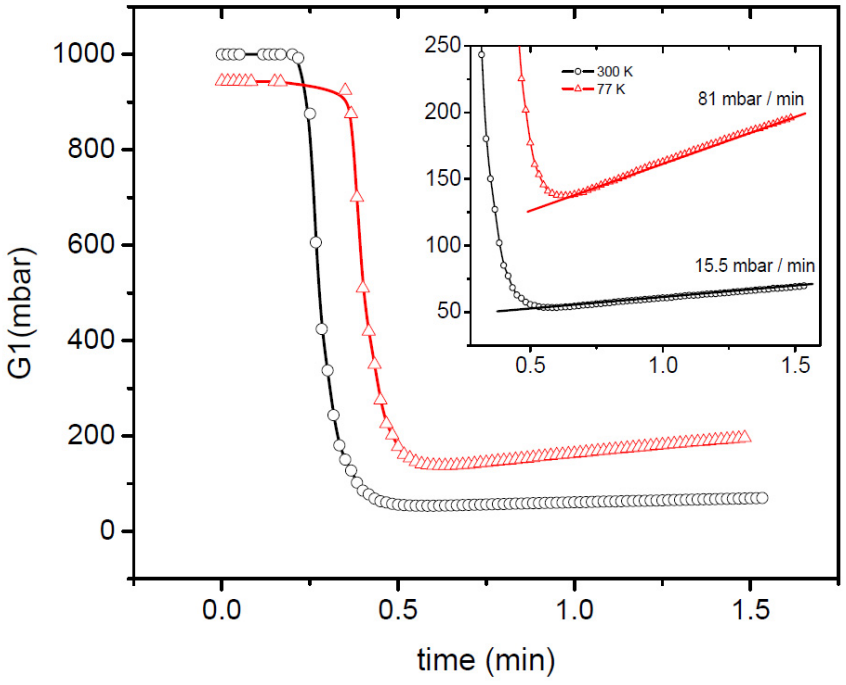

FIG. 3.4 Plot of *G1* pressure versus the time during the throughput test. Inset shows different pressure rise at different temperature.

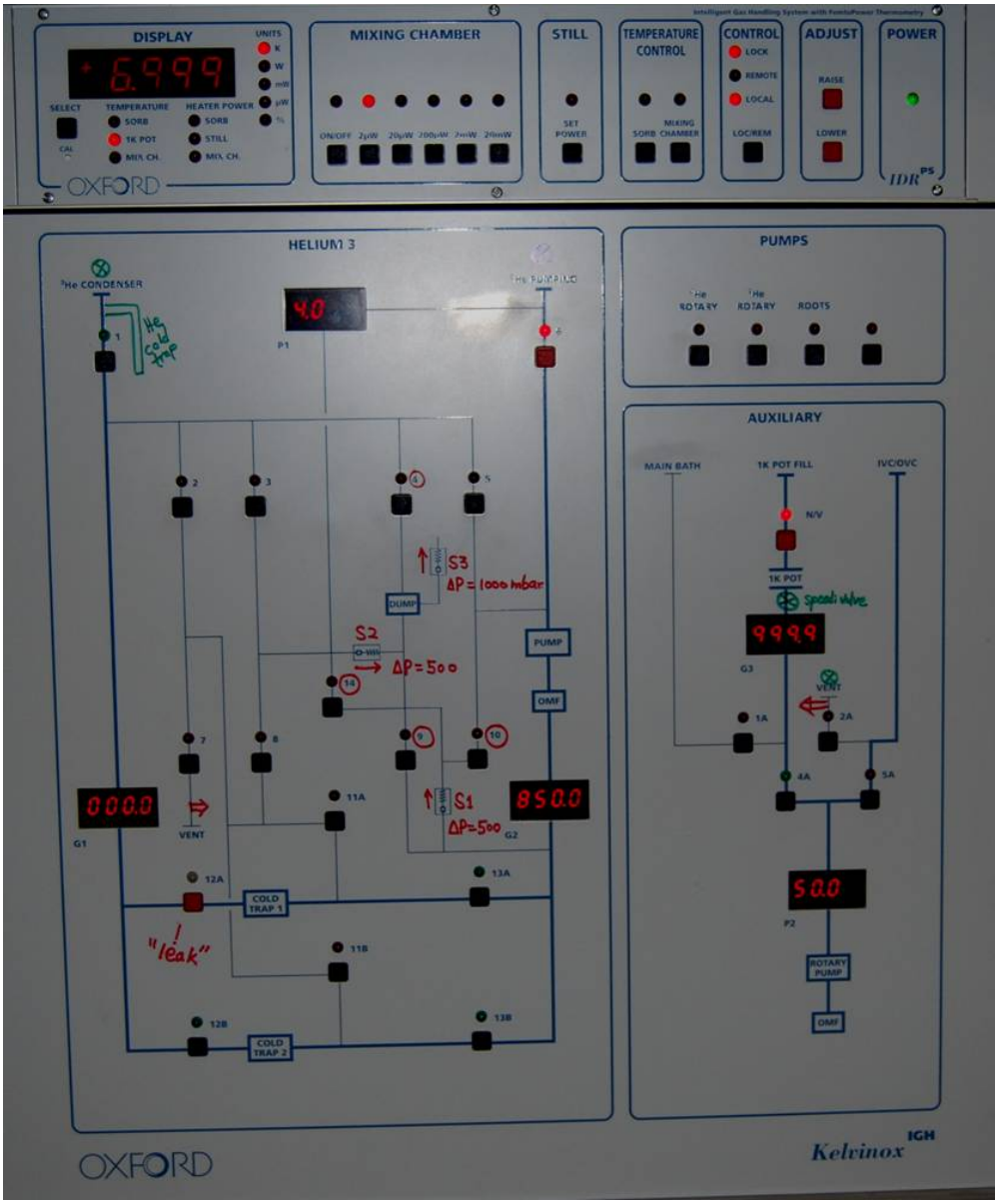

FIG. 3.5 A picture of the front panel of Kelvinox^{IGH}, where the Kelvinox temperature controller is also shown on the top of the Kelvinox^{IGH}. The picture is taken when the system is not being used.

A preliminary step to run the Kelvinox$^{HE\text{-}100}$ is to perform the throughput test at room temperature. This process is necessary to check if there is any blockage in the mixture circulation line. When all the still and pumping lines are connected as described in the manual [3.1], these lines must be evacuated using the ^{4}He pump, by opening the valve 5A, 2A, 7, 11A, 2, 1 and 3 of the Kelvinox^{IGH} front panel [**Fig. 3.4**]. The still line is filled with pure ^{4}He gas through valves 7, 11A, 12A and 3 until the pressure reading on G1 is less then 1 bar. Since the safety valve S2 is connected between the still lines and the dump vessel (mixture), the pressure difference between G1 and the mixture should be less then 500mbar, otherwise there is a probability of losing and contaminating the mixture. Once the pressure reading on G1 approaches 1 bar, valves 7, 11A, 12A and 3 are closed and valve 1 is opened. The pressure on G1 drops quickly and then starts to increase slowly. **Figure 3.5** shows our pressure change on G1. The throughput rate was about 16.6mbar/min (test value at Oxford instruments is 15.5mbar/min). Once the room temperature throughput test is done, ^{4}He gas has to be pumped out and the system is then ready for pre-cooling with liquid nitrogen. Since the sample environment was under vacuum, a small amount of hydrogen gas *(*~ 10 cc*)* was introduced for the controlled cooling of the system.

Once the system is ready to transfer liquid nitrogen (LN_2), it is recommended to transfer slowly in the helium bath and nitrogen jacket. There must be a sufficient amount of LN_2 in the helium bath in order to cool down the magnet around ~77K and also to cover the magnet until blowing the liquid nitrogen out. It is best to transfer LN_2 a day earlier and leave it overnight. Once the temperature of the magnet reaches ~77K (sample temperature may be slight higher ~80K), the second throughput test at this temperature

might be desired. The next step is to blow out the liquid nitrogen from the helium bath. ^{4}He gas of pressure 1-2 psi was used to pressurize the bath and LN_2 was collected. To blow out the LN_2, the blow out tube has to be inserted all the way down (which is the top position of the magnet). Once there is no more LN_2 coming out from the tube, the helium bath is pumped with the ^{4}He rotary pump to make sure there is no LN_2 in the helium bath. If the pressure of the helium bath passes through the 100mbar smoothly, it can be assumed that there is no more LN_2 inside the bath. At this point, the helium bath needs to be pumped and flushed with pure ^{4}He gas at least twice, and the opening of the 1K pot needle valve should be checked as well. If the lambda point refrigerator is used, a couple of pumping and flushing of the lambda point refrigerator is desired. At the end of the final flushing, the needle valve of lambda point refrigerator should be left open until the end of liquid helium transfer.

Now, the system is ready for transferring liquid helium. A slow transfer of liquid helium is recommended. This can be controlled by monitoring the temperatures of the sample and magnet so that they can be cooled at the same rate (temperature difference is usually 5-10 K). One important thing to keep in mind is that a rapid cooling may cause the H_2 exchange gas in the refrigerator to freeze at higher temperature than required to run the system. While transferring the liquid helium, the sorb heater is kept at ~ 100 K until the temperature of the sample space goes below 20 K. At the end of the transfer, the sample temperature should reach 8-10 K, for which the dilution refrigerator can be operated.

The next step is to cool the system down to the base temperature. The Kelvinox^{HE-100} is designed to run the system automatically from this point. This can be

done by manually opening the two storage dump valves, *1K* pot valve, still valve, and return line valve. Once this is done, the automatic operation can be performed by clicking three icons in a row in *KelvFrontPanal.vi*: **Fill 1K Pot, Condense in and Circulate**. The cooling sequence will run one after another and the base temperature can be reached within 2-3 hours. However, the refrigerator has been operated manually for this work.

For manual operation, the first step is to open the 1K pot needle valve about 10% and open the KF-25 speedivalve on the fridge while pumping on 1K pot. The opening of needle valve can be controlled by monitoring the pressure reading on P2. The pressure reading of P2, about 5-6mbar, gives rise to the temperature of 1.6K on the 1K pot. When the 1K pot reaches ~ 1.6 K, the system is ready for condensing the mixture. The condensing process begins with opening the valves: the two dump valves, 9, 13A, 1, 3, the 3He return valve, and the still valve. While doing so, the mixture goes through the liquid nitrogen and liquid helium cold traps. The condensing process starts once the valve 12A is opened by a small amount. The valve 12A has to be open in such a way that the pressure reading on G1 is less than 200mbar. If the pressure reading on G2 is less than 100mbar with the valve 12A opened fully, the initial condensation of the mixture is done. At this stage, the temperature of the sample is about ~1.8K. Then, the valve 9 and 3 is closed and valve 14 is opened to collect the remaining mixture in the dump (the valves on the dump vessel should be open until the end of experiment. Simultaneously, without any delay, the opening of the valve 6 by 11% triggers the circulation of mixture. The opening of valve 6 is gradually increased in such a way that the pressure on G2 is below 200mbar. During this circulation, the temperature of the sample space

(temperature of mixing chamber) decreases. When the sample temperature is ~ 1.3K, the Pirini gauge *P1* will come to its working range and the pressure reading on P1 decreases on further cooling. When the pressure reading on G2 < 200mbar and P1 < 10mbar, valve 14 must be closed and valve 6 can be opened fully, depending on the desired cooling rate. When the pressure reading on *G2* falls below 140mbar, the still heater is turned on. The power required on the still heater, for the proper cooling, is about 6mW. The base temperature of approximately 20mK will be then achieved in one hour.

To keep the system running, the liquid helium level has to be greater than 50% for our Dewar and the liquid nitrogen bath should be always full. The amount of the liquid helium consumption depends on the working environments, such as the temperature and the magnetic field. The sample temperature was monitored, while the system was cooling down from room temperature to 4.2K, using Cernox (*LakeShore* model *CX-1030-SD*) resistance thermometer; a separate mixing chamber thermometer (RuO_2 resistance) was used below 4K or 5K. Also, we used another RuO_2 thermometer mounted on the sample platform.

3.4 Split-coil Magnet and Dual Axis Rotation

Split-coil magnet, also known as split pair magnet, is the two horizontal magnets made of Nb_3Sn superconductors, used to achieve high horizontal magnetic fields. The use of two rotator and the split-coil magnet allows us to measure angular dependence for all possible angles. The most common use of dual-axis rotation is, nowadays, a combination of an external (*ex situ*) rotator and an internal (*in situ*) rotator as shown in **Fig. 3.6**. The *ex situ* goniometer gives a complete rotation of the fridge about the center

vertical line of the fridge itself, whereas the *in situ* rotator allows the sample stage to rotate about an axis in a plane normal to the fridge. For this work, we used an Oxford Instruments made split-coil magnet with a 40mm access gap, and two rotators that include a commercially-made goniometer (Huber model 420) and a home-made *in situ* rotator. The split-coil magnet uses an IPS120 magnet power supply that can produce magnetic fields up to 12T (≡ 105.51 A) at 4.2K or up to 13.5T (≡ 118.70 A) at 2.2K. During this work, the maximum field employed was 9T.

The rotational sample holder was made of OFHC (oxygen free high conductivity) copper, giving good thermal link between the mixing chamber and the sample stage. The $(DMET)_2I_3$ sample was mounted on the sample stage. On the backside of the sample platform, a flat Minco 75□ local heater and Cernox (*LakeShore* model *CX-1030-SD*) temperature sensor were mounted along with 12 twisted paired wires. As depicted in **Fig. 3.6** (also in **Fig. 3.3**), the dilution refrigerator was placed on the goniometer, providing a complete 360° rotation and very accurate rotation of the refrigerator (□□= 0.0025°). This high angular resolution is necessary to accurately align our sample with respect to the sample. The refrigerator was connected to electronics as well as pumping lines from the Kelvinox^{IGH}. To avoid any restriction of rotation of the refrigerator, a turntable was designed such that, when the *ex situ* goniometer is rotated in one direction, this turntable allows the cryogenic Dewar to simultaneously rotate in the opposite direction, to keep the refrigerator at the same orientation. Otherwise, the rotation of the fridge will be constrained by the length of the still pumping line, which is the shortest line attached on the fridge from the Kelvinox^{IGH}.

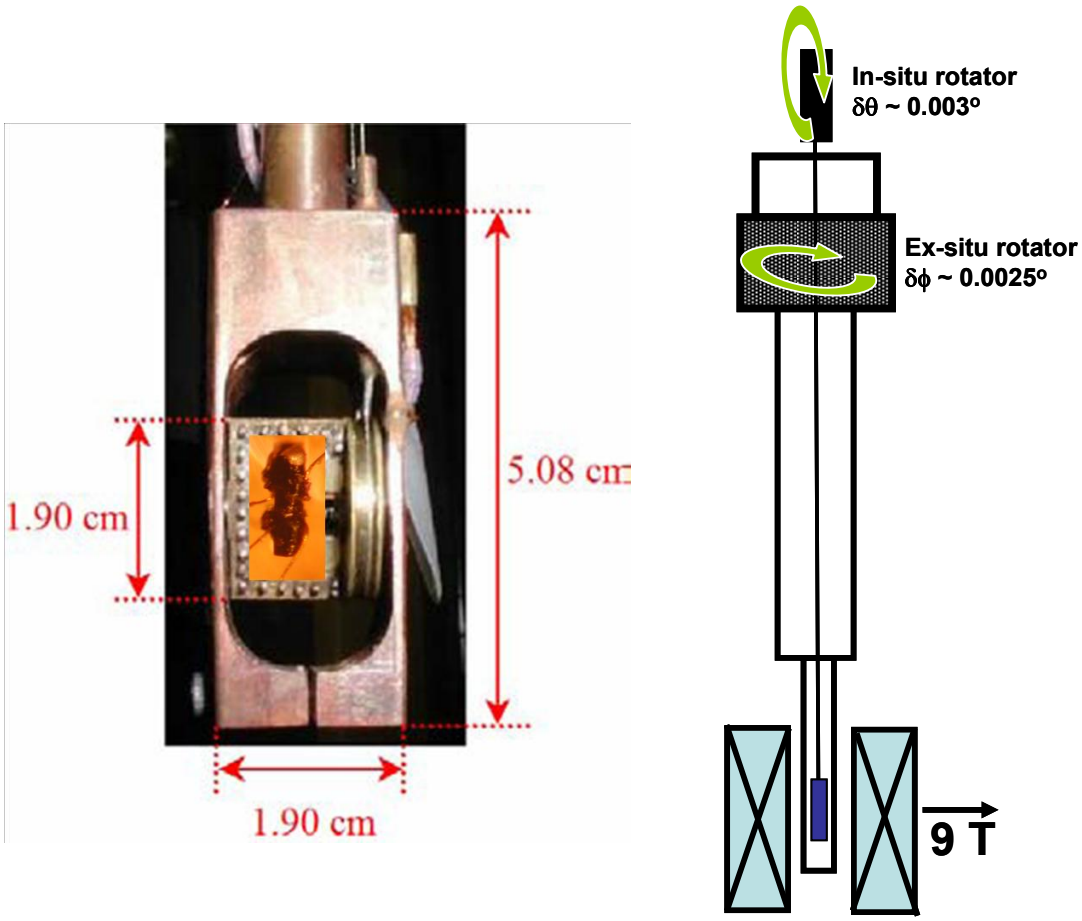

FIG. 3.6 Photograph of the rotating sample holder (left) and schematic diagram of the dilution refrigerator in the split-coil superconducting magnet (right).

The use of the rotator can produce the temperature fluctuation during the measurement. It was found that while rotating the refrigerator using goniometer (*ex-situ* rotator), there was a small fluctuation in temperature (<5 mK). But, the *in situ* rotator can easily cause excessive sample heating at low temperature due to friction, since the sample was directly mounted on the rotator. In order to prevent possible excessive frictional heat, a string-driven (Spectra-1000 fiber) *in situ* rotator was employed instead of a gear-

driven rotator for this work. This Kevlar-based fiber string, which has very poor thermal conductivity, has some linear expansion at low temperatures. For compensation, three beryllium copper springs (with spring constant k = 95.8N/m and 168mm free length, annealed for 2 hours at 130°C), were used to adjust the variation of string length. By a release or pull of the linear positioner in step units, where 1 step gives 0.8125μm displacement of the linear positioner, an angular resolution of $\delta\theta \sim 0.003°$ was obtained.

3.5 Measurement Technique

The conventional 4-probe method combined with AC Lock-In technique was used for all transport measurements. Electrical contacts on the sample of the dimension ~ 0.5 x 0.3 x 0.15 mm^3 were made by attaching 12μm gold wires with conducting carbon paste. The schematic diagram of the electrical connection as well as the real sample used during the experiment is shown in **Fig. 3.7**. Two temperature sensors have been mounted: one is a Cernox (*LakeShore* model *CX-1030-SD*) sensor for high temperature valid above 2K, and the other is a RuO_2 (R = 1004 Ω at room temperature) for monitoring low temperature (valid below 6.5 K). The RuO_2 sensor had been previously calibrated at zero magnetic field with respect to the Oxford Instruments supplied RuO_2 mixing chamber thermometer. Note that temperatures of the mixing chamber and the sample turn out to be nearly equal. In other words, the sample platform and mixing chamber was nearly in thermal equilibrium.

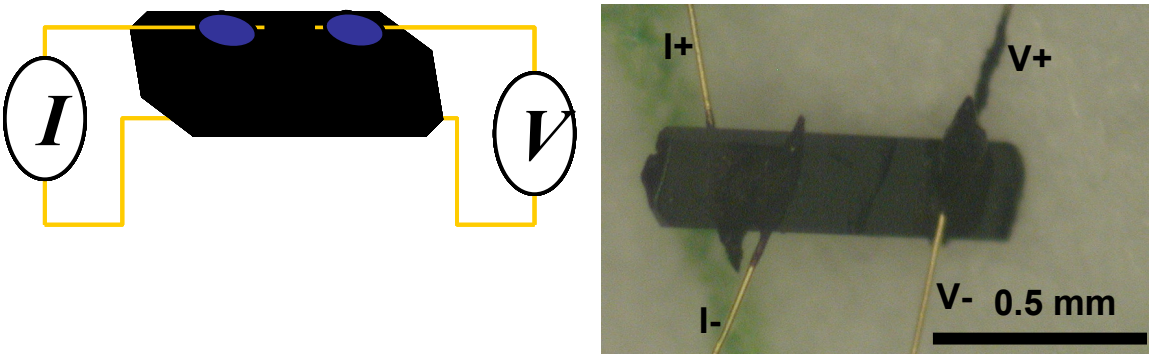

(a) (b)

FIG. 3.7 (a) Schematic picture (b) the sample with the four 12 μm gold wire connected to the sample with graphite paste for 4-probe measurement on $(DMET)_2I_3$.

Typically, measurement currents of 1μA (~10^{-3} A/cm^2) with low frequency (< ~300Hz) were employed to monitor the interlayer resistance (R_{zz}) by using a Stanford Research Systems 830 lock-in amplifier. A Stanford Research Systems 560 low-noise preamplifier was also used to amplify the signal as well as filter out noise. In addition to the sample measurement, the *CX-1030-SD* thermometer was measured by using Lakeshore 340 temperature controller and Linear Research Inc LR700 ac Resistance Bridge. The LR-700 ac Resistance Bridge was used to measure the resistance of our RuO_2 thermometer. A home-written Labview code was used for data acquisition as well as electronic control, via a GPIB parallel port. Also, RS-232 serial ports were used to control the goniometer and stepper motor, whereas the magnetic field and the mixing temperature were measured via LAN (Local Area Network).

3.6 References

[3.1] Kelvinox User's Manual, Oxford Instruments.

[3.2] J. I. Oh: Ph. D. dissertation, Boston College (2003).

[3.3] P. L. Kapitza: J. Phys. USSR **4**, 181 (1941).

[3.4] R. C. Richardson, E. N. Smith: *Experimental techniques in condensed matter physics at low temperature*, Addison Wesley, 159 - 164 (1988).

Chapter 4

Angular Magnetoresistance Oscillations (AMRO) in $(DMET)_2I_3$: Experiment and Calculation

4.1 Introduction

Quasi-one-dimensional (Q1D) molecular conductors are highly anisotropic materials which show remarkable oscillatory magnetoresistance phenomena with respect to magnetic field orientation [4.1]. Several related types of so-called angular magnetoresistance oscillations (AMRO) have been observed in many families of Q1D conductors, as well as in quasi-two-dimensional (Q2D) conductors. In Q1D, Lebed magic angle (LMA) resonances [4.2-4.6] [**Fig. 2.5**], Danner-Kang-Chaikin (DKC) oscillations [4.7] [**Fig. 2.7**], and the Yoshino angular effect (YAE) [4.8, 4.9] [**Fig. 2.9**] have been observed for field rotations about the three principle axes *x*, *y* and *z,* respectively, as shown in **Fig. 1.7** and **Fig. 1.15**. In addition, more complex Lee–Naughton (LN) oscillations are observed when the magnetic field is rotated in arbitrary (out-of-plane) directions [4.10, 4.11, 4.12] as shown in **Fig. 2.11**.

While such AMRO effects have been observed in many Q1D materials, their origin(s) and relationships to each other have puzzled researchers for over two decades. Several theoretical models have been put forth to explain interlayer AMRO in Q1D materials [4.13-4.21] . Some observed effects (DKC, YAE, and LN) are qualitatively explained by the above-referenced models. For magnetic field rotation in the least conduction *y*-*z* plane (*i.e.*, about *x*-axis), however, these theories have consistently failed to explain or reproduce in simulations, the first experimentally observed effect, the Lebed

magic angle effect. The models in Refs. [4.18 - 4.21] result in a similar expression for the interlayer conductivity, though with slightly different starting assumptions, that can be used to qualitatively reproduce many observed AMRO features, excluding the Lebed effect. According to these models, the conductivity is modulated by a series of n^{th}-order Bessel functions that themselves are functions of the magnetic field ratio B_x/B_z, where x and z are the most and least conducting directions, respectively. When the field is rotated in the crystal y-z plane, all of these Bessel functions vanish, with the exception of that for $n = 0$, and the resulting resistivity has a smooth, featureless variation with field angle. In particular, no Lebed oscillations appear, even though this is the orientation (rotation) plane in which the Lebed effect is both conceptually anticipated and experimentally observed. Based on experimental data and theoretical models, the authors of Ref. [4.22], nonetheless assert that Lebed oscillations are the only "fundamental effect", with all other AMRO effects (DKC, YAE, and LN) being mere modulations of this master effect. This contention is arguable since, experimentally, the observed oscillation amplitudes decrease as the field direction approaches the y-z plane, where the Lebed effect is expected to be strongest. Furthermore, higher order oscillations fully vanish when the field direction approaches the y-z plane [2.11, 4.22].

In a slightly alternate theoretical approach, Lebed and Naughton [4.19] proposed that an "*interference effect*" between the velocity of electrons in the Q1D FS and the variation of the density of states across this FS gives rise to 1D-2D dimensional crossovers, which appear to result in peaks of the calculated interlayer conductivity at the correct magic angles. To date, all available theoretical models have been derived based on an orthorhombic approximation to the actual triclinic crystal structure of the materials

in which the AMRO effects have been seen. None of these models reproduce the Lebed AMRO effects, except for the above "interference model", which assumes density of state variations for electrons across the FS for which little if any experimental support exists. Here, we have measured the interlayer magnetoresistance of Q1D conductor, $(DMET)_2I_3$, which has similar crystal structure to that of $(TMTSF)_2X$, for all angular orientation of magnetic field, and have simulated the same via numerical calculations employing the actual triclinic crystal structure. This constitutes the first use of the correct crystal symmetry in such calculations. These simulations reveal, for the first time, the Lebed oscillations in the predicted *y-z* plane.

4.2 Experimental Results

Experimental data for the temperature dependence of the resistance of $(DMET)_2I_3$ is shown in **Fig. 4.1**. This was measured using the 4-probe measurement technique [**Fig. 3.8**], using 1 μA rms with 77.77 Hz lock-in frequency. The room temperature resistivity is ~ 200 μΩ–cm, indicating good metallicity. Conventional metallic behavior ($dR/dT < 0$) is seen upon cooling, with a superconducting transition observed ~ 0.58K. It was found elsewhere that the spin density wave phases induced by a magnetic field occur in fields greater than 10 T [4.6]. Here, an applied magnetic field of 9T will always be below the minimum of the threshold field for FISDW transition. This, in turn, ensures the system is always in the normal metal (field is too small for FISDW and too large for superconductivity). This contrasts with all previous AMRO studies in Q1D systems, where complicated mixtures of metallic and SDW states occurred in measured magnetic fields, tending to complicate interpretation of data.

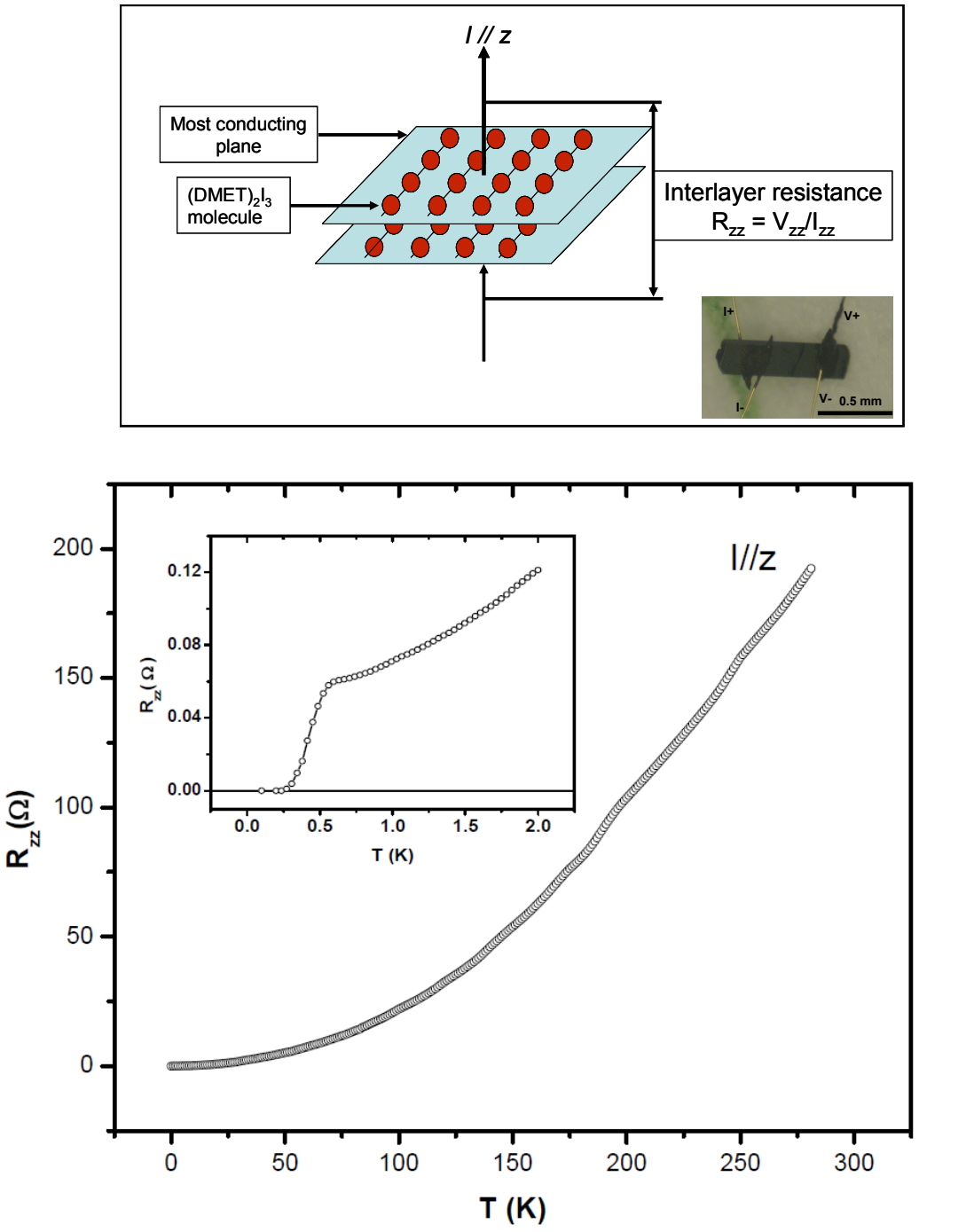

FIG. 4.1 (Upper) interlayer resistance measurement scheme used showing the real crystal of $(DMET)_2I_3$ in lower right corner. (Lower) the temperature dependent interlayer resistance of $(DMET)_2I_3$ with *I//z* – axis (i.e., current is perpendicular to the most conducting plane). The resistance of the sample is measured using 4-probe technique. The sample shows conventional metallic behavior upon cooling with a superconducting transition ~ 0.58K. Inset shows the low temperature part of the resistance showing the clear superconducting transition.

The interlayer resistance $R_{zz}(\theta,\phi)$ was measured for two comparably-sized $(DMET)_2I_3$ samples as a function of different angle orientations in a magnetic field. One rotation angle θ was varied by rotating the magnet about the vertical while keeping the sample stationary, whereas a second, perpendicular rotation angle ϕ was controlled with an external stepper motor driving an internal Kevlar string attached to an internal rotation platform. Note that the angle θ is measured from the *z*-axis and the angle ϕ is measured from *x*-axis unless otherwise defined. We obtained data for both samples, simultaneously. Sample #1 exhibited a residual resistivity ratio ($RRR = \rho_{T=300K} / \rho_{T=4K}$) of 3,000, compared to 1,000 for Sample #2. Although both samples showed qualitatively similar results, so we concentrate on the better sample #1 in most of the following discussion.

Similar sets of experiments were carried at out two different times. For the first set, only sample #1 was measured, with data recorded every 0.5^o of θ, from $\theta = -100^o$ to $\theta = +100^o$; and every 5^o of ϕ, from $\phi = -45^o$ to $\phi = +135^o$. The resistance was always measured by varying the angle θ, keeping angle ϕ constant. Whereas, in the second set of experiments both samples #1 and #2 were simultaneously measured for resistance for the field in, and in the vicinity of the *y*-*z* plane (Lebed plane). The measured resistance (raw data) as a function of θ for various ϕ from the first set of experiment (sample #1) is shown in **Fig. 4.2**. As expected, remarkable oscillations in resistance is observed for all angular orientation of the magnetic field with respect to the sample.

As discussed in Chapter 2, the *y*-*z* plane rotation of magnetic field is where the first predicted and observed AMRO effect occurs in Q1D systems. The facts that some theoretical models predict the absence of Lebed oscillations and a vanishing of the amplitudes of those oscillations, as the magnetic field rotation plane approaches the *y*-*z*

plane, motivated us to measure the resistance of the sample with finer angular spacing (that is $\delta\phi = 2^o$). Thus, in second set of experiment, the resistance for the field rotated near the *y*-*z* plane, was measured for every 2^o of ϕ, as shown in **Fig. 4.3** for sample #1 and sample #2. As discussed earlier, the resistance has pronounced oscillations for a field rotation in every rotation plane.

Figure 4.4 shows the expanded view of data for sample #1 for angular span of $15^o \leq \theta \leq 60^o$ (right) and $-15^o \leq \theta \leq -60^o$, to see the closer look on resistance oscillations. In these angular span lower order oscillations with indices $n = \pm 1, \pm 2$, and ± 3 are visible. The amplitude of oscillations in resistance in positive θ direction is bigger then on negative θ direction. Furthermore, the dips in resistance in positive θ are more sharper then in negative θ. We believe that this asymmetry arises due to the triclinic crystal symmetry and (or) due to the slight misalignment of the sample with respect to magnetic field during the measurements. Looking at these angular spans, the amplitude of the oscillations decreases with the increase in angle ϕ and becomes minimum for angle $\phi = 90^o$. Upon further increase in θ angle the amplitude oscillations again increases. The more quantitative analysis of this feature will be presented later in this chapter.

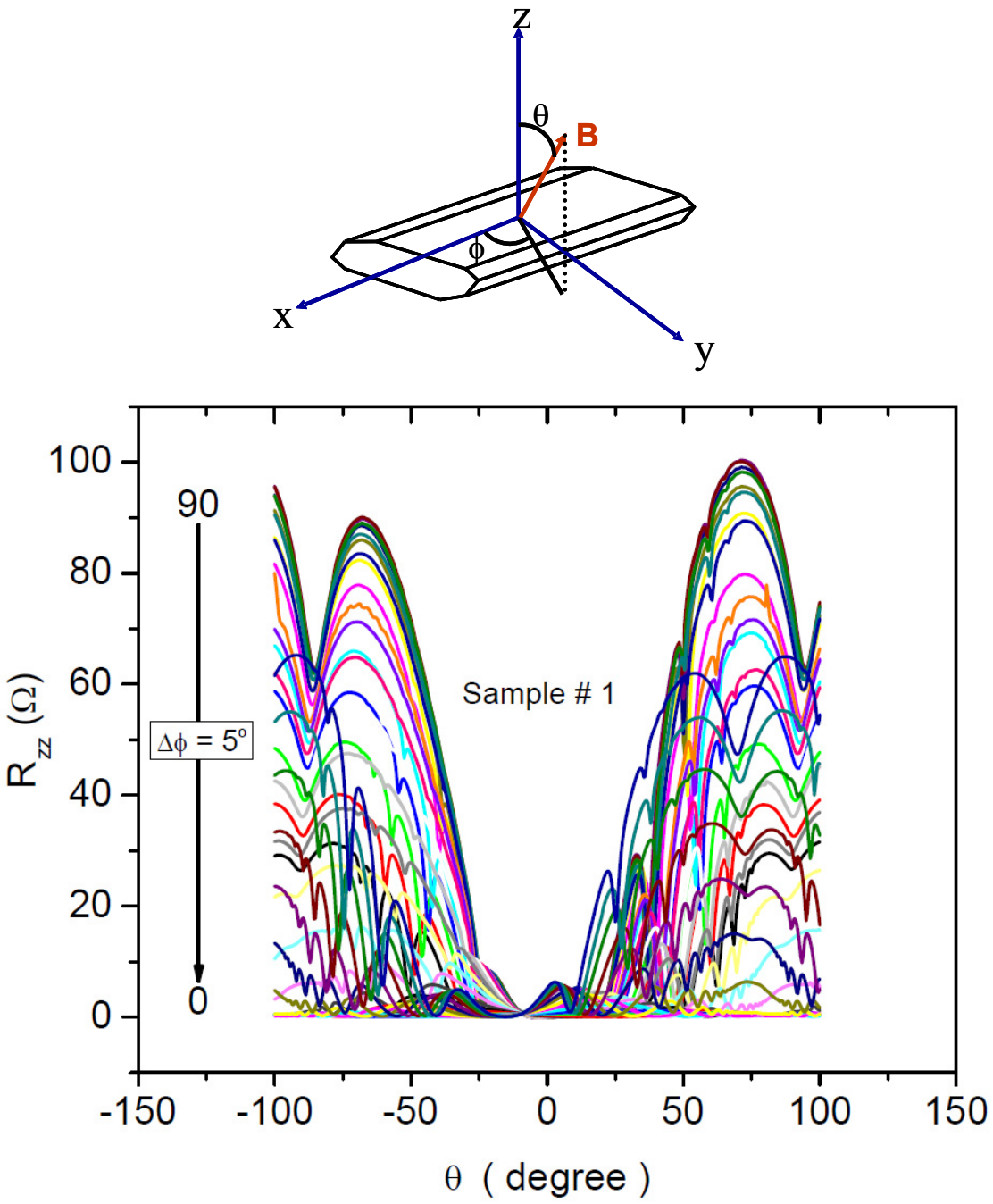

FIG. 4.2 (Upper) the sample orientation in magnetic field. (Lower) Measured interlayer resistance (raw data) as a function of polar angle θ for different azimuthal angle ϕ at magnetic field 9T and 100 mK temperature for sample #1. The data are measured for every half degree of θ, from -100^{o} to $+100^{o}$, and every five degrees of ϕ, from -45^{o} to $+135^{o}$. The plot shown is only labeled from $\phi = 0^{o}$ to $\phi = 90^{o}$ as the curve for $\phi = 80^{o}$ approximately the same as that for $\phi = 100^{o}$, and so on. The resistance has pronounced oscillations for a field rotation in every rotation plane.

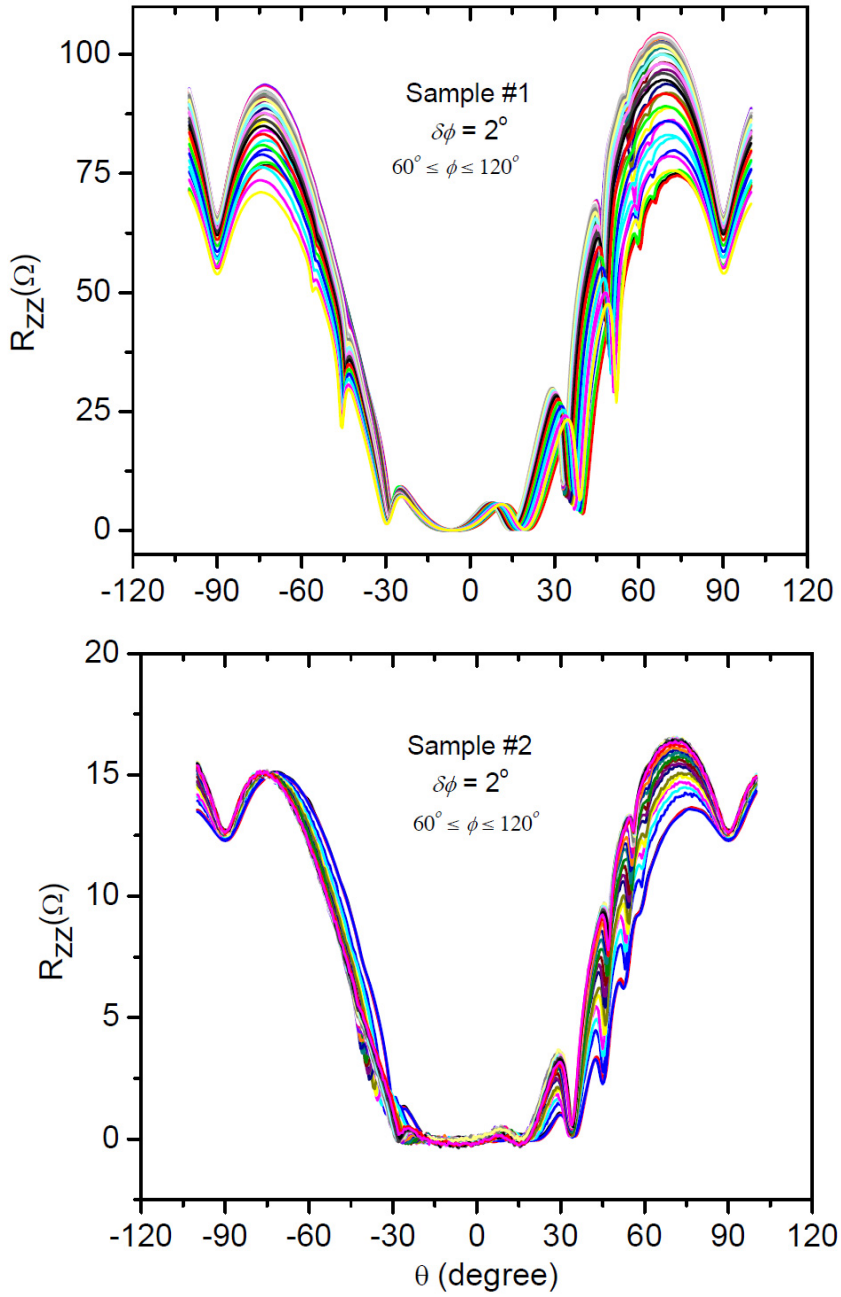

FIG. 4.3 Measured interlayer resistance at different ϕ angles at B = 9T and T =100 mK for sample #1 (upper) and sample #2 (lower). The data are measured for every half degree of θ, from -100^{o} to $+100^{o}$; and every two degrees of ϕ, from 60^{o} to 120^{o}. The resistance has pronounced oscillations for a field rotation in every rotation plane.

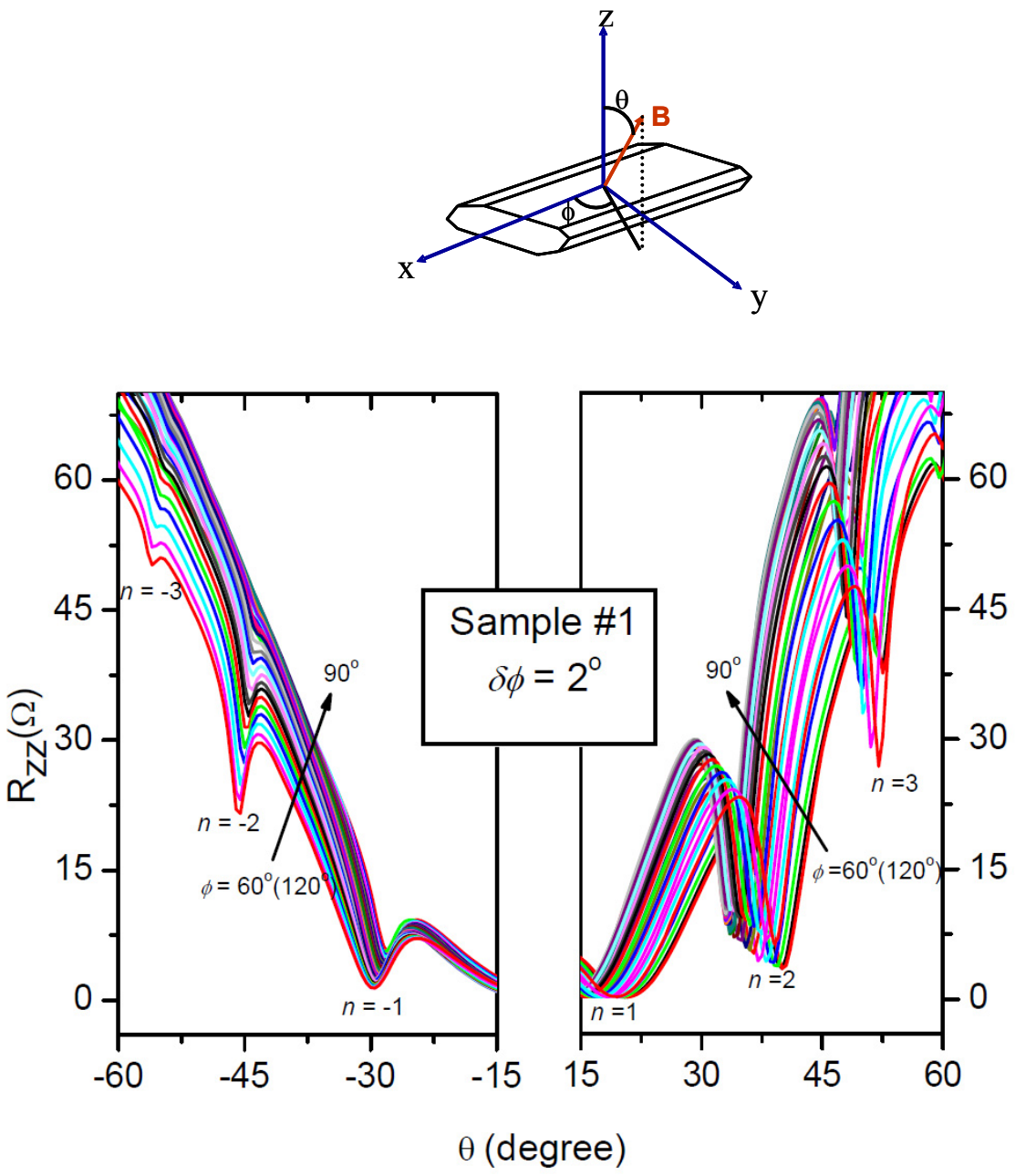

FIG. 4.4 (Upper) the sample orientation in magnetic field. (Lower) measured interlayer resistance as a function of θ angle at different ϕ angle at B = 9T and T = 100 mK for sample #1, showing only the low-index oscillations (n = ±1, ±2, and ±3). The θ–dependence of resistance is measured for every 2° of ϕ angle from 60° and 120°. The resistances of the sample for angles 60° and 120° are approximately equal. Finite difference in resistance for angle ϕ = 60° and 120° is expected due to the tricilinicity of crystal structure.

Now, we have plotted the measured interlayer resistance as a function of θ for different ϕ angle with vertical offset for clarity. The curve for a given ϕ represents a magnetic field rotation plane. For $\phi = 0°$, the field is rotated in the *x*-*z* plane as shown in the schematic diagram in **Fig. 4.5**. Even though, the oscillations are not visible in this plot (will be presented separately later), this plane represents the plane where DKC oscillations are observed in the family of TMTSF Q1D systems. In present experiment, for the first time, we have observed the DKC oscillations near $\theta = -90°$ and $+90°$ for $\phi = 0°$. On increasing the angle ϕ, the field rotation plane moves towards the *y*-*z* plane. In doing so, the more pronounced oscillations in resistance are observed as seen in **Fig 4.5**. For angular position of $\phi = 90°$, the Lebed oscillations (LMA) are observed as indicated by thick solid line in **Fig. 4.5**. However, the oscillations, which were pronounced while the field rotation plane moves from $\phi = 0°$ towards $\phi = 90°$, becomes bigger for $\phi \approx 45°$, and decreases when the rotation plane becomes $\phi = 90°$. In other words, the amplitude of oscillations in resistance increases and again decreases when the magnetic field rotation plane moves from *x*-*z* plane to *y*-*z* plane.

Nonetheless, the present measurement is done changing θ angle and keeping ϕ angle fixed, we can extract the data for different ϕ with constant θ angle. In doing so, the YAE effect is observed for the field rotating in a plane with $\theta = \pm 90°$, *i.e.*, for the field rotation in the *x*-*y* plane. The detail origin of these oscillations was presented in chapter 2 and more explanation of this effect in this present experiment will be presented later in this chapter. Even more complex oscillations called LN oscillations are observed when the sample is rotated in a plane while keeping θ angle constant. Thus, all four kind of

oscillations observed in the family of Q1D (mostly in $(TMTSF)_2X$) are now observed in present single experiment.

Assuming the 180° ϕ angle symmetry in the resistance data, we have plotted the resistance data as shown in **Fig 4.5** in to polar plot for an illustrative purpose, for an angular span of θ = 0° to 360° for every 5° of ϕ from 0° to 180° covering all 4π steradian, however, in conventional co-ordinate system, θ varies from 0° to 180° and ϕ varies from 0° to 360°. The resistance shows the complicated oscillations as a function of angular orientations. The angles $\theta = 90^o$ and 270^o represents the field parallel to the *y*-axis, whereas the angular position of $\theta = 0^o$ (180^o) is parallel to *z*-axis. The oscillations are observed in LMA, DKC, YAE, when the magnetic field is rotated in three principal planes, *y*-*z*, *z*-*x*, and *x*-*y*, respectively. The LN oscillations are originally introduced as ϕ rotation with constant θ angle. From this plot, it is much clear that, the oscillations in resistance are observed in any possible rotation plane of magnetic field.

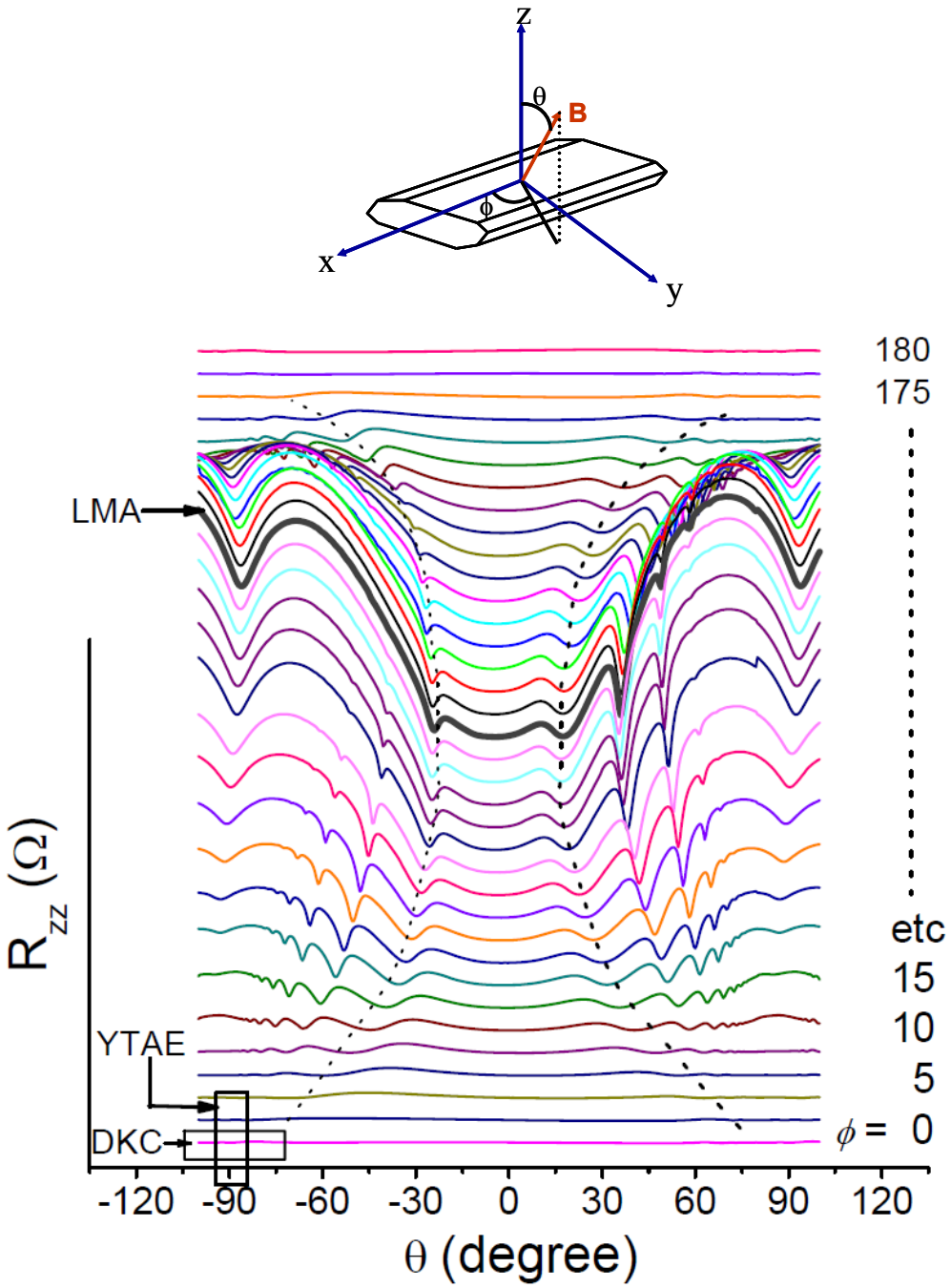

FIG. 4.5 (Upper) the sample orientation in magnetic field. (Lower) measured interlayer resistance as a function of polar angle θ for different azimuthal angles ϕ at $B = 9$T and $T = 100$ mK for sample #1. The data are measured for every 0.5° of θ, from –100° to +100°; and every 5° of ϕ, from 0° to +180°. The plot is vertically offset for clarity and the curved dashed line is to guide the lowest order oscillation ($n = \pm 1$).

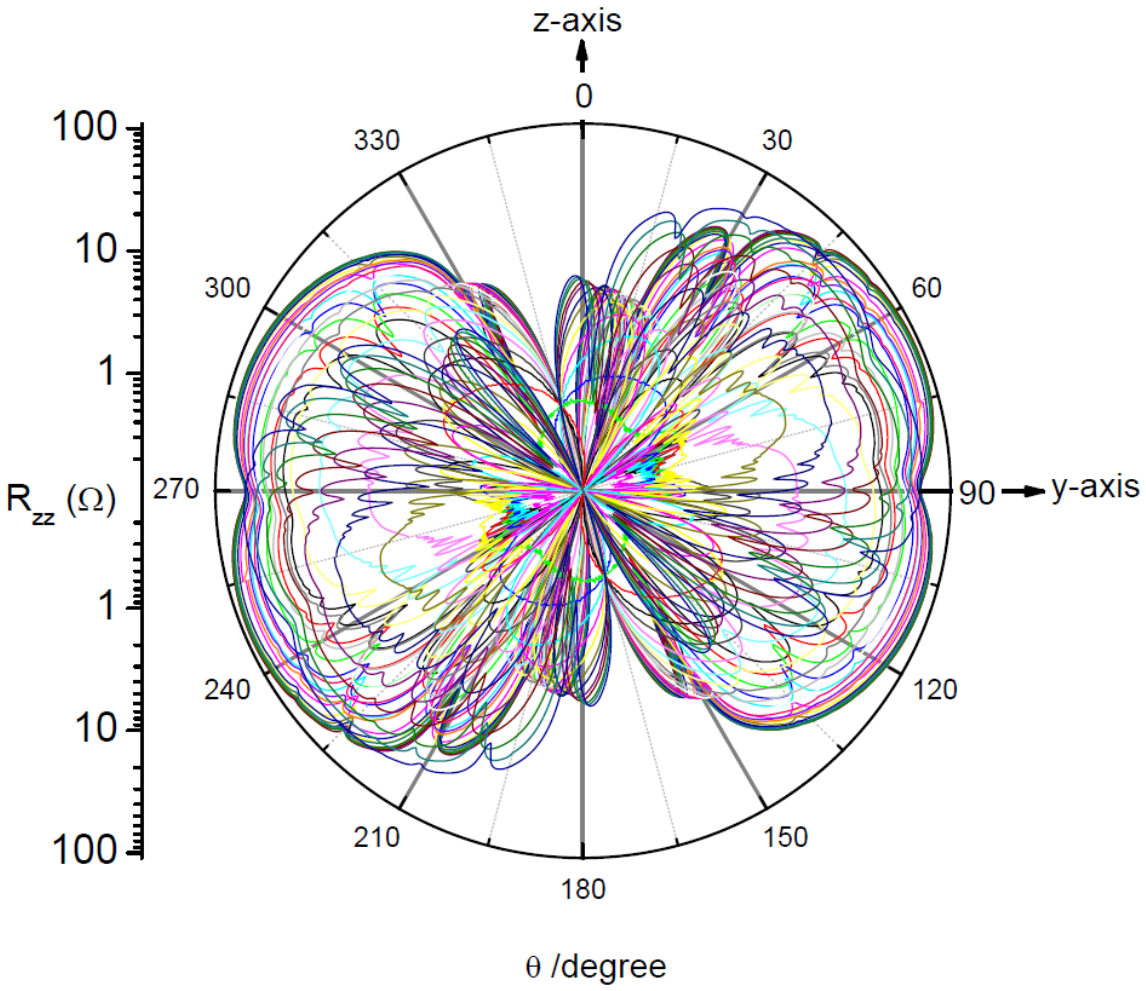

FIG. 4.6 Polar plot of the measured resistance from **Fig 4.5** for all possible angular orientation of magnetic field of strength 9T at 100 mK. Resistance is plotted for every 5° of ϕ, from 0° to 180° and every 0.5° of θ, from 0° to 360°. The angular orientation of magnetic field covers all 4π steradian. The resistance shows the complicated oscillations as a function of angular orientations. The angles $\theta =$ 90° and 270° represents the field parallel to the *y*-axis, whereas the angular position of $\theta = 0°$ (180°) is parallel to *z*-axis.

As presented in **Figs. 4.2 - 4.6**, the resistance shows pronounced oscillations when the magnetic field is rotated in different planes. The numbers of oscillations as well as their amplitudes are not symmetric about $\theta = 0^{o}$, and higher order oscillations observed when the field rotation plane moves away from *y-z* plane. This nonsymmetric feature in may arise from slight misalignment of sample during the measurement. In the above experimental data, the resistance has its lowest value at about $\theta \approx 8.5^{o}$ corresponding to magnetic field parallel to the *z*-axis and the resistance has a dip at the angle $\theta = \pm 90^{o}$ corresponding to the magnetic field parallel to *x-y* plane.

In most of the above discussion, we have presented the data from sample #1 (except in **Fig. 4.3**). A comparison of the resistance measured for the two samples #1 and #2, for the magnetic field rotating in *y-z* plane, is shown in **Fig. 4.7**. The measured resistance of these two samples is qualitative in agreement with each other, meaning the oscillations in resistance coincide to each other. Even though both samples have nearly equal dimensions, the difference in resistance in two samples may be due to crystal quality. Sample #1 had under gone several cooling process while sample #2 was intrinsic "virgin-cooled state". Our experience with organic molecular conductors showed that the thermal cycles can greatly affect the resistivity of the sample.

The resistance of both samples increases with an oscillations while increasing the angle $|\theta|$ with peak resistance about $\theta = \pm 75^{o}$. And, on further increase in $|\theta|$, the resistance shows the local minima at $\theta = \pm 90^{o}$. This feature observed local minima for $\theta = \pm 90^{o}$ will be discussed later in this chapter and some possible scenario in Chapter 5.

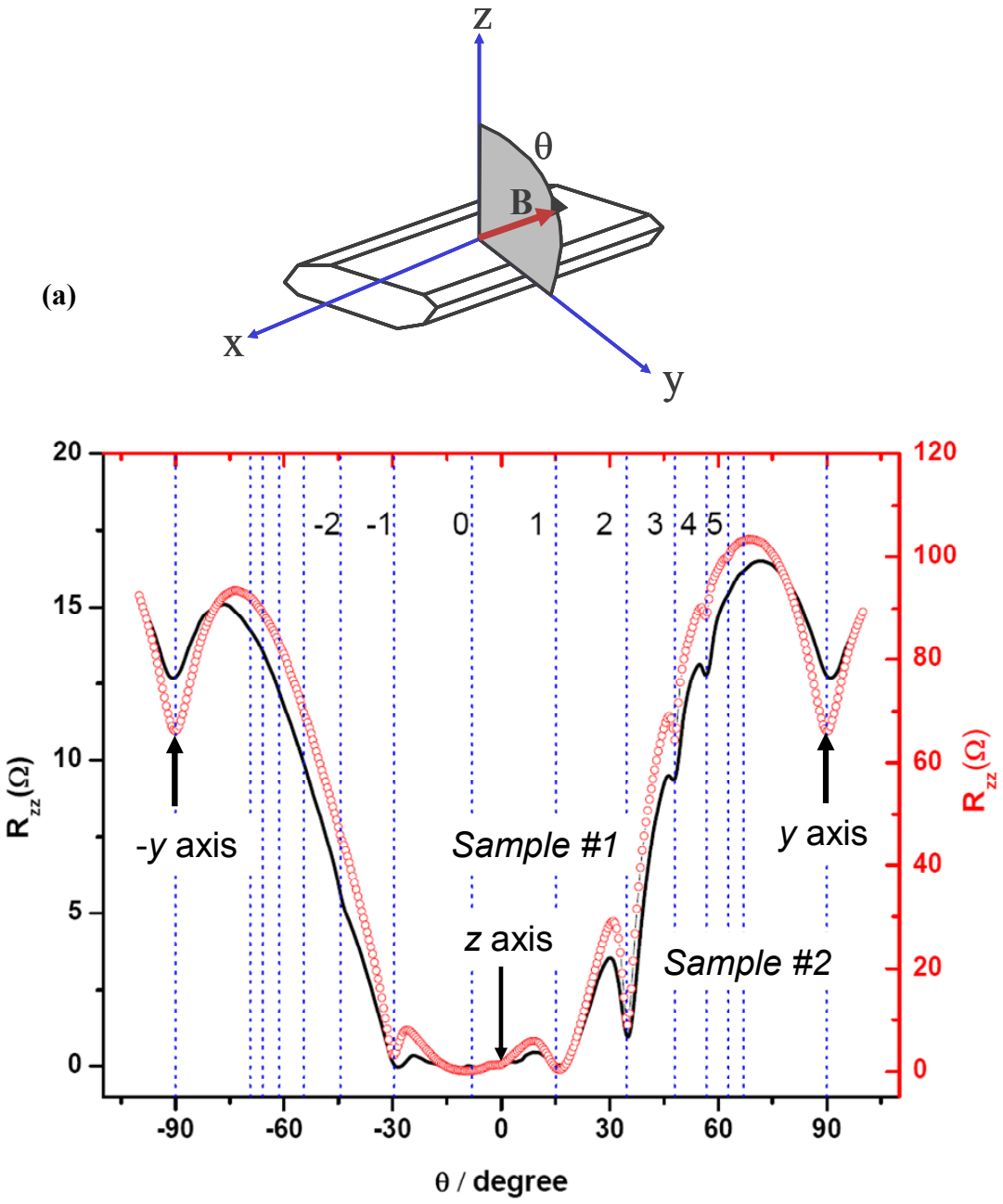

FIG. 4.7 (a) Sample orientation with respect to magnetic field in LMA scheme. (b) Measured interlayer resistance of two samples in 9T magnetic field rotated in the *y*-*z* plane (Lebed plane) at 100 mK. The open circles (sample #1) and solid line (sample #2) distinguish the samples. The dotted vertical lines are the calculated positions of Lebed resonances given by Eq. (4.1) with $\phi = 90^{o}$.

As presented in **Figs. 4.7**, the resistance shows pronounced oscillations when the magnetic field is rotated in *a*-*c* plane ($\phi = 90°$). The number of oscillations as well as their amplitudes are not symmetric about $\theta = 0^{o}$, and higher order oscillations observed when the field rotation plane moves away from *y*-*z* plane. A small nonsymmetric feature in magnetoresistance may arise from slight misalignment of sample during the measurement. Another possible reason may be due to the triclinic crystal structure with different magnitudes of the transfer integrals between the DMET molecules as shown in **Fig. 8**.

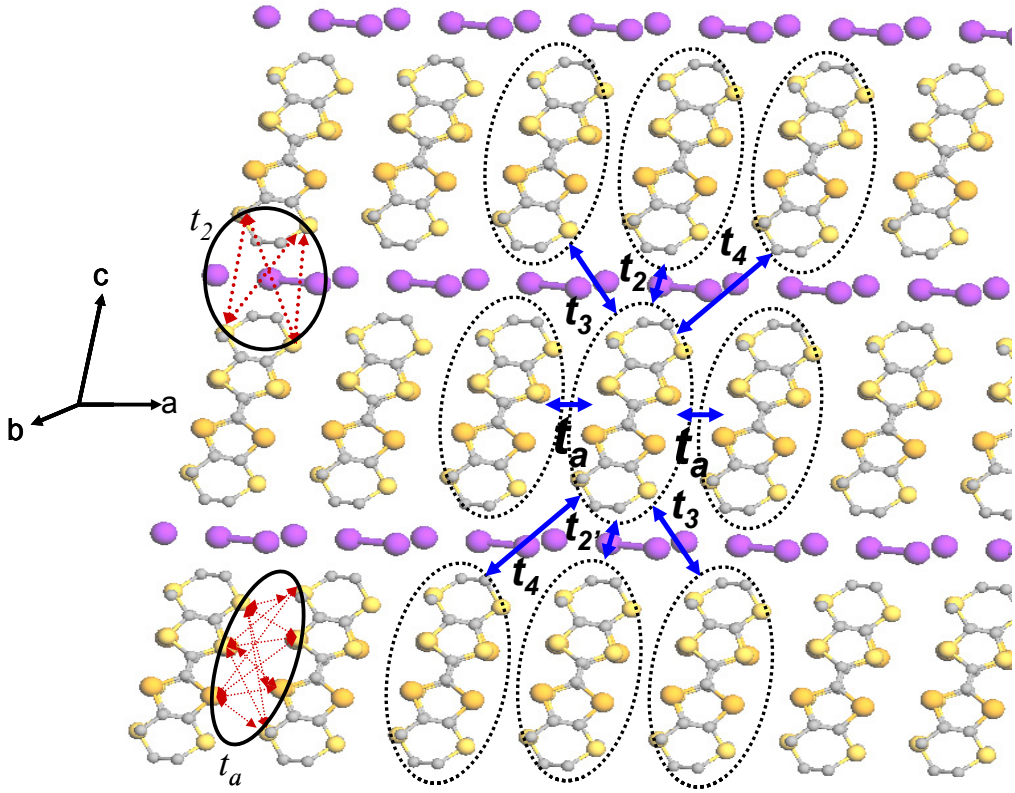

Fig. 4.8 The molecular arrangement of (DMET) and transfer integrals of $(DMET)_2I_3$ viewed along the most conducting axis (*b*) where the molecular plane is separated by inorganic I_3 molecules along the *c*-axis. The nearest neighbor interactions are t_2 and $t_{2'}$ and the second nearest neighbor interactions are t_3 and t_4. The transfer integrals may be responsible for nonsymmetric in the number and the amplitudes of magnetoresistance oscillations.

In this two dimensional (*a-c* plane) molecular packing each DMET molecule is surrounded by eight neighboring DMET molecules as shown in **Fig 8**, each having different interactions. It is expected that the nearest neighbor interactions t_a, t_2 and $t_{2'}$ are strongest, while second nearest neighbor t_3 and t_4 are weaker. The interactions $t_2 \sim t_{2'} = t_c$ and with $t_3 > t_4$, the magnetoresistance is expected to be different along the right and left from the vertical plane as $\sigma \sim t^2$. The number of oscillations and amplitudes is believed to be connected to the strength of these transfer integrals giving the nonsymmetric feature in numbers as well as the amplitudes of these oscillations. However, away from the *a-c* plane the effect is dominated due to the strongest transfer integral t_b and more symmetric oscillations are observed as shown in **Figs. 4.2-4.6**.

Similar nonsymmetrical features have been observed in the $(TMTSF)_2ClO_4$ [22] and $(DMET\text{-}SeF)_2I_3$ [23] in resistivity data as well as in $(DMET)_2I_3$ in periodic orbit resonance data [24]. Ishikawa [4.25] calculated the transfer integral for $(DMET)_2I_3$ in the *a-b* plane, however no report has been found for the transfer integral calculations in *a-c* plane However, the calculations of these transfer integrals are very complicated due to the presence of Se and S atoms. The DMET molecule is made of TMTSF and ET molecules. The TMTSF and ET ends have different thicknesses, due to the difference in the Van der Waals radii of the constituent atoms. To produce face-to-face stacks, successive molecules must be rotated 180˚ relative to one another which gives the very complex transfer integrals. In the current experiment, the ratio of the amplitudes of magnetoresistance oscillations in the vicinity of *a-c* plane (*y-z* plane in Cartesian coordinate system) is estimated to be ~ 10. Thus the nonsymmetrical feature in

amplitudes and number of oscillations may be due to the tricilinicity of crystals structure due to the anisotropic transfer integrals.

So far, it can be seen that these large resistance oscillations are a very peculiar feature of Q1D conductors. They are seen for virtually any possible θ or ϕ angular rotation of magnetic field. We can empirically define the positions of the minima observed in these resistance oscillations by the relation

$$\tan\theta \sin\phi = n\frac{b\sin\gamma}{c\sin\alpha\sin\beta^*} + \cot\beta^* \tag{4.1}$$

where n is an integer, and β^* is give by

$$\cos\beta^* = \frac{\cos\gamma\cos\alpha - \cos\beta}{\sin\alpha\sin\gamma} \tag{4.2}$$

Here, θ denotes, as usual, the angle that the magnetic field makes from the z-direction, and (α, β, γ) and *(a, b, c)* are the lattice angles and parameters, respectively. For $(DMET)_2I_3$, these lattice parameters were reported to be a = 6.669 Å, b = 7.761 Å, c = 15.776 Å, α = 89.96^o , β =81.81^o, and γ = 78.19^o [4.24]. Most of the resistance minima found in **Fig. 4.6** and **Fig. 4.7** can be indexed by the relation give by Eq. (4.1), with an exception for field rotations in the x-y and x-z planes.

All of the above experimental data shown in **Figs. 4.2 – 4.7** were taken for a magnetic field strength of 9T. It is worth exploring whether or how these features evolve with field strength (The evolution of field dependence of these features calculated based on available theoretical models is shown in **Fig. 2.15.** We have thus measured the resistance of sample #1 for three different field strengths 3T, 6T, and 9T, for field rotations in the y-z plane, as shown in **Fig. 4.9**. For 3T, only lower order oscillations (*i.e.,* n = –1, 0, 1) are clearly observed, though higher order oscillations are identified in

second derivatives of the raw data (shown in the inset of **Fig. 4.9**). For higher field, 9T, oscillations as high as $n = +5$ are observed. These oscillations for the field rotation in *y-z* plane are first predicted and observed experimentally in $(TMTSF)_2X$ (X = ClO_4 and PF_6). As discussed in Chapter 2, they are ascribed to the commensurate motion of electrons across the Fermi surface and are purely geometrical resonances which measure the lattice parameters rather than the band parameters [4.2, 4.3, 4.4].

As shown in **Fig. 4.9**, the overall nature of angular dependence of resistance is similar for different magnetic field strength *i.e.*, resistance increases with the increase in angle $|\theta|$ with several oscillations. Also, the amplitude of oscillations increases with the increase in magnetic field. One of the striking features observed from this plot is that the positions of minima observed in resistance are independent to the strength of applied magnetic field. We now plotted the field dependence of resistance (extracted from **Fig. 4.9**) for angular position $\theta = 8.6°$, 15.5°, 31°, and 90° as shown in **Fig 4.10**. The angle $\theta = 8.6°$ is the position at which the resistance has local maxima, between the two local minima indexed by $n = 0$ and 1. The angle $\theta = 15.5°$ is the position of minima $n = 1$. Again, the angle $\theta = 31°$ is the position at with the resistance has local maxima, between the two local minima indexed by $n = 1$ and 2. Finally, the angle $\theta = 90°$ is the position of sharp minima observed.

From **Fig. 4.10**, it is seen that the resistance of sample increases with field strength for angular position $\theta = 8.6°$, 31°, and 90°, however it tends to saturate for angular position $\theta = 15.5°$. In other words, the resistance of sample saturates at higher field at certain angular position. The saturation and non-saturation of this resistance was explained by dimensional crossover due to the interference effects between electron

velocity components along the *z*-axis and the electron motion along the *y*-direction [12]. The more results and explanation of this feature will be discussed later in this chapter (section 4.4). Interestingly, for the angular position $\theta = 90°$, at which the resistance shows sharp minima, the resistance does not show any saturating behavior.

When the magnetic field is applied parallel to the *y*-axis (*i.e.*, $\phi = 90°$), such as shown in **Fig. 4.7**, and electron motion is perpendicular to the magnetic field, due to current being applied along *z*, electrons experience the largest Lorentz force as depicted in **Fig 4.11**. As results, magnetoresistance is expected to be maximal. Experimentally, however, we observe a pronounced, if broad, local minimum. Strong *et al.* [4.13] and independently, McKenzie and Moses [4.15] suggested that the magnetic field parallel to the *y*-axis larger than a certain value de-emphasizes coherent motion (3D Fermi liquid) along *z*, and induces 2D non-Fermi liquid. This is basically Lebed's field induced dimensional crossover effect, but for the normal state (*i.e.*, non-superconducting state). A study on $(TMTSF)_2PF_6$ by Lee and Naughton [4.26] for field parallel to *y*, showed saturating of magnetoresistance at high field, however. Classically, the magnetoresistance is predicted to be non-saturating. Also, in $(TMTSF)_2X$, it is known that for *B//y*, the superconducting state is highly anomalous, with H_{c2} far exceeding the Pauli limit, potentially associated with spin triplet Cooper pairing [4.27,4.28]. In contrast, $H_{c2}(T)$ for $(DMET)_2I_3$, saturates at low temperature, without exceeding the Pauli limit, as will be discussed in Chapter 5. Further studies will be required to explore the relationship between the magnetoresistance minimum observed for field parallel to *y*-axis and superconducting state or any dimensionality enhancement.

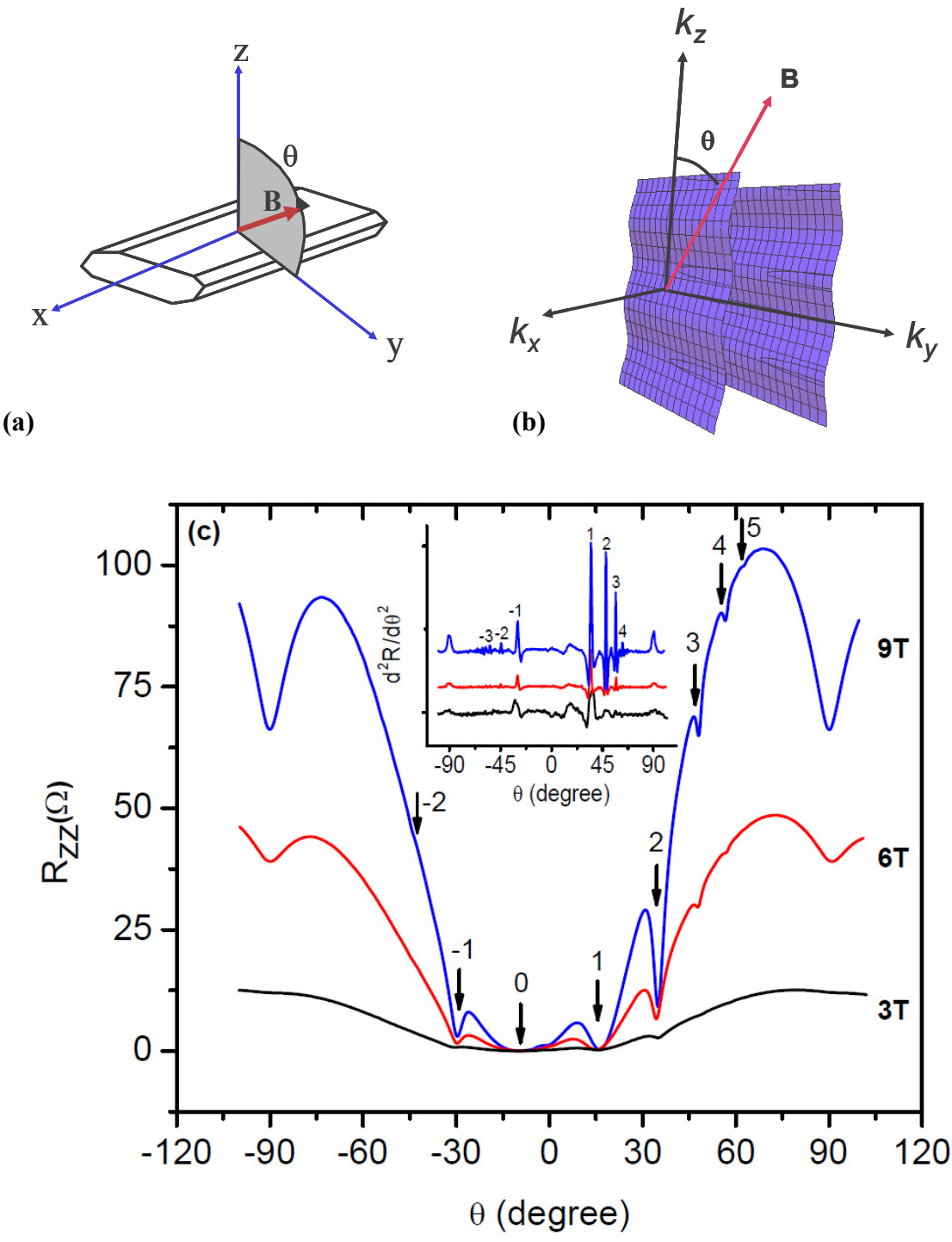

FIG. 4.9 The angular rotation of magnetic field (a) in real space, (b) in momentum space. (c) The observed interlayer resistance for the field rotation in the Lebed *y*-*z* plane for different magnetic field strengths. The arrows represents the position of Lebed minima given by Eq. (4.1) with $\phi = 90^{o}$. The inset shows the 2nd derivative of raw data showing the higher order of oscillations.

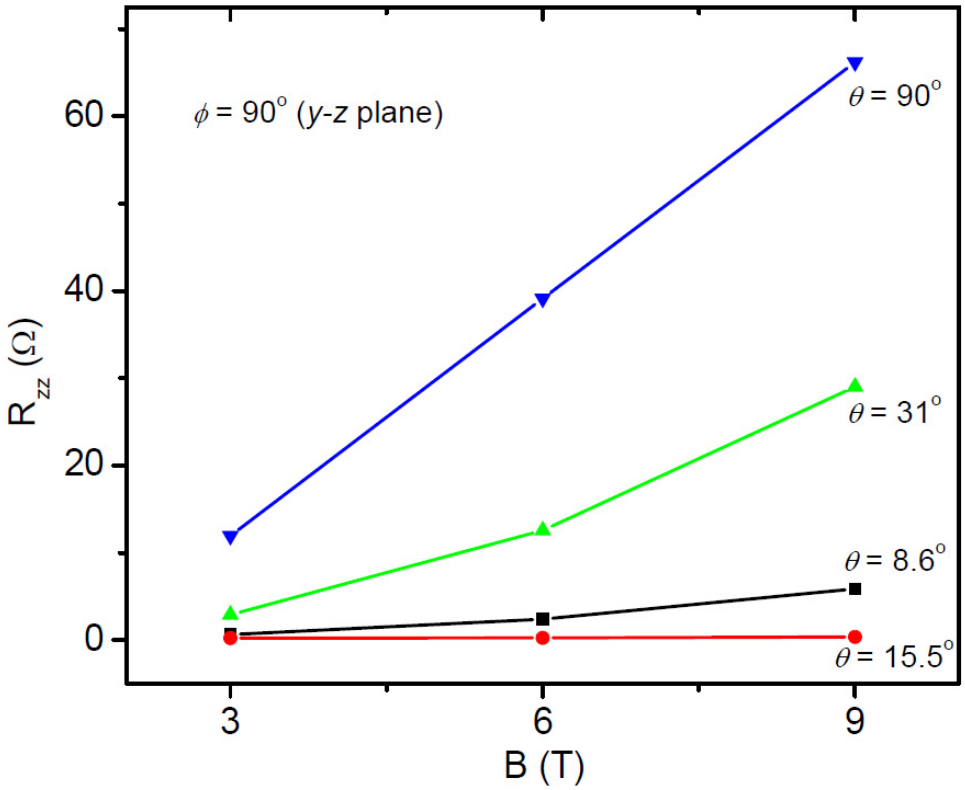

Fig. 4.10 The field dependence of resistance for angular position θ = 8.6°, 15.5°, 31°, and 90°. The data extracted from **Fig. 4.9**.

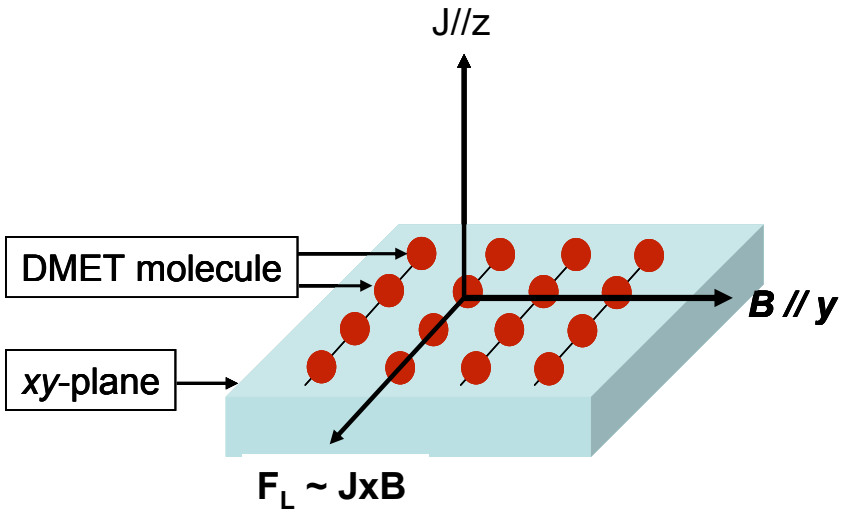

FIG. 4.11 The schematic diagram showing the motion of an electron along *z*-direction with magnetic field along *y*-axis. The electron experiences a maximum Lorentz force $F_L \sim JB$ and classically the magnetoresistance is expected to be the maximum.

As discussed earlier, upon closer examination of the experimental data, oscillations are observed for the field rotation in a plane with $\phi = 0^o$ and around $\theta = \pm 90^o$ (x-z plane). These are the DKC oscillations and are observed for the first time in $(DMET)_2I_3$. In **Fig. 4.12,** the curve $\phi = 0^o$ represents the true x-z plane, and the DKC oscillations set shifted for $\phi \neq 0^o$ by an interplay of these DKC oscillations and the Lebed oscillations, which is responsible for the asymmetry of the data. Similar shifts in oscillations have been observed in $(TMTSF)_2PF_6$ [4.31]. Classically, when the magnetic field is perpendicular to the current direction, the largest magnetoresistance is expected (*i.e.*, maximum Lorentz force). In this current field rotation scheme (x-z plane), the magnetoresistance is expected to be maximum when the magnetic field is parallel to the x-axis. A small local maximum in resistance is observed experimentally for field parallel to x-axis as shown in **Fig. 4.12**. However, this peak in resistance was explained in terms some close orbit when the magnetic field is parallel to x-axis [4.7]. When the field is directly parallel to x-axis, there is a small band of closed orbits near the extrema of the FS. The closed orbits are more effective averaging the velocity to zero than the extended orbits, resulting in an enhanced resistance. This peak can be used to estimate the strength of interlayer coupling t_c. The DKC oscillations can be used for determination of FS warping by calculating transfer integral t_y along k_y-direction: provided the interlayer distance c and the Fermi velocity v_F along the chain, by using the relation given by Eq. (2.12), which is given as

$$\Delta(\tan\theta) = \frac{\pi\hbar v_F}{2t_y c} \qquad (4.3).$$

In case of $(DMET)_2I_3$, the peak in resistance is observed around $\theta \approx \pm 15°$ and using c = 15.776 Å and $v_F = 2.7 \times 10^4$ ms^{-1} [4.23], the transfer integral is estimated to be

t_y = 53 meV. For $(TMTSF)_2ClO_4$ in the anion ordering state, the value was estimated to be t_y = 12 meV (24 meV in above anion ordering state) [4.7] and for $(TMTSF)_2PF_6$, it was estimated to t_y = 32 meV under a pressure of ≈ 10 kbar [4.35].

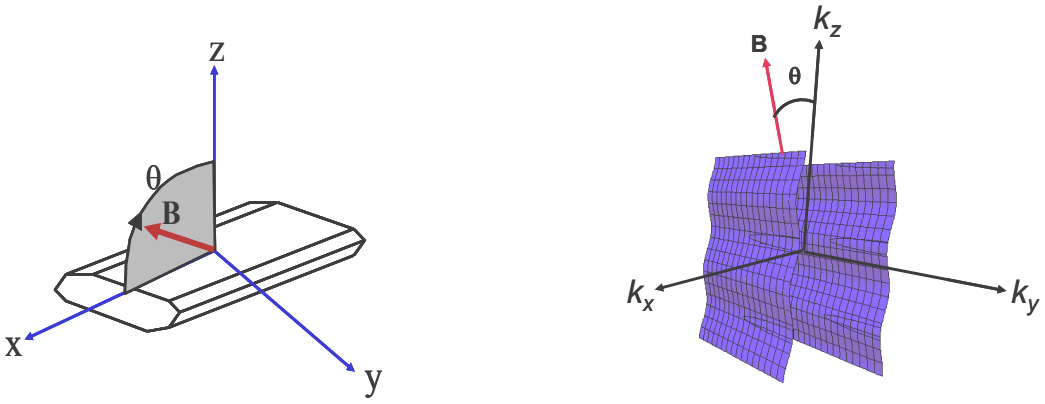

(a) **(b)**

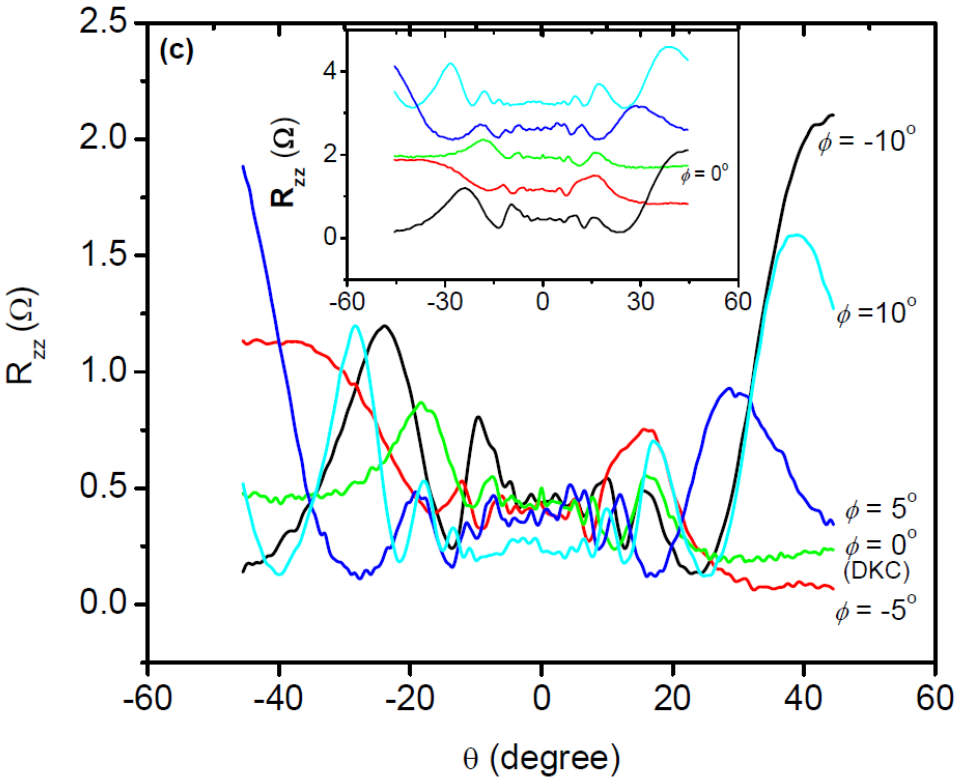

FIG. 4.12 The angular rotation of magnetic field (a) in real space, (b) in momentum space. (c) Measured interlayer resistance of $(DMET)_2I_3$ (Sample #1) for the field of 9T rotated in the *x*-*z* plane (DKC for $\phi = 0^o$). (Inset) the curve is offset vertically for clarity and the angle θ is measured from the x-axis.

The third kind of Q1D resistance oscillation (after the Lebed and DKC effects), known as the Yoshino angular effect (YAE) observed for a ϕ–rotation for $\theta = 90^{o}$ (x-y plane) as shown in **Fig. 4.13**. The YAE causes two resistance minimum ~ 15° either side of the x-z plane, when magnetic field rotating in the x-y plane. The positions of resistance minima are in agreement with the previously reported positions [4.8]. The angular separation between two minima is observed to be $\Delta\phi \approx 30°$, with an asymmetry in the positions of the minima observed due to the triclinic crystal structure.

As discussed in Chapter 2, the origin of the YAE is closely related to the corrugation of the Q1D Fermi surface within the x-y plane and YAE resistance minima can be used to estimate the ratio of transfer integrals t_x/y_y by using the following analytical expression [4.29]

$$\Delta\phi = 2\sqrt{2}\,\frac{b}{a}\,\frac{|t_y|}{|t_x|}\sin\gamma \qquad (4.4).$$

With lattice parameter of $b = 7.761$ Å and $a = 6.669$ Å, $\gamma = 78.19^{o}$ and observed angular width of $\Delta\phi \approx 30°$, the transfer integral ratio is estimated as $t_x/t_y \sim 9.0 \pm 0.9$. Since our experimental data are every $\phi = 5^{o}$, so the estimation of $\Delta\phi$ has an uncertainty, which is estimated as $\delta\phi = \pm 2.5°$. This yields transfer integral ratio as $t_x/t_y \sim 9.0 \pm 0.9$. A somewhat more accurate estimation of $\Delta\phi$ can be found in literature [4.38], which gives a value of $\Delta\phi = 28°$ with the estimated value of the transfer integral ratio $t_x/t_y = 9.7$. The anisotropy ratio estimated the conductivity measurement is $t_x/t_{y'} \approx \sigma_x/\sigma_{y'} = 10$ from [4.8]. However, in triclinic system $t_x/t_y \neq t_x/t_{y'}$. Thus the estimated value of t_x/t_y from the current measurement is in agreement with the previously reported ratio within the experimental error.

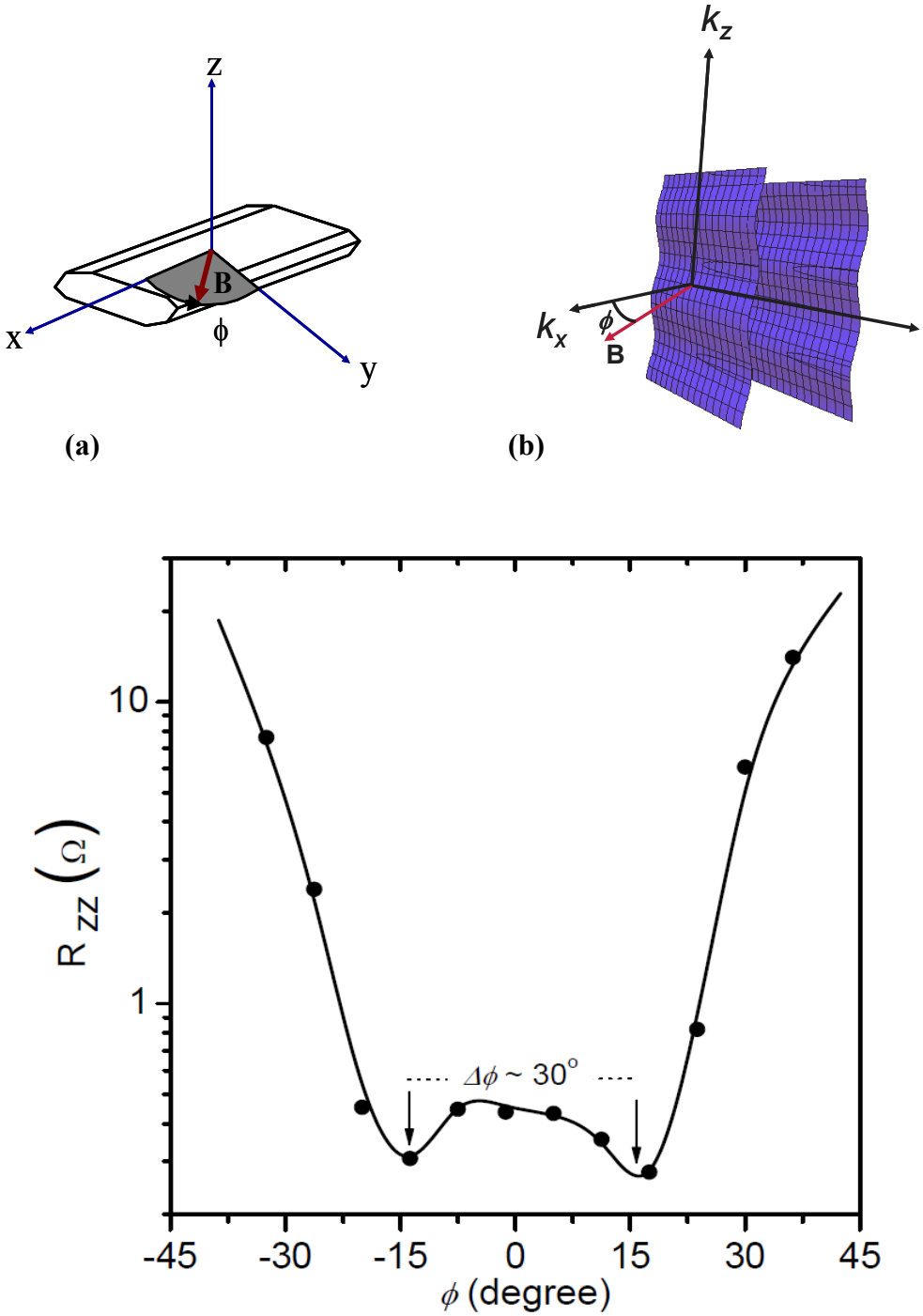

FIG. 4.13 The angular rotation of magnetic field (a) in real space, (b) in momentum space. (c) The observed interlayer resistance of $(DMET)_2I_3$ (Sample #1) for a field of 9T rotated in the *x*-*y* plane at 100mK: YAE oscillations. Local minima are observed for the angle $\phi \sim \pm 15^\circ$. The line is a guide to the eye.

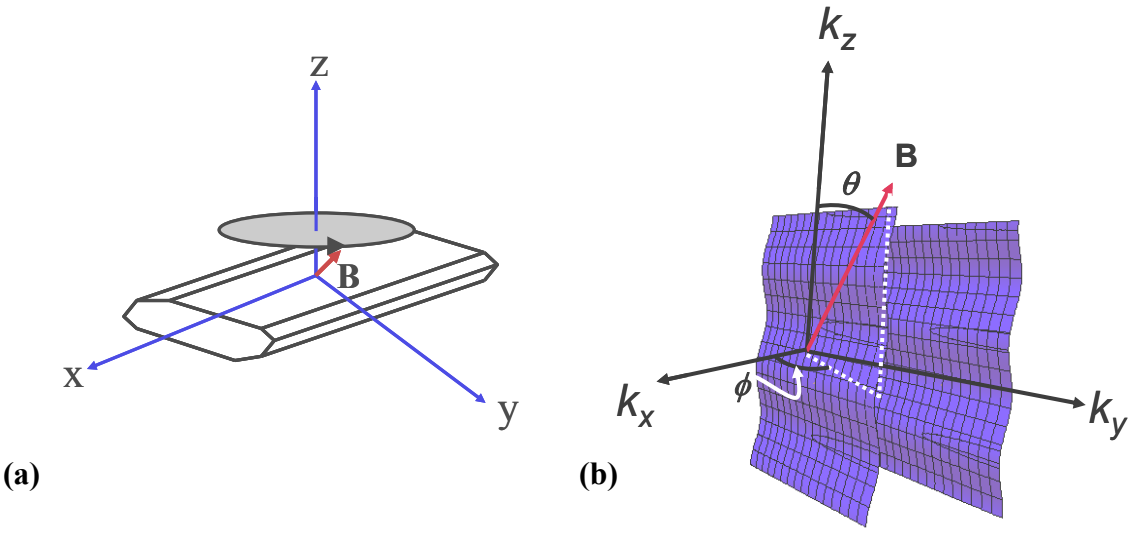

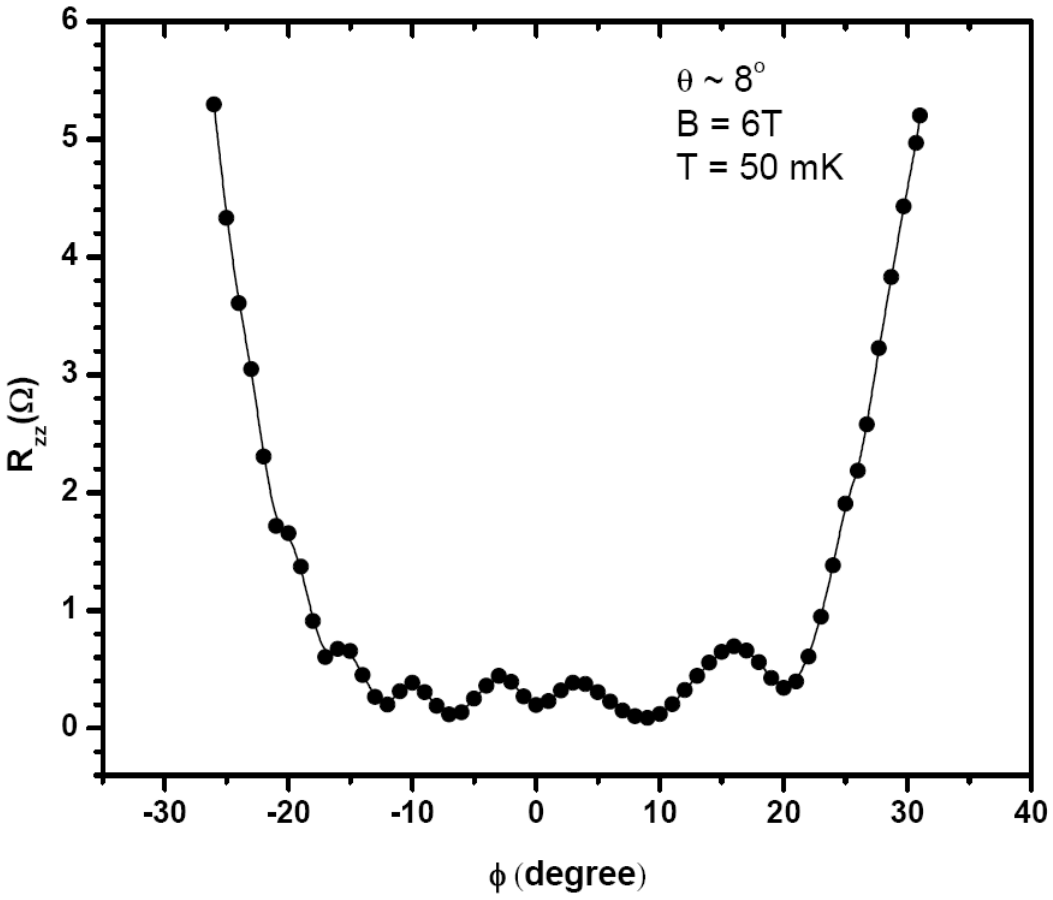

FIG. 4.14 The angular rotation of magnetic field (a) in real space, (b) in momentum space. (c) The observed interlayer resistance of $(DMET)_2I_3$ (Sample #1) for the field of 9T rotated arbitrary plane ($\theta \sim 8^o$ from *x*-*y* plane) at 100mK: LN oscillations.

Finally, more complex oscillations, the Lee-Naughton (LN) oscillations, are observed for the field rotating along arbitrary directions. The first experimental observation of LN oscillations occurred for $(TMTSF)_2PF_6$ while rotating angle ϕ for different fixed angles θ [4.11]. The oscillations in resistance in the LN scheme is shown in **Fig. 4.14**. Most of the oscillations in resistance shown in **Fig. 4.5** can be referred to LN oscillations, even though that measurement was taken varying θ while keeping ϕ constant. Since a field rotation in the $\phi = 90^o$ plane yields the Lebed effects, we believe that it is appropriate to name the oscillations seen in **Fig 4.5** as Lee-Naughton-Lebed (LNL) oscillations. In other words, either the LN oscillations are specialized to the Lebed effects for a particular rotation plane (*y*-*z* plane) or the Lebed oscillations are generalized to LN oscillations which cover all possible angular orientation of magnetic field rotation plane.

Thus, all previously reported AMRO effects are experimentally observed in the present single set of experiments. In the following sections, these experimentally-observed results are compared with new calculations based on the triclinic crystal structure, as well as with previously existing theoretical models.

There is a broad agreement between the angular positions of the LMA and LN (*i.e.*, LNL) oscillations, given theoretically by Eq. (4.1) and summarized experimentally in **Fig. 4.15**. Here, the integer *n*, which defines the positions of the minima is plotted as a function of $\tan\theta$ for in-plane ($\phi = 90^o$) and out-of-plane rotations for ϕ between 60^o and 120^o. A series of clear V-shaped symmetric patterns emerges, not about $\tan\theta = 0$ but about $\tan\theta = -0.15 \pm 0.05$. Moreover, these resistance minimum positions shift progressively away from this symmetry point as the rotation plane moves away from the

y-z plane (*i.e.* as ϕ deviates from 90°), as indicated by the curved lines (which can also be seen in **Fig 4.5** with the dotted line for the lowest order oscillations *i.e.*, for $n = \pm 1$). Meanwhile, owing to the tricilinicity of the crystal structure (Eq. 4.2), the curves in **Fig. 4.15** are symmetric about a calculated value of $\tan\theta = -\cot\beta^* = -0.146$. The measured value of $\tan\theta = -0.15$ is within experimentally uncertainty ± 0.05 of this calculated value. Interestingly, the number of minima observed for different ϕ angles, at least in the raw data, is not symmetric with respect to $\tan\theta$. Similar nonsymmetrical features have been observed in magneto-optical absorption spectrum measurements [4.25]. As discussed earlier, a certain asymmetry is expected due to the tricilinicity of the crystal structure; however, a contributing factor could be slight misalignment of the sample during the experiment.

These experimentally-measured resistance data can be summarized in the three dimensional plot shown in **Fig 4.16** and **Fig. 4.17**. This plot is generated for interlayer conductivity ($\sigma_{zz} \approx 1/\rho_{zz}$) with a logarithmic scale. In **Fig 4.16**, the horizontal and vertical lines correspond to the DKC and YAE effects, which are shown in **Fig 4.17**. The spikes emerge diagonally are LNL oscillations. The LN oscillations near the origin developed to the original Lebed oscillations along the circumference of the image. Similar three dimensional plots calculated using the theoretical model by Osada *et al.*, [4.22] was shown in **Fig 2.15**. In **Fig 2.15,** the spikes that are developed from the origin are discontinuous in circumference, showing the lack of Lebed oscillations in theoretical model.

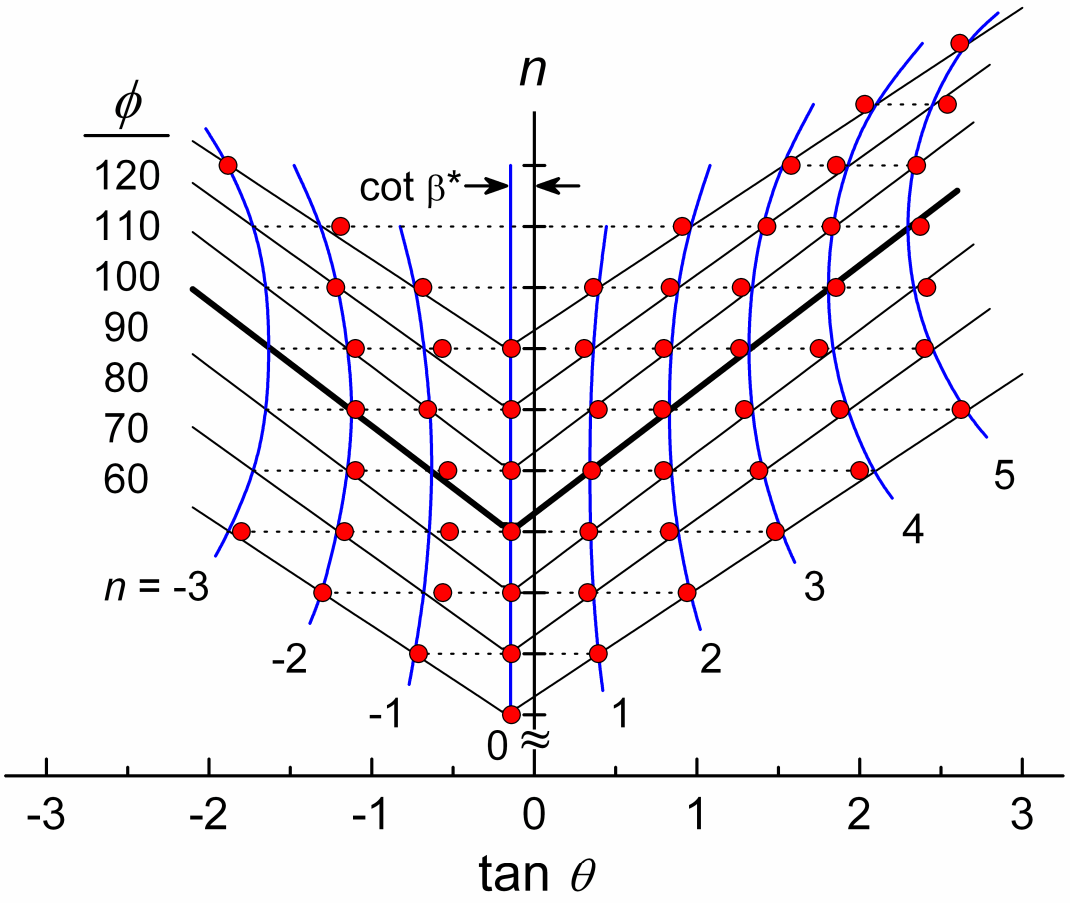

FIG. 4.15 Dependence of the resistance minima number *'n'* on *tan*θ, θ are the angles at which minima are observed for the field rotation in different planes (ϕ = 90° is *y*-*z* plane). The solid points are the angular θ position of minima observed in resistance for the field rotation in give plane (represented by angle ϕ). The solid straight and curved lines are calculated using Eq. (4.1). The experimentally observed data points lie at the intersection of two solid lines, showing the good agreement with theoretical predicted minima in experiment. The data are offset vertically for different ϕ for clarity.

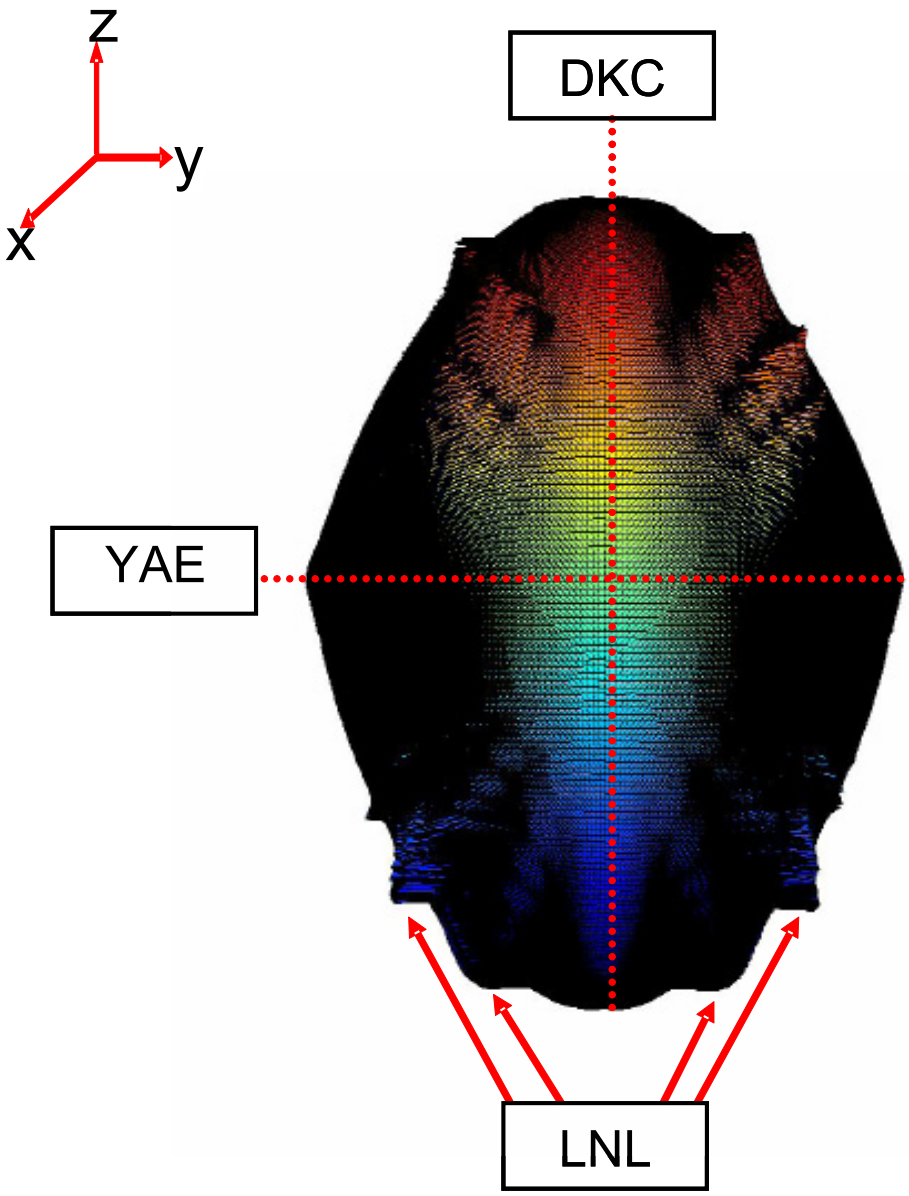

FIG. 4.16 Three dimensional presentation of the experimentally measured interlayer conductivity ($\sigma_{zz} \approx 1/\rho_{zz}$) of $(DMET)_2I_3$ in logarithmic scale in magnetic field of strength 9T at 100 mK. The horizontal and vertical lines correspond to the YAE and DKC effects, respectively (not all oscillations are visible due to the resolution of the image). Meanwhile, the spikes which emerge diagonally are LNL oscillations (the LN-oscillations near the origin developed to the original Lebed oscillations along the circumference of the image).

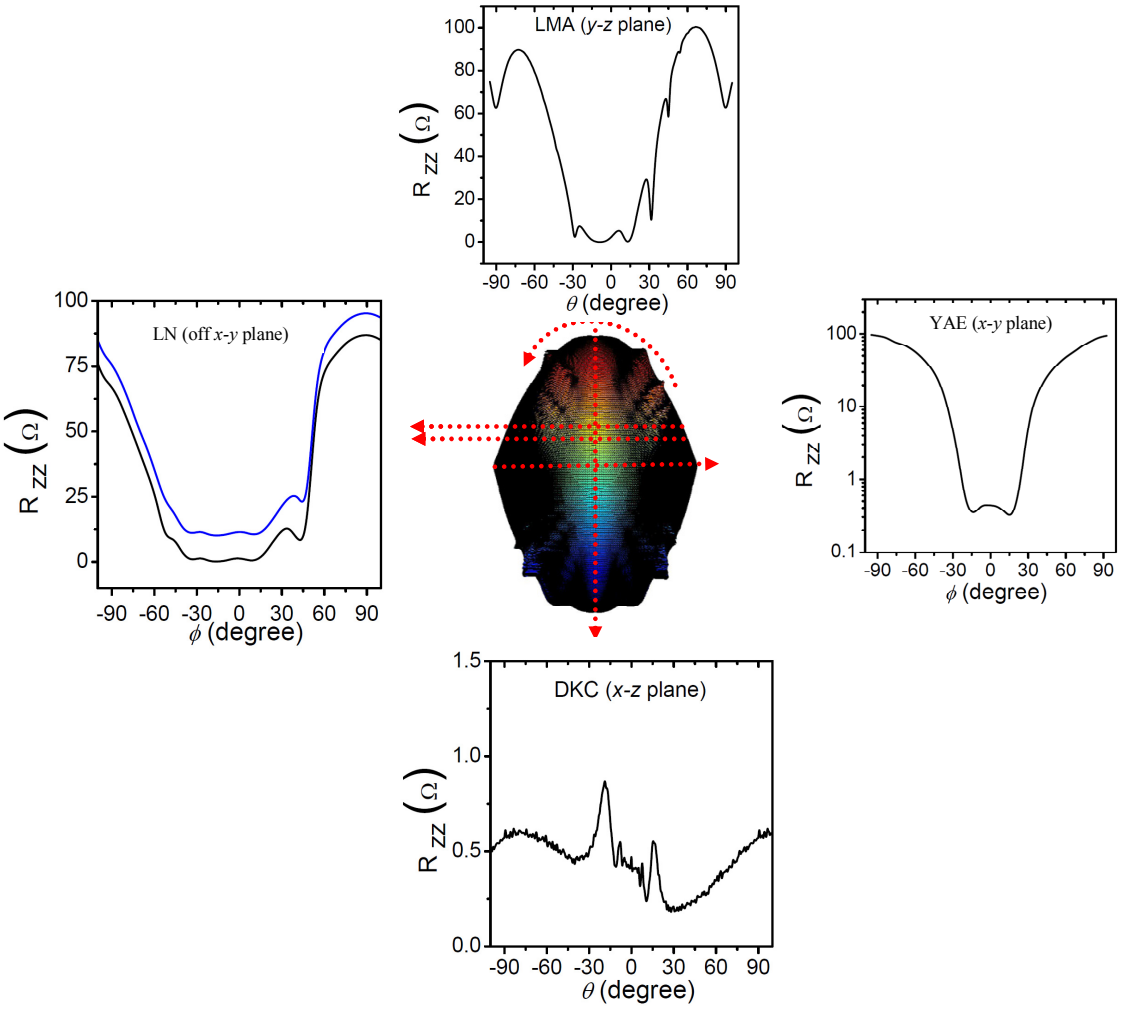

FIG. 4.17 Three dimensional presentation of the experimentally measured interlayer conductivity ($\sigma_{zz} \approx 1/\rho_{zz}$) of $(DMET)_2I_3$ in logarithmic scale in magnetic field of strength 9T at 100 mK, showing all four AMROs. The horizontal and vertical lines correspond to the YAE (pointing towards right), LN (pointing towards left) and DKC effects, respectively. Meanwhile, the spikes which emerge diagonally are LNL oscillations (the LN-oscillations near the origin developed to the original Lebed oscillations along the circumference of the image).

4.3 Triclinic Calculations

A number of theoretical models have been developed to explain AMRO in Q1D conductors, including some based on field-induced density-wave instabilities [4.2, 4.30, 4.31], electron-electron interactions [4.32, 4.33, 4.34], and non-Fermi liquid behavior [4.13, 4.35]. Analytical expressions for interlayer magnetoresistance calculated within each of these have employed an orthorhombic approximation to the Q1D crystals structure. However, these Q1D conductors are not orthorhombic, but triclinic in nature and it has proven very difficult to derive an exact analytical solution of magnetoconductivity using triclinic crystal symmetry. Here, we have succeeded to simulate the magnetoconductivity tensor derived from Boltzmann transport equation for this true triclinic crystal structure [4.36].

The Boltzmann transport equation is a semi-classical approach to calculate the carrier transport in crystalline metals. The expression for the magnetoconductivity tensor σ_{ij}, under the relaxation time approximation [4.37] is given by

$$\sigma_{ij} = \frac{2e^2}{V}\sum_k \left(-\frac{df}{dE}\right) v_i(k,0)\int_{-\infty}^{0} v_j(k,t)e^{t/\tau}dt, \tag{4.3}$$

where e = electronic charge, V = sample volume, f = Fermi distribution function, E = electron energy, v_i = ith component of the carrier velocity, k = electron wave vector, t = time, and τ = relaxation time, respectively, with τ assumed to be constant. The carrier velocity can be calculated based on tight binding energy dispersion,

$$E = -2t_a cosk_a a - 2t_b cosk_b b - 2t_c cosk_c c \tag{4.4}$$

where a, b and c, are lattice parameters and t_a, t_b and t_c are intermolecular transfer integrals along $\boldsymbol{a}$, $\boldsymbol{b}$ and $\boldsymbol{c}$, respectively. We have solved the Eq. (4.3) numerically in the presence of a magnetic field using the software developed by Prof. H. Yoshino at Osaka

City University in Japan. We calculate the interlayer magnetoresistance using t_a:t_b:t_c = 300:30:1 [4.38] and τ = 10^{-14} sec. It is found that this value of τ gives clear AMRO structures with the magnitude of B that we can easily achieve in the laboratory. The velocities v_a, v_b, and v_c along triclinic crystal axes are calculated as $v_i = \frac{1}{\hbar}\left(\frac{\partial E}{\partial k_i}\right)_{E=E_F}$ and transformed into that along the x, y and z-axes of the Cartesian co-ordinate system, by using matrix transformations (Q) in real space given by [4.34]

$$Q = \begin{pmatrix} \frac{a\sqrt{1-\cos^2\alpha-\cos^2\beta-\cos^2\gamma+2\cos\alpha\cos\beta\cos\gamma}}{\sin\alpha} & 0 & 0 \\ \frac{a(\cos\gamma-\cos\alpha\cos\beta)}{\sin\alpha} & b\sin\alpha & 0 \\ a\cos\beta & b\cos\alpha & c \end{pmatrix}$$

Once the Lorentz forces and wave vectors are calculated along the Cartesian coordinate system, they are converted to the triclinic system by using an inverse matrix transformation $\tilde{Q}$ given by

$$\tilde{Q} = \begin{pmatrix} a & b\cos\lambda & c\cos\gamma \\ 0 & b\sin\gamma & \frac{a(\cos\alpha-\cos\beta\cos\gamma)}{\sin\gamma} \\ 0 & 0 & \frac{c\sqrt{1-\cos^2\alpha-\cos^2\beta-\cos^2\gamma+2\cos\alpha\cos\beta\cos\gamma}}{\sin\gamma} \end{pmatrix}$$

This calculates a new Fermi velocity from the dispersion relation. To acquire computational simulation results with sufficient precision, the first Brillouin zone is divided into a grid of 128 x 128 x 128 sites. As for the time integration, it is assumed that the time step of Δt=10^{-16} sec is sufficient (*i.e.*, τ/100) to obtain accurate results with relaxation time τ = 10^{-14} sec. However, for very high magnetic fields (B > 30T), a much

finer Δt must be taken (*i.e.*, $\Delta t \sim \tau/1000$), since the Lorentz force and the change in wave vector k of a carrier in Δt become too large to draw precise trajectories of carriers. The zz-component of magnetoresistivity tensor ρ, ρ_{zz} is calculated as,

$$\rho_{zz} = \frac{\sigma_{xx}\sigma_{yy} - \sigma_{xy}\sigma_{yx}}{\sigma_{xx}(\sigma_{xx}\sigma_{yy} - \sigma_{xy}\sigma_{yx}) - \sigma_{xz}\sigma_{yy}\sigma_{zx} + \sigma_{xy}\sigma_{yz}\sigma_{zx} + \sigma_{xz}\sigma_{yx}\sigma_{zy} - \sigma_{xx}\sigma_{yz}\sigma_{zy}} \qquad (4.4).$$

The ρ_{zz} is reduced to $1/\sigma_{zz}$, since the second to last terms in the denominator at the right hand side of Eq. (4.4) are much smaller than ($\sigma_{xx}\sigma_{yy}$ - $\sigma_{yx}\sigma_{yx}$) for $(DMET)_2I_3$. The calculated ρ_{zz} as a function of angle θ at different angles ϕ is shown in **Fig 4.18**. Again the comparison of the experimental and calculated data is shown in **Fig. 4.19**. We have plotted the true magnetoresistance ($\Delta\rho/\rho$) as a function of θ angle for various ϕ angles. Here, it can be seen that the calculated magnetoresistance is qualitatively and semi-quantitatively in accordance with the experimental data, reproducing all known AMRO effects. The minima in magnetoresistance observed are well defined by Eq. (4.1), which also indicates the validity of our calculations. As we have seen in experimental data, the amplitudes of the oscillations decrease when the magnetic field rotation planes approaches towards the y-z plane. The detail comparisons of this amplitude of oscillations will be presented later in this chapter. Even though, we have calculated the magnetoresistivity, in **Fig. 4.18**, the data are plotted resistance versus the angle θ in such a way as to allow for a direct comparison of calculated data with experiment. It turns out that, the calculated resistance is about three times higher then the experimentally measured resistance. This may reflect the choice of relaxation time τ and (or) uncertainty in sample dimensions.

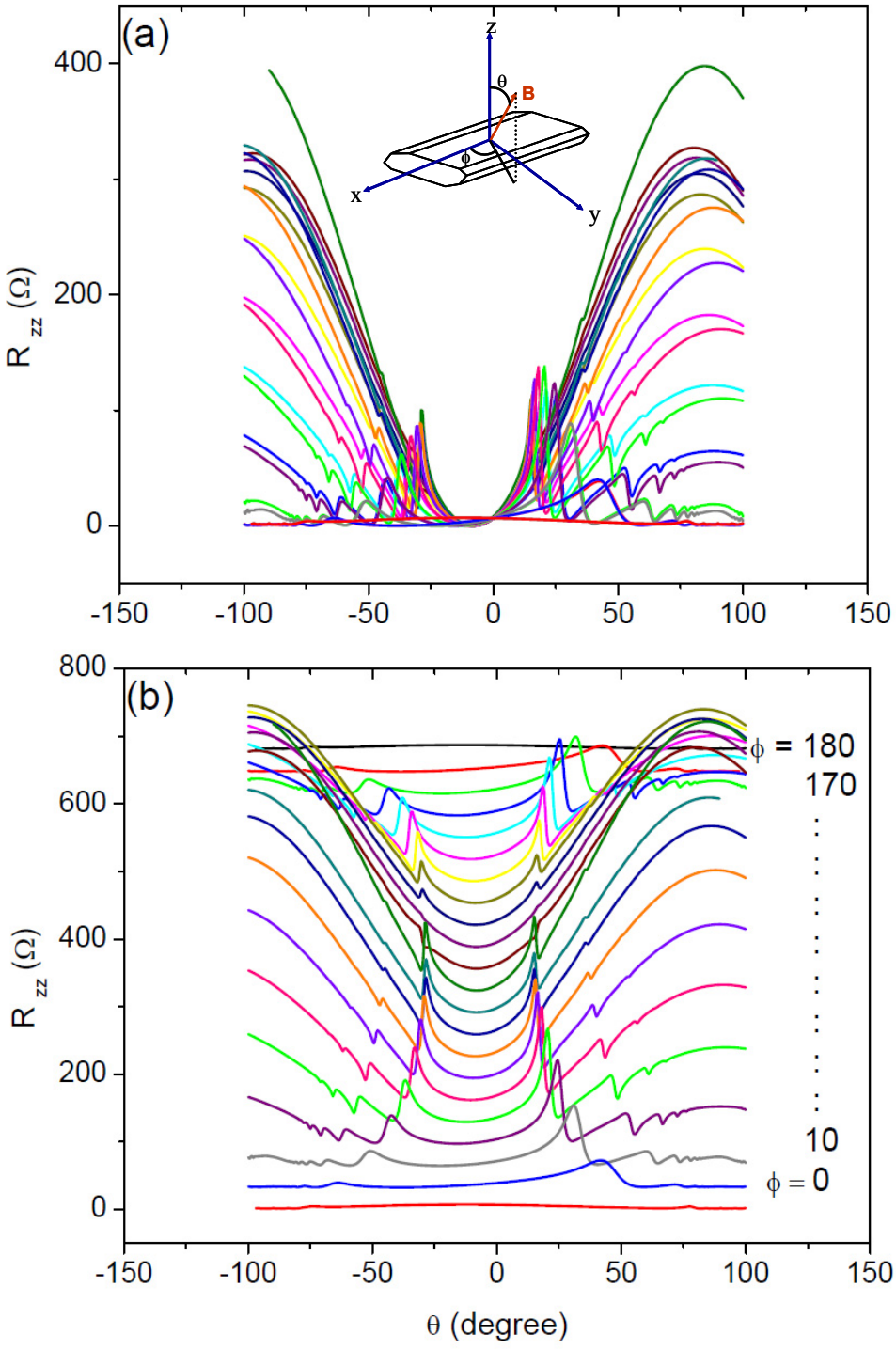

FIG. 4.18 The calculated interlayer magnetoresistance at different θ and ϕ angle at B = 9T using t_a:t_b:t_c = 300:30:1 and $\tau = 10^{-14}$ sec with lattice parameter for $(DMET)_2I_3$ given in above text. The curves are offset vertically for clarity (lower). The magnetoresistance has oscillations for the field rotation in every rotation plane.

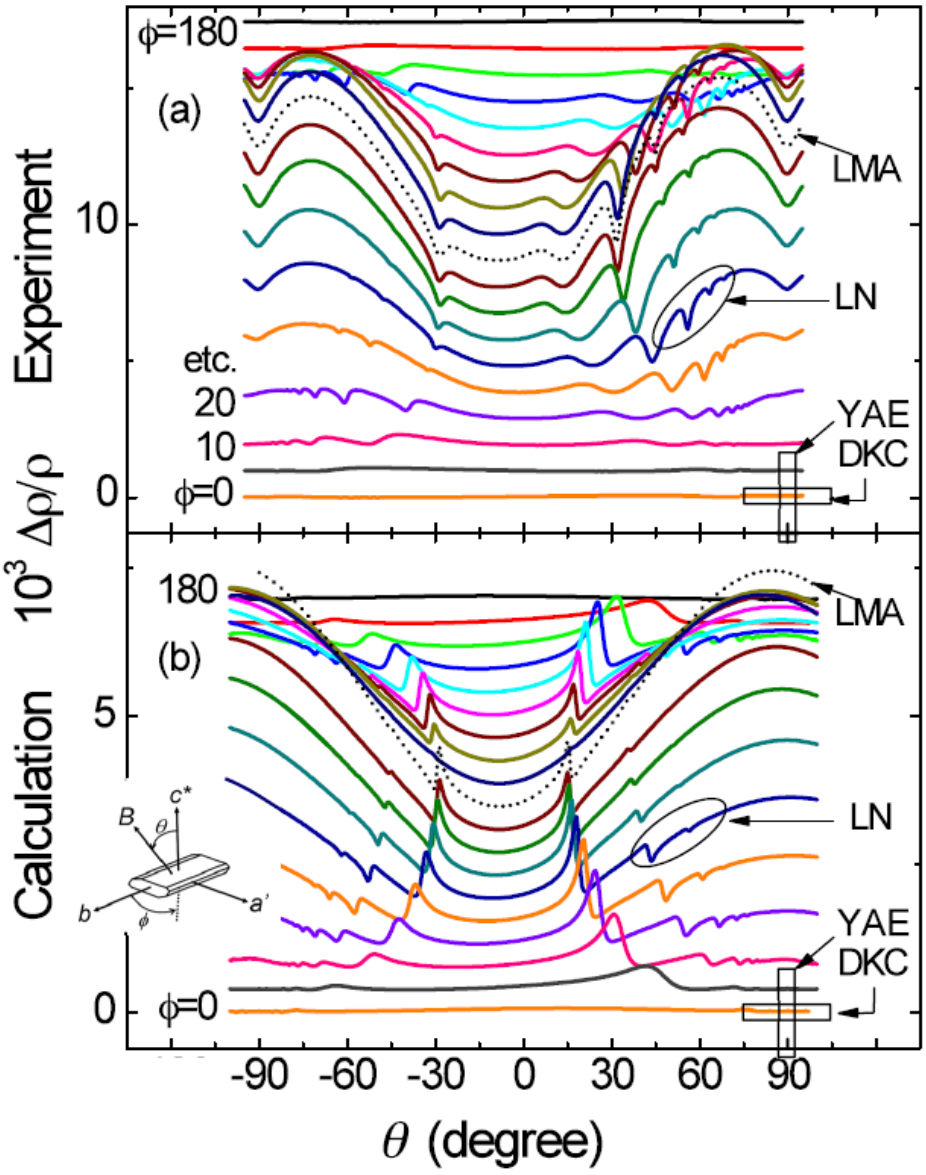

Fig. 4.19 (a) Interlayer magnetoresistance of $(DMET)_2I_3$ versus polar angle θ for different azimuthal angles ϕ at B = 9T and T = 100mK. (b) Calculated magnetoresistance at 9T using the true triclinic crystal structure. All known types of AMRO oscillations, LMA (dotted line at $\phi = 90^\circ$), DKC, YAE and LN, as indicated, are detected in the experiment and reproduced in the calculations (DKC and YAE are clearly evident on expanded scales). The DKC effect had not been previously observed in this compound.

We have calculated the τ dependence of magnetoresistance for the magnetic field rotating in *y*-*z* plane (*i.e.*, $\phi = 90°$) using the above equations and sample parameters. The resulting plot for three values of τ is shown in **Fig. 4.20**. The overall magnetoresistance of sample increases with the increase in τ. However, the sharp oscillation in magnetoresistance as observed for higher τ value.

Finally, some of the discrepancy can be attributed to uncertainties in the sample dimensions. We estimated these to be $\delta x = \delta y = \delta z \approx 20$ μm, which yields the resistivity uncertainty of $\delta\rho/\rho \sim 12.64$ %. Another affecting factor could be the current density to the sample. Nonetheless, calculated magnetoresistance is qualitatively in accordance with the experimental data.

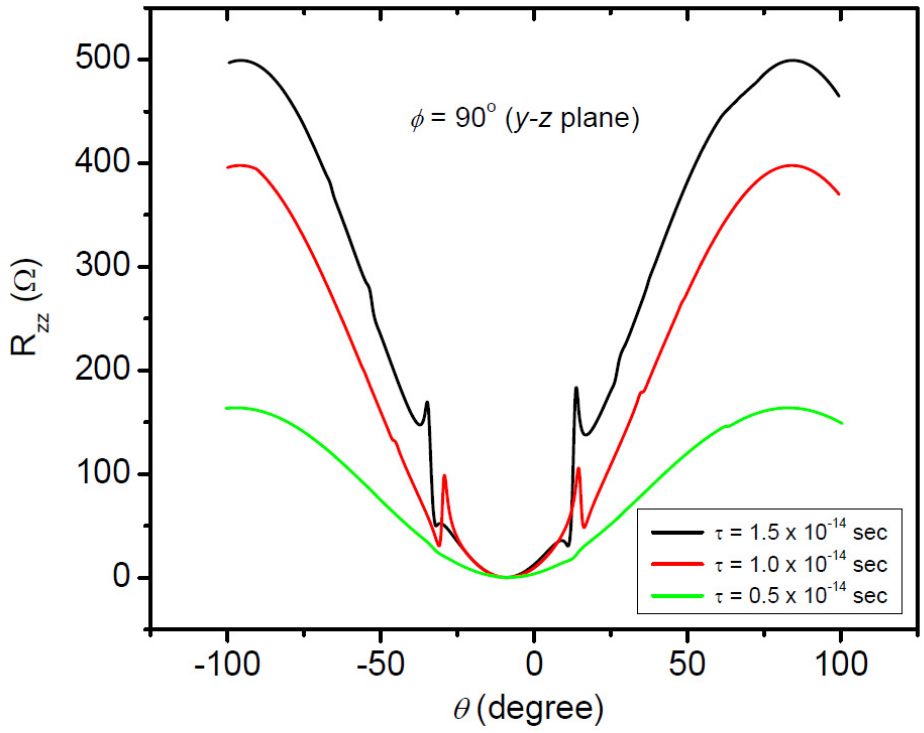

Fig. 4.20 The calculated interlayer magnetoresistance at different relaxation time as a function of angle θ for $\phi = 90°$ at 9T using t_a:t_b:t_c = 300:30:1. The resistance of the sample increases with the decrease in τ.

4.4 Comparison of Experimental Data with Calculations

It is clear that the present calculations are qualitatively in agreement with experimentally-observed magnetoresistance oscillations. As discussed earlier, some theoretical models [4.14 - 4.18] derive analytical expressions for the interlayer magnetoresistance oscillations using different approximations. These expressions are able to predict the positions of minima in magnetoresistance, given by Eq. (4.1). However, they fail to reproduce the experimentally observed magnetoresistance oscillations; the first predicted and observed AMRO in Q1D systems. The causes of absence of these features in magnetoresistance can be few. The first possible explanation could be that these expressions are derived assuming the orthorhombic crystal structure. It may be that Lebed oscillations (*y*-*z* plane) may be characteristic features of triclinic Q1D systems only. However, no experimental evidence exists for the absence of Lebed oscillations in orthorhombic Q1D materials, for the simple reason that no data are available. The second possible scenario could be that all of the above analytical models are ill-defined, meaning one can't derive the equation using single electron model.

Here, we have calculated the interlayer magnetoresistance in $(DMET)_2I_3$ for field rotated in the *y*-*z* plane using the expression given in Ref. [4.14] *i.e.*, Eq (2.14) (for simplicity) and compared this with the experiment as well as present triclinic calculation. The comparison is shown in **Fig 4.21**. **Fig. 4.21(a)** uses orthorhombic crystal symmetry (Eq. 2.14), while **Fig. 4.21 (b)** uses the present triclinic symmetry Boltzmann model. These can be compared to our experimental data in **Fig. 4.21(c)**. The positions of Lebed minima calculated from Eq. 4.1, using the triclinic lattice parameters for $(DMET)_2I_3$, are in good agreement with the experimental results of **Fig. 4.21(c)**. As shown in **Fig. 4.21**,

the magnetoresistance is as high as several thousand in both experiment and calculations. Indices as high as $n = \pm 6$ are observed both experiment and the present triclinic calculations but are absent in calculation using the analytical expression for magnetoconductivity. Derivatives $\partial^2\rho/\partial\theta^2$ illustrate this latter point, as well as the complete absence of LMA in the Kubo model calculations [4.14]

We have also calculated the magnetoresistance using the Boltzmann transport equation with the orthorhombic approximation (*i.e.*, $\alpha = \beta = \gamma = 90°$) for the field rotated in the *y*-*z* plane. The result is shown in **Fig 4.21 (a)** along with the calculations using analytical expression**.** Curiously, the oscillation in resistance has been observed and minima in resistance can be well indexed by the relation $tan\theta = n(b/c)$ (symmetric resistance minima due to the orthorhombic approximation of crystal structure). However, the amplitude of oscillations observed in orthorhombic approximation is about 10 times smaller then the oscillations observed using true triclinic crystal symmetry. Now, it is very important to look for experimental resistance oscillations in orthorhombic Q1D before drawing any conclusion, whether AMRO are special in triclinic Q1D systems.

As in other theoretical models, the present calculation is unable to reproduce the experimentally observed resistance dips for field parallel to the *y*-axis. In the present calculations, the resistance does not show local minima for field parallel to the *y*-axis. As discussed earlier, at this orientation the electron experiences the maximum Lorentz force and hence the maximum resistance is expected. However, employing the triclinic crystal symmetry, the resistance is found to be maximal at about ~8.5° away from the *x*-*y* plane.

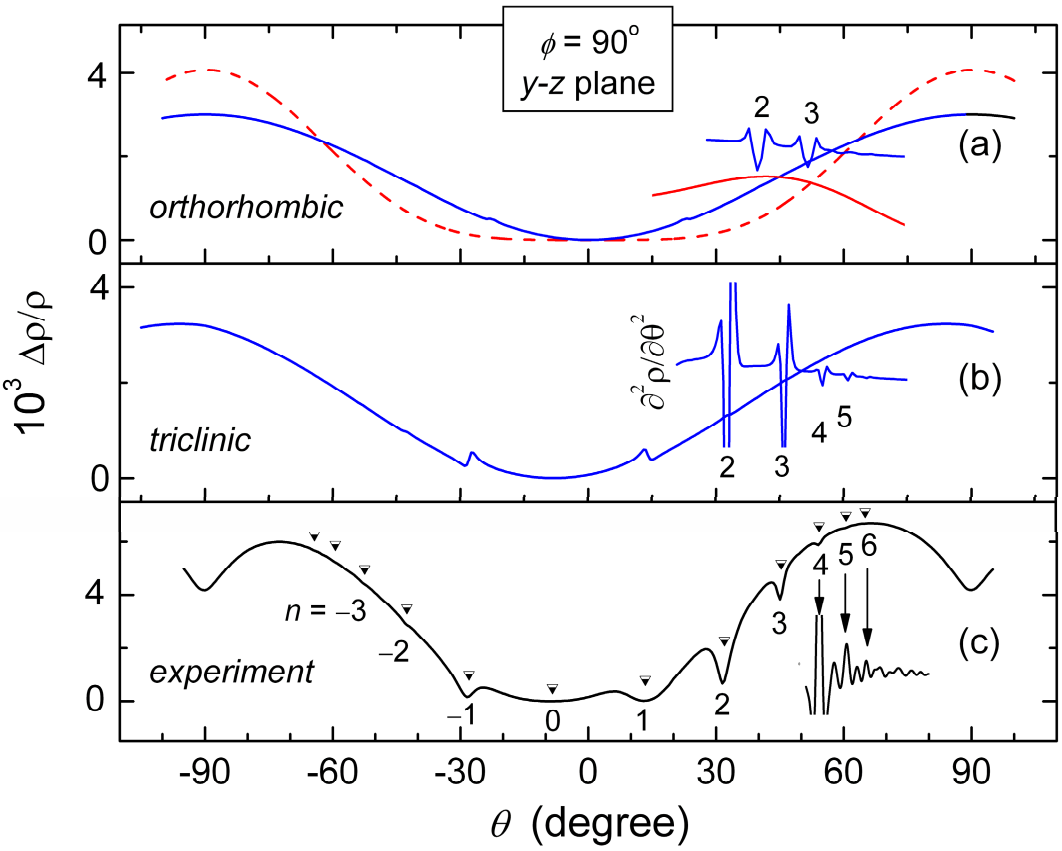

FIG. 4.21 Polar angle dependence (*i.e.* magnetic field rotated in *y-z* plane) of the 9T magnetoresistance of $(DMET)_2I_3$. (a) Orthorhombic Boltzmann numerical (blue) and Kubo analytic (red) calculations [4.14], (b) Present triclinic Boltzmann numerical calculation, and (c) Experiment. Insets show $d^2\rho/d\theta^2$ for the calculations, indicating the lack of Lebed oscillations using the Kubo formula, and their presence in Boltzmann calculations, with triclinic symmetry yielding features ~10 times larger than orthorhombic. Oscillations up to $n = 5$ or higher are observed in triclinic calculations (b) and experiment (c). Triangles indicate angular positions of the resistivity minima for indices n according to Eq. (4.1).

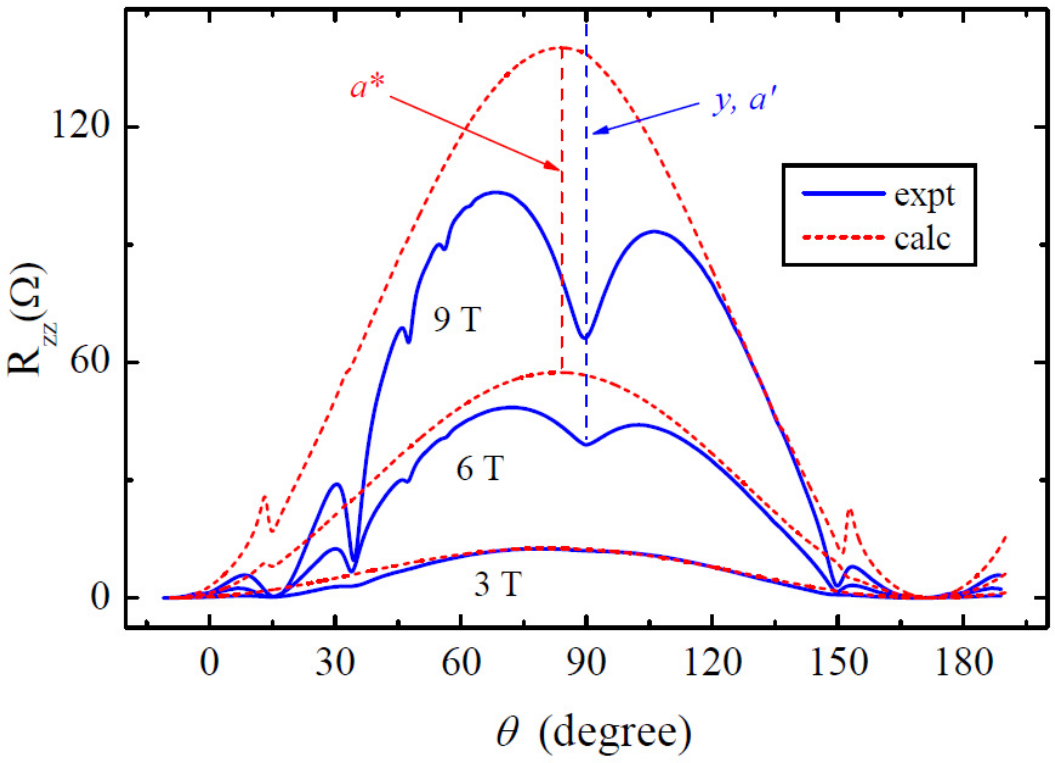

FIG. 4.22 Measured at 100 mK (solid lines) and calculated using triclinic Boltzmann transport equation (dashed lines) angle-dependent magnetoresistance of $(DMET)_2I_3$ at 3, 6 and 9 T, rotated in the *y*-*z* plane ($\phi = 90°$).

The magnetic field dependence of magnetoresistance for field strength of 3, 6, and 9T is calculated and compared with the experimentally observed magnetoresistance as shown in **Fig 4.22**. The calculation qualitative reproduces the experimentally observed magnetoresistance, except for the field in the vicinity of *y (a')*-axis. Note that the calculations in **Fig. 4.22** yield a maximum for field not along *y*//a', the normal to the planes at $\theta = 90°$, but at $\theta \sim 81.5°$, corresponding to reciprocal lattice a^* direction. This suggests that the internal current flows along the intermolecular *c*-axis, as opposed to the c*//*z*-axis. This is in fact borne out by experiment: the 3 T experiment curve in **Fig. 4.22**

also exhibits a maximum at $\theta \sim 81.5°$, as seen in **Fig. 4.23**. In the absence of this experimentally-observed minimum for $\theta = 90°$, the magnetoresistance shows the peak ~81.5°, at which the magnetic field is perpendicular to the *b*-*c* lattice plane. Classically, in this orientation of magnetic field, the current is perpendicular to the magnetic field and the electron motion experiences the largest Lorentz force and maximum magnetoresistance is expected and detected.

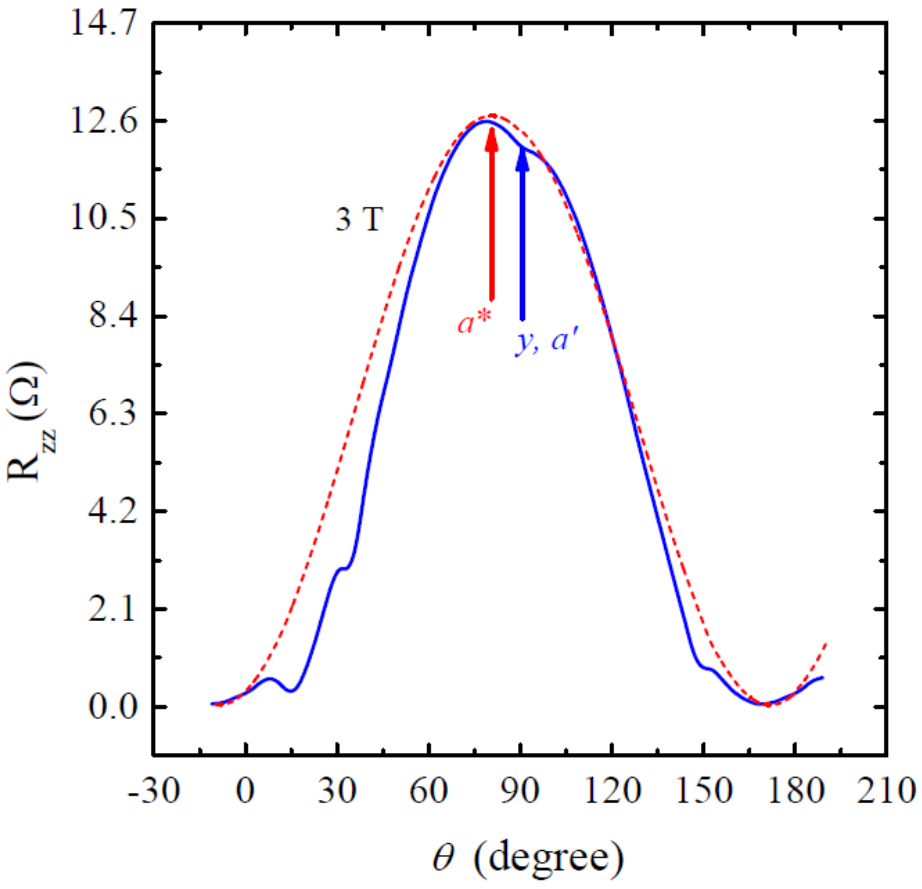

FIG. 4.23 Measured at 100 mK (solid lines) and calculated using triclinic Boltzmann transport equation (dashed lines) angle-dependent magnetoresistance of $(DMET)_2I_3$ at 3T, rotated in the *y*-*z* plane ($\phi = 90°$).

We can also compare present triclinic calculation with the experimentally observed DKC oscillations as shown in **Fig. 4.24**. The calculations are qualitatively in agreement with the observed data. Two symmetric peaks are observed about $|\theta| \approx 15^{o}$, characterizing the DKC effect, which measures the ratio of transfer integrals t_x/t_y. Furthermore, a local maxima in resistance for $\theta = 0°$ is observed in both calculations and experimentally.

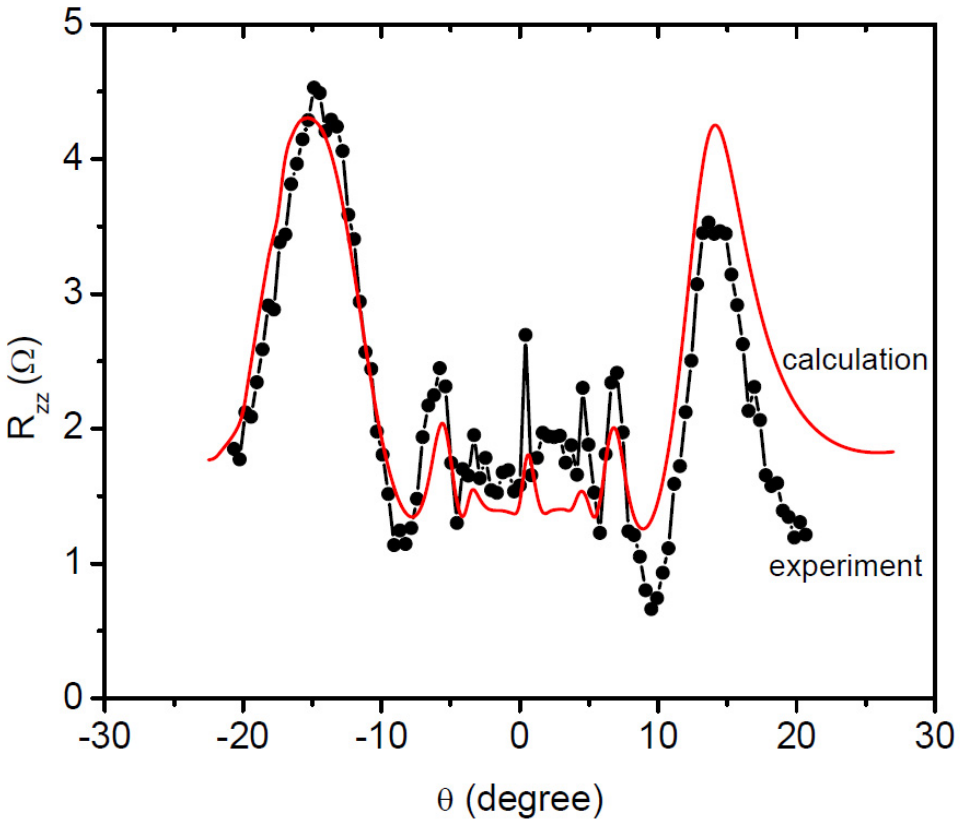

FIG. 4.24 Comparison of calculated magnetoresistance of $(DMET)_2I_3$ for magnetic field rotated in the *x*-*z* plane (DKC oscillations) with experiment data. The solid line is for calculated data and scatter points are our experiment. Experiment and calculation are qualitatively in agreement, with the peak in resistance at about $\theta \approx \pm 15°$. The angle θ is measured from the *x*-axis.

A comparison of YAE in the present calculations, with experimental data, is shown in **Fig. 4.25**. The experiment and calculations are qualitatively in agreement. Since the experimental data are taken every 5^{o}, it is not a particularly clear fit to the experimental data; however, the minima in magnetoresistance are close in both the experiment and the calculation.

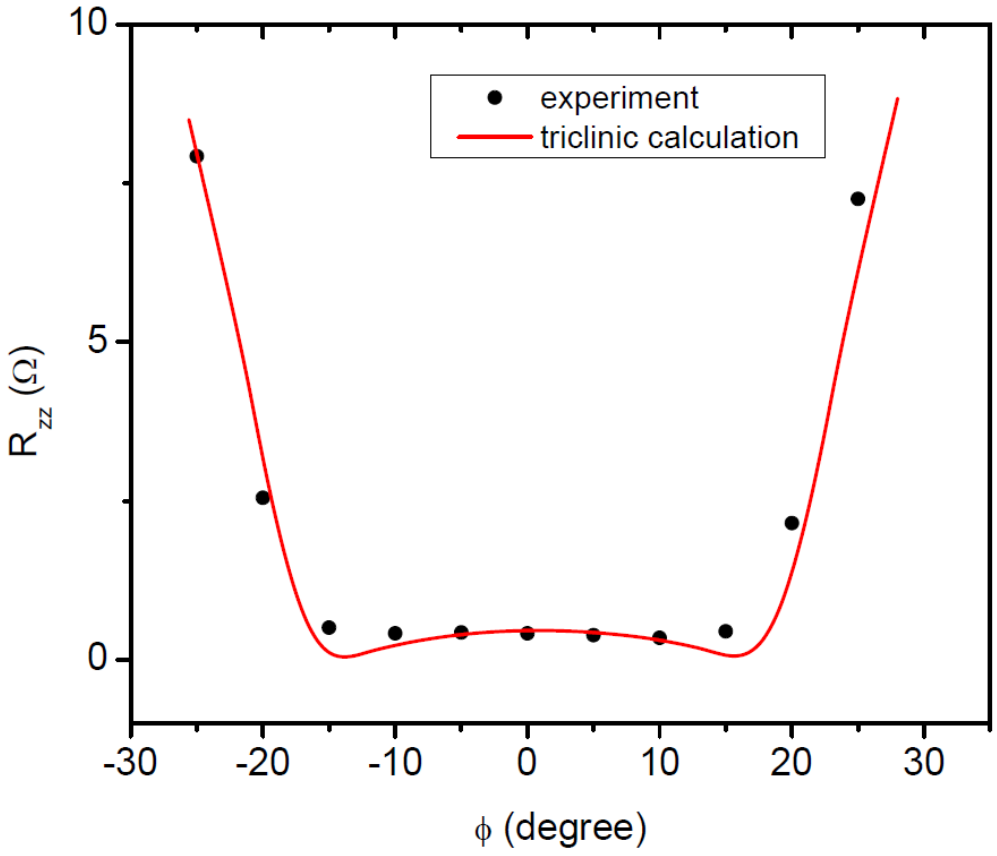

FIG. 4.25 Comparison of calculated magnetoresistance of $(DMET)_2I_3$ for magnetic field rotated in *x*-*y* plane (YAE). The solid line is for calculated data and scatter points are experiment. Experiment and calculation are qualitatively in agreement, with the resistance minima at about $\theta \approx \pm 15°$. The angle ϕ is measured from the *x*-axis.

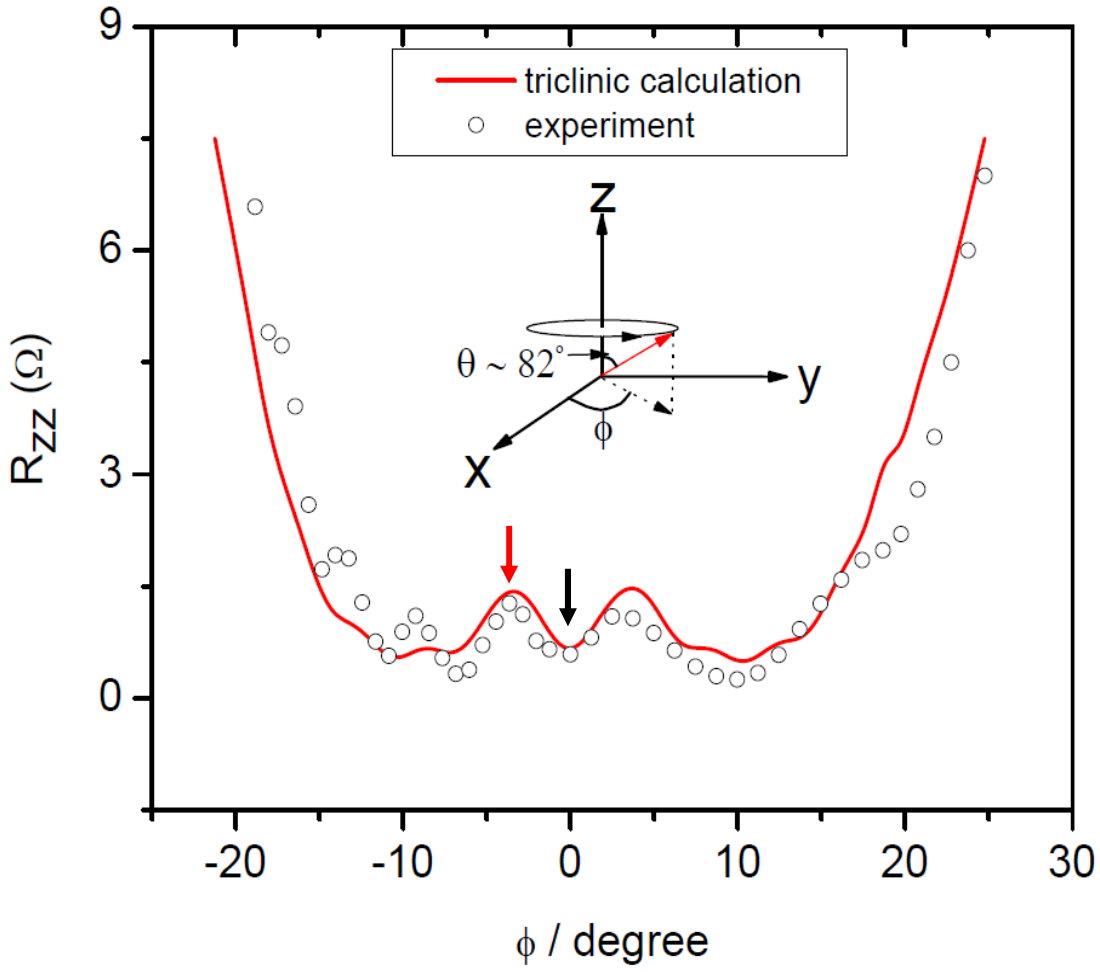

FIG. 4.26 The interlayer magnetoresistance measured (open circle) for $(DMET)_2I_3$ and triclinic calculation (solid like) near the *x*-*y* plane (8^o from *x*-*y* axis) with finite *z*-component. The present calculations are qualitatively in agreement with experimental data.

We now turn our attention to the oscillations observed in *x*-*y* rotations with a finite *z*-component of a magnetic field (*i.e.* the LN-effect). Due to the very complex behavior of these oscillations, their physical meaning has remained somewhat elusive, their properties have not been described in detail. Recently, Lebed and Naughton [4.17] proposed an "interference commensurate (IC)" nature to these oscillations, and they demonstrated that the origin of the LN-oscillations (or IC oscillations) is related to special "commensurate" electron trajectories in a magnetic field, where an average electron velocity along the *z*-axis is non-zero. Ha *et al*, [4.12] measured the interlayer magnetoresistance in $(TMTSF)_2ClO_4$, and their experiment is quantitatively in agreement with the theory for an angle $|\theta| \lesssim 20^o$.

Let us discuss Lebed and Naughton's approach to the IC oscillations in terms of dimensional crossovers, and compare this with our measurements in $(DMET)_2I_3$. In particular, they demonstrated that, in the absence of Landau level quantization for open Fermi surfaces, this "other" quantum effect in a magnetic field, "Bragg reflections" results in a series of 1D to 2D crossovers at the minima of the LN oscillations. In other words, electron wave functions, which are localized on the Q1D conducting chains at arbitrary directions of a magnetic field, become 2D (i.e. delocalized on some planes) at the magnetic field commensurate LN directions. The non-trivial physical origin of these 1D $\rightarrow$ 2D crossovers is said to be related to interference effects between velocity components along the *z*-axis and the electron motion along the *y*-direction [4.17]. These interference effects occur as electrons move along open FS sheets in the extended Brillouin zone and are qualitatively different from those that are responsible for the magic angle effect. They discussed how 1D $\rightarrow$ 2D crossover can lead to the appearance

of LN-oscillation minima in R_{zz} using qualitative arguments. The present triclinic calculations is compared with the experimentally observed magnetoresistance for angle θ = 82° (or 8° from *x*-axis) as shown in **Fig.4.26**. The present calculations are qualitatively in agreement with experimental data. We haven't measured magnetoresistance for other than $\theta = 82^{o}$, but we can extract the data from **Fig. 4.5** for other θ angle. It will be worth to compare the calculations with experimental data for different θ angles.

For electrons localized on conducting *x*-chains (1D), it is natural to expect that the resistivity component ρ_{zz} (i.e. between chains) is nonzero in the absence of impurities and varies as $(\omega_c \tau)^2 \sim H^2$ at high field. Here, $\omega_c = \omega_c(H)$ is one of the cyclotron frequencies related to electron motion along the open FS, and τ is the electron relaxation time. If, at LN-directions of the field, electron wave functions become delocalized (2D), then R_{zz} is expected to have similarities with resistivity in the absence of a magnetic field. Therefore, R_{zz} is expected to saturate at high magnetic fields and to be proportional to τ. In other words, it is possible to show that $R_{zz}(H,\theta,\phi)$ is characterized by an unusual linear behavior for "non-commensurate" directions of a magnetic field, whereas, for "commensurate" directions, $R_{zz}(H,\theta,\phi)$ saturates with increasing magnetic field. This is what Ha *et al.*, showed in Ref 4.12 for $(TMTSF)_2ClO_4$. **Fig. 4.27** presents the results of our field sweeps at each of the minima and maxima in our "*x*-*y* with finite *z*-component" experiment. As predicted by the theory, $R_{zz}(H,\theta,\phi)$ saturates at "commensurate" direction (at minima), while $R_{zz}(H,\theta,\phi)$ (shows some power-law behavior) at "non-commensurate" direction (at maxima) $R_{zz}(H,\theta,\phi) \sim H^{\alpha}$. The experimental data were fit using the polynomial and found that $R_{zz}(H,\theta,\phi) \sim H^2$ as shown in **Fig 4.28**, giving the

exponent $\alpha \sim 2$. As this point, it appears that determination of the precise exponent α is beyond the scope of the one-electron theory, and will require future work. But, the basic idea of saturating magnetoresistance at commensurate angles (minima in angle sweeps) and non-trivial, non-saturation, otherwise, is borne out in the experiments as well as in present triclinic calculation.

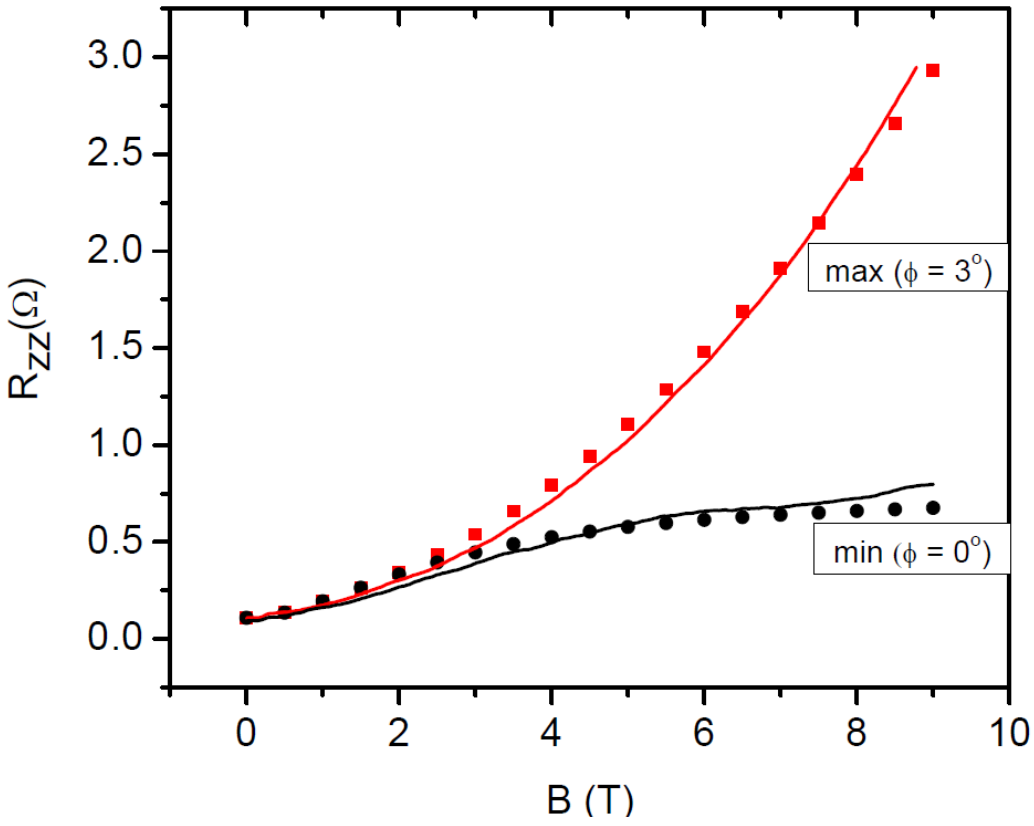

FIG. 4.27 1D-2D topological crossover at certain commensurate and non-commensurate orientations. For maxima (as shown by arrow in **Fig 4.23**), the magnetoresistance is nonsaturating in the field (1D-like), while for minima (as shown by arrow in **Fig 4.23**), it tends to saturation (commensurate, 2D-like). Consistent dependencies occur in the calculated magnetoresistance (solid point) to the experimental data (solid lines). The experimental data for minima at higher field shows slight upward turn due to the temperature fluctuation during measurements.

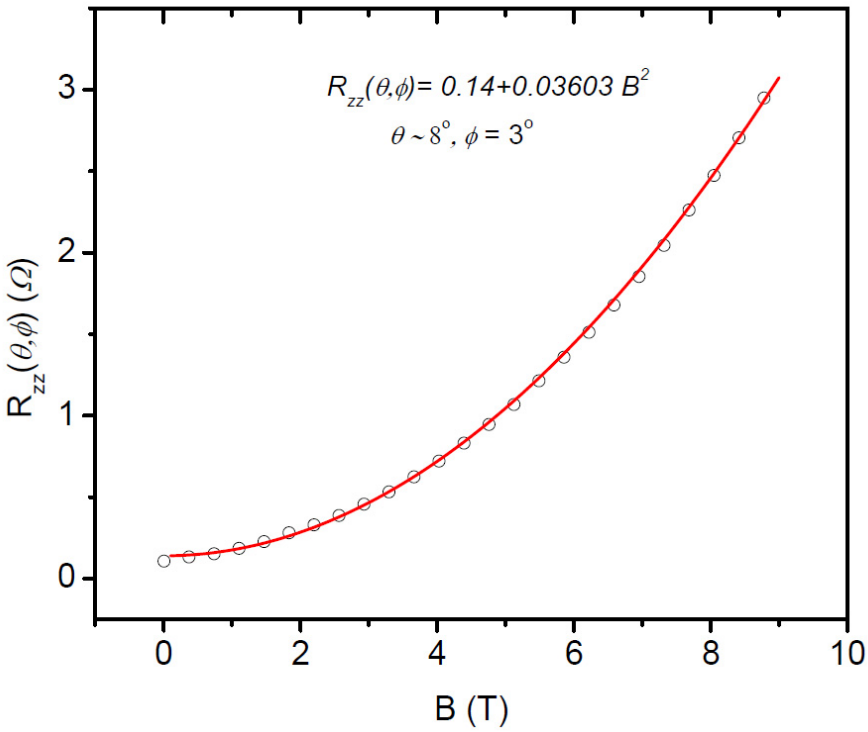

Fig. 4.28 The magnetic field dependence resistance at a non-commensurate orientation (maxima observed in **Fig 4.26**, shown by arrow). The circle is experimentally measured value and solid line is the polynomial fit with R_{zz} = 0.14 +0.03603B^2. We have ignored the low field data due to the superconducting state.

We have also investigated the amplitudes of the magnetoresistance oscillations at positions where the minima are observed. To determine these oscillations, the background magnetoresistance (*i.e.*, in the absence of oscillations) of the experimental and calculated data are fitted using an oscillatory function ($\propto sin^2\theta$) and the deviation from such lines is taken as the amplitude of oscillations, as shown in **Fig. 4.29** and **4.30** for experimental and calculated data, respectively. There is a very reasonable fit to the calculated data using a sine function but the match to the experimental data is far from perfect (**Fig. 4.29**). We have used these fit to estimate the background in the absence of magnetoresistance oscillations.

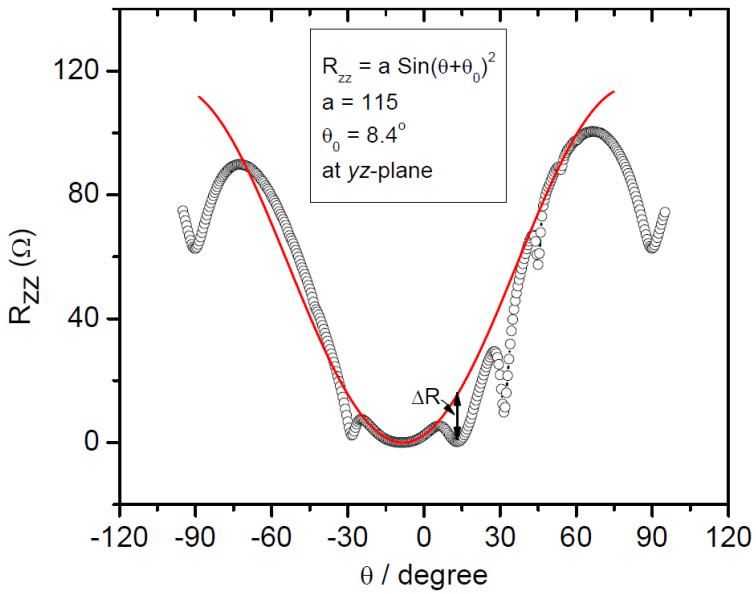

FIG. 4.29 The experimental data (open circles) for field rotating in the *y-z* plane were fit (solid line) using the oscillatory sine function $R_{zz} = a \sin(\theta+\theta_0)^2$ with a = 115 and θ_0 = 8.4°. The deviation of the solid line from the experimental data is taken as the amplitude of the oscillation. Here the angular offset θ_0 = 8.4° is due to the tricilinicity of crystal structure.

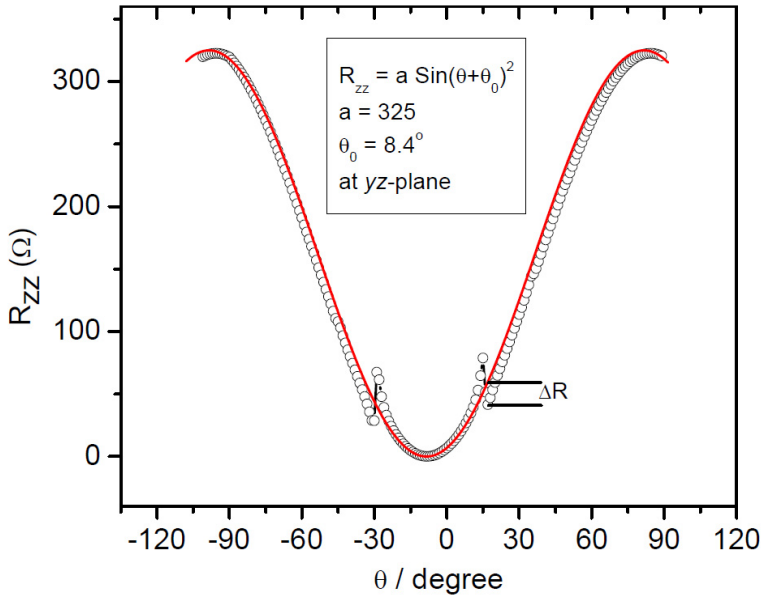

FIG. 4.30 The calculated data for the field rotating in *y-z* plane were fit using the oscillatory sine function $R_{zz} = a \sin(\theta+\theta_0)^2$ with a = 325 and θ_0 = 8.4°. The deviation of the solid line from the experimental data is taken as the amplitude of the oscillation. Here the angular offset θ_0 = 8.4° is due to the tricilinicity of crystal structure.

Now, the amplitudes of the magnetoresistance oscillations $\delta(\Delta\rho/\rho)$ at the magic angles for different ϕ angle as observed experimentally and from present triclinic calculation are shown in **Fig. 4.31** As shown in **Fig 4.4**, the amplitude oscillations decrease when the magnetic field rotation plane rotation approaches to *y-z* plane (the rotation plane is defined by angle ϕ, where $60° \leq \phi \leq 120°$ and $\phi = 90°$ is *y-z* plane). This can be seen more clearly in **Fig. 2.31 (a)**. Interestingly, the lower order oscillation amplitudes *i.e.*, for $n = 0, \pm 1$ and +2, remain about constant, whereas higher oscillation amplitudes ($n \geq 3$) significantly decreases and has minimum for $\phi = 90°$ with n= -2, -3, -*4*, and +5 completely vanish ($\delta(\Delta\rho/\rho) < 1\%$). In triclinic Boltzmann numerical calculations show diminishing oscillation amplitudes for $n = \pm 1$ and vanishing completely for all higher oscillations while approaching the *y-z* plane, as shown in **Fig. 4.31 (b)**. In Kubo analytic model, all oscillations completely vanish within our calculation precision.

As seen, the measured amplitudes indeed decrease, at least for $|n|>1$, while approaching the *y-z* plane, where naively they were expected to be maximal. One possible explanation for this behavior, now observed in both theory and experiment, is that as the magnetic field is tilted away from the Lebed plane, Fermi surface electrons acquire velocity components along the magnetic field which are even larger that those thought to be responsible for the original Lebed effect, resulting in stronger conductivity increases (deeper resistivity minima) for the generalized LNL effect [4.39]. Likewise, detailed differences between theory and experiment may suggest that the one-electron theory employed may be too simplistic, and electron interactions, which are expected to increase in such low dimensional systems, may be involved.

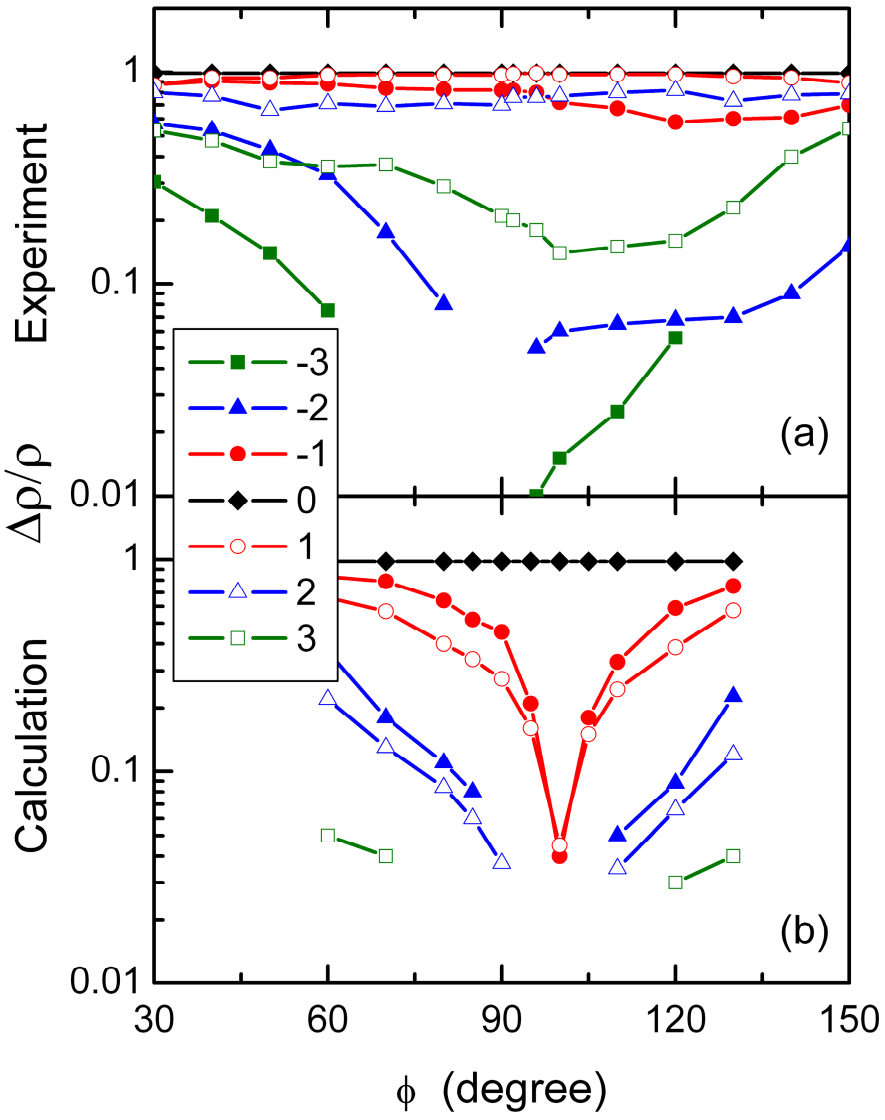

FIG. 4.31 Amplitudes of magnetoresistance oscillations from data and simulations in Fig. 1 for different LNL indices n versus angle ϕ as observed experimentally (upper) and from present triclinic calculations (lower). High index amplitudes decrease significantly while approaching the magic angle orientation $\phi = 90^{\circ}$, but they remain finite. The amplitude in oscillations is calculated by fitting the AMRO data with an arbitrary sine function as shown in **Figs. 4.29** and **4.30**.

Notice that, the amplitudes of the magnetoresistance oscillations in experimental data decrease while the field rotation plane approaches the *y*-*z* plane. However, in our present calculations the amplitudes of these oscillations have minimum values, while approaching to ~ 10° away from the *y*-*z*-plane, this is close to the actual *b*-*c* lattice plane of $(DMET)_2I_3$, is yet to be understand and is left for future study.

Finally, we show in **Fig. 4.32** a the density plot of the resistance $R_{zz}(\theta,\phi)$ in the vicinity of the most conducting *x*-axis. Here, the vertical and horizontal dotted lines represent the DKC and YAE orientations, whereas the oblique dotted lines represent the LNL (LMA+LN) oscillations. Thus three (formerly four) distinct AMRO are observed in experiment and are simulated using true triclinic calculations.

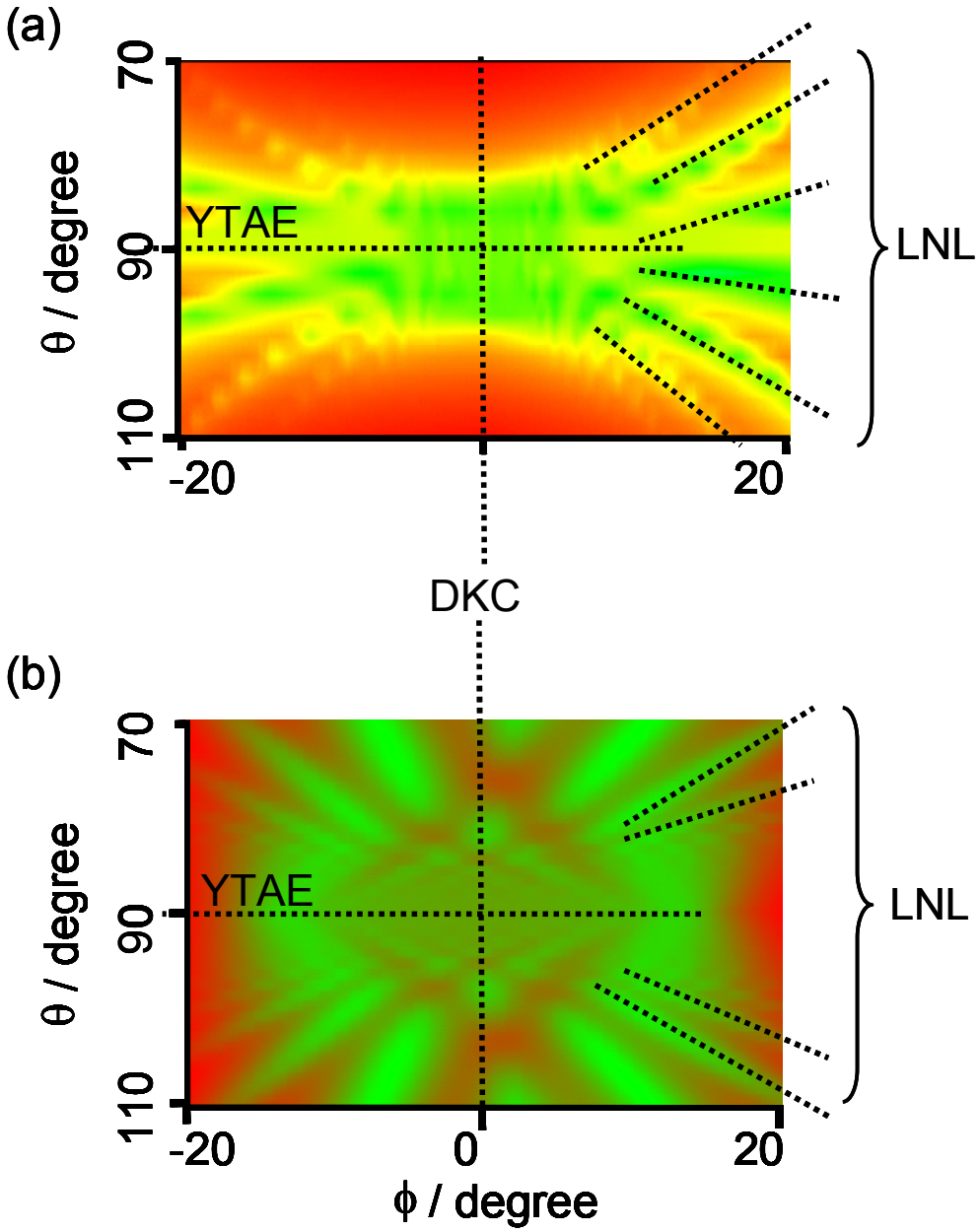

FIG. 4.32 Density plot of the resistance $R_{zz}(\theta,\phi)$ around the most conducting x-axis in $(DMET)_2I_3$ for (a) experimental data and (b) triclinic calculation. The color green (red) corresponds to the maximum (minimum) resistance. The vertical and horizontal dotted lines represent the DKC and YAE orientations, whereas the oblique dotted lines represent the LNL (LMA+LN) oscillations. Thus three (formerly four) distinct AMRO are observed in experiment and are simulated using true triclinic calculations.

4.5 Conclusion

In summary, we have measured the interlayer magnetoresistance of the Q1D organic molecular conductor $(DMET)_2I_3$ at low temperature and across all magnetic field orientations. All known Q1D AMRO effects are now observed in this system. We have numerically solved the interlayer magnetoconductivity tensor for the same field orientations, using the true triclinic lattice parameters, a procedure that should now be employable for other Q1D systems. Even though the LNL amplitudes decrease while the magnetic field rotation plane approaches the *y-z* plane, the calculated results confirm that Lebed oscillations survive, up to at least $n=5^{th}$ order, in contrast to some previous theoretical models which predict their absence. These Lebed oscillations may indeed be "magic" in Q1D molecular conductors.

4.6 References

[4.1] T. Ishiguro, K. Yamaji, and G. Saito, *Organic Superconductors*, Second Edition Springer Verlag, (1998).

[4.2] A. G. Lebed, JETP Lett. **43**, 174 (1986).

[4.3] T. Osada, A. Kawasumi, S. Kagoshima, N. Miura, and G. Saito, Phys. Rev. Lett. **66**, 1525 (1991).

[4.4] M. J. Naughton, O. H. Chung, M. Chaparala, X. Bu, and P. Coppens, Phys. Rev. Lett. **67**, 3712 (1991).

[4.5] W. Kang, S. T. Hannahs, and P. M. Chaikin, Phys. Rev. Lett. **69**, 2827 (1992).

[4.6] S. Uji, C. Terakura, T. Terashima, H. Aoki, H. Nishikawa, I. Ikemoto, and K. Kikuchi,, *Proceeding of the physical Phenomena at High Magnetic Fields III* (World Scientific, London, 1998), p 227.

[4.7] G. M. Danner, W. Kang, and P. M. Chaikin, Phys. Rev. Lett. **72**, 3714 (1994).

[4.8] H. Yoshino, K. Saito, K. Kikuchi, H. Nishikawa, K. Kobayashi, and I. Ikemoto, J. Phys. Soc. Jpn. **64**, 2307 (1995).

[4.9] T. Osada, S. Kagoshima, and N. Miura, Phys. Rev. Lett. 77, 5261 (1996).

[4.10] M. J. Naughton, I. J. Lee, P. M. Chaikin, and G. M. Danner, Synth. Met. **85**, 1481 (1997).

[4.11] I. J. Lee and M. J. Naughton, Phys. Rev. B **57**, 7423 (1998).

[4.12] H. I. Ha, A. G. Lebed, and M. J. Naughton, Phys. Rev. B **73**, 033107 (2006).

[4.13] S. P. Strong, D. G. Clarke, and P. W. Anderson, Phys. Rev. Lett. **73**, 1007 (1994).

[4.14] T. Osada and M. Kuraguchi, Synthetic Metals, **133-134**, 75-77, (2003).

[4.15] R. H. McKenzie and P. Moses, Phys. Rev. Lett. **81**, 4492 (1998).

[4.16] H. Yoshino and K, Murata, J. Phys. Rev. Soc. Jpn. **68**, 3027 (1999).

[4.17] A. G. Lebed and M. J. Naughton, Phys. Rev. Lett. **91**, 187003 (2003).

[4.18] B. K. Cooper and V. M. Yakovenko, Phys. Rev. Lett. **96**, 037001 (2006).

[4.19] A. G. Lebed, N. N. Bagmet, and M. J. Naughton, Phys. Rev. Lett. **93**, 157006 (2004).

[4.20] A. G. Lebed, H. I. Ha, and M.J. Naughton, Phys. Rev. B **71**, 132504 (2005).

[4.21] T. Osada , Physica E , **12**, 272 (2002).

[4.22] K. Wang, T. Osada, Y. J. Jo, and H. Kang, Phys. Rev. Letts. **99**, 017002 (2007).

[4.23] K. Oshima, T. Kambe, T. Sasaki, and T. Kato, Synth. Met. **154**, 249 (2005).

[4.24] Y. Oshima, M. Kimata, K. Kishigi, H. Ohta, K. Koyama, M. Motokawa, H. Nishikawa, K. Kikuchi, and I. Ikemoto, Phys. Rev. B **68**,054526 (2003).

[4.25] Y. Ishikawa, M. Sc. Thesis, Tokyo Metropolitan University, 1989.

[4.26] I. J. Lee and M. J. Naughton, Phys. Rev. B **58**, R13343 (1998).

[4.27] M. J. Naughton, I. J. Lee, P. M. Chaikin, and G. M. Danner, Synth. Met. **85**, 1481 (1997).

[4.28] I. J. Lee, M. J. Naughton, G. M. Danner, and P. M. Chaikin, Phys. Rev. Lett., **78**, 3555 (1997).

[4.29] H. Yoshino, A. Oda, K. Murata, H. Nishikawa, K. Kikuchi, and I. Ikemoto, Synth. Met. 120, 885 (2001)

[4.30] G. Montambaux and P. B. Littlewood, Phys. Rev. Lett. **62**, 953 (1989).

[4.31] L. Chen and K. Maki, Synth. Met. **29**, F493 (1989).

[4.32] A. G. Lebed and P. Bak, Phys. Rev. Lett. **63**, 1315 (1989).

[4.33] V. M. Yakovenko, Phys. Rev. Lett. **68**, 3607 (1992).

[4.34] P. M. Chaikin, Phys. Rev. Lett. **69**, 2831 (1992).

[4.35] G. M. Danner and P. M. Chaikin, Phys. Rev. Lett. **75**, 4690 (1995).

[4.36] H. Yoshino, (unpublished).

[4.37] N. W. Aschroft and N. D. Mermin, *Solid State Physics*, Harcourt Asia PTE Ltd, Singapore (2001).

[4.38] H. Yoshino, K. Murata, K. Saito, H. Nishikawa, K. Kikuchi, and I. Ikemoto, Phys. Rev. B **67**, 035111 (2003).

[4.39] Pashupati Dhakal, H. Yoshino, J. I. Oh, K. Kikuchi, and M. J. Naughton, Phys. Rev. Lett. **105**, 067201 (2010).

Chapter 5

Superconductivity and Upper Critical Field in $(DMET)_2I_3$

5.1 Introduction

After the discovery of superconductivity in Bechgaard salts by Jerome *et al.* in 1980 [5.1], there has been a sustained period of interest in the study of the existence and origin of superconductivity in molecular organic superconductors. This is because, not only is it remarkable that organic materials superconduct, let alone conduct, but aspects of the superconductivity were immediately found to be anomalous. The study of impurities in these superconductors by Choi *et al*. [5.2] showed that the superconductivity is of unconventional type. Conventional superconductors are only mildly perturbed by the impurities that are not magnetic, but they found that radiation doses introducing defect concentrations of only a few 100 ppm were found to completely suppress superconductivity. Takigawa *et al.* [5.3] performed the first NMR experiments of the NMR spin-lattice relaxation rate T_1^{-1} in the superconducting state of $(TMTSF)_2ClO_4$, and found $T_1^{-1} \sim T^3$ below T_c, consistent with a zero-field superconducting state with nodal lines on the open Fermi surface. However, it turns out they didn't explore temperatures sufficiently low enough to be definitive.

Lebed in 1986 [5.4] predicted a divergence of the upper critical field (H_{c2}) in these superconductors, based on a novel field-induced dimensional crossover concept. This theory anticipated a complete recovery of superconductivity in very intense magnetic fields, for the condition of magnetic field parallel to the *x*-*y* plane but perpendicular to the chains (*i.e.* in the *y*–direction). This reentrance has yet to be

definitely observed experimentally. However, a pronounced positive upturn in upper critical field with no sign of saturation, and with H_{c2}^{y} growing larger than H_{c2}^{x}, has been observed. In addition, H_{c2}^{y} well-exceeds the Pauli paramagnetic limit (the magnetic field required to destroy the spin-singlet Cooper pairs) [5.5, 5.6, 5.7, 5.8]. Later Lee *et al.*, found that the spin susceptibility measured via NMR Knight shift remained unchanged upon cooling through the superconducting state in $(TMTSF)_2PF_6$ [5.9]. The unusual high critical fields, as well as the observed absence of resonant frequency shift in the Knight shift suggest spin triplet pairing may be responsible for the superconductivity. In this Chapter, we will discuss superconductivity in Q1D systems, in general, and in $(DMET)_2I_3$, in particular. We present H_{c2} data for $(DMET)_2I_3$ for field carefully oriented along the three principal axes and compare our results with those of the Bechgaard salts. These result may help to understand whether the anomalous upper critical field is unique to $(TMTSF)_2X$ or is a more generalized characteristic of all Q1D systems. Also, the anisotropy in the upper critical field, for the field with in the *y*-*z* plane, will be presented.

5.2 Superconductivity in Q1D Systems

The Bechgaard salt $(TMTSF)_2PF_6$ has a superconducting transition transition of approximately 1.2 K under 6 kbar pressure (it is a spin density wave state at ambient pressure). Soon after the discovery of the superconductivity, the general belief was that the nature of the superconductivity is conventional, meaning that the order parameter is *s*-wave singlet. The primary evidence for conventionality of the superconducting state was from upper critical field measurements. For example, Murata *et al.*[5.10] showed early evidence of singlet pairing as they measured the temperature–dependent upper critical

field in the ambient pressure superconductor $(TMTSF)_2ClO_4$ down to 0.5 K (which was about $T_c/2$), and showed it tends to saturate at low temperature. $H_{c2}(T)$ was shown to be anisotropic, consistent with the crystal and band structures, but nonetheless, conventional (*i.e.*, $H_{c2}^{x} > H_{c2}^{y} > H_{c2}^{z}$), as reproduced in **Fig 5.1**. Notice also that the highest critical field value for *B*//x appears to tend to saturate at zero temperature at about ~ 2.5 T. This is below the limit [5.11, 5.12] at which the single Cooper pairs breaks (Pauli paramagnetic limit).

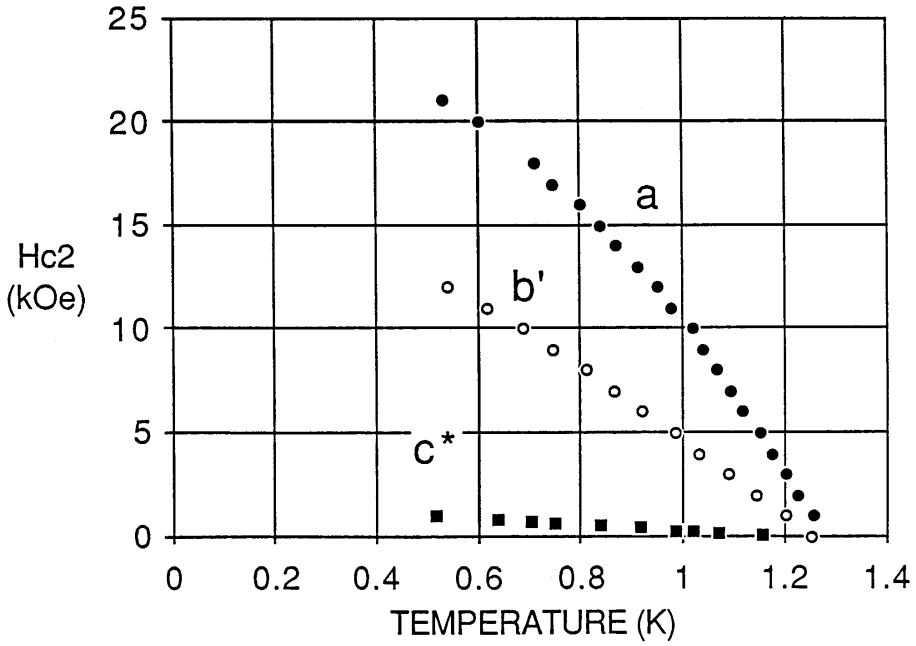

FIG. 5.1 Temperature dependence of H_{c2} with magnetic field along the *x (a), y (b')* and *z (c*)*-axes in $(TMTSF)_2ClO_4$ [from Murata *et al.* 5.10].

Around the same time as his prediction of the AMRO magic angle effect, Lebed also proposed a type of field-induced dimensional crossover effect relating to the superconducting state of Q1D superconductors [5.4]. He used the typical energy dispersion relation of a Q1D system, the tight binding approximation as in Eq. 2.4 given by

$$\mathrm{E}(\vec{k}) = -2t_x \cos(k_x a) - 2t_y \cos(k_y b) - 2t_z \cos(k_z c) - \mathrm{E}_F \tag{5.1}$$

where the parameters have the same meaning as discussed in Chapter 2. When the magnetic field is applied along the *y*-axis, an electron moving along the *z*-axis experiences a Lorentz force given by

$$F_L = \frac{\hbar d\vec{k}}{dt} = e\vec{v} \times \vec{B},$$

where the velocity $\vec{v} = \frac{1}{\hbar}\frac{\partial E(\vec{k})}{\partial \vec{k}}$. (5.2)

From Eq. (5.1) and (5.2), an electron moving along the *z*-axis can be shown to follow a trajectory given by $z = 2c\left(\frac{t_c}{\hbar\omega_c}\right)\cos Gx$ (5.3)

where $G = -eBc$ is a magnetic wave vector and $\omega_c = eBcv_F/\hbar$ is the frequency with which the electron crosses the Brillouin zone in the *z* (c^*) direction. Lebed pointed out that the motion of this electron is oscillatory along the *x*-axis, with *z*-direction oscillation amplitude $4ct_c / eB\hbar$. That is, this amplitude is inversely proportional to the magnetic field strength ($z \sim 1/B$). This leads to the conceptualization of a localization of electronic motion in the *x*-*y* plane as the field increases, since *B* can be increased to the point where $z<c$, the interlayer separation distance. Lebed called this field-induced dimensional crossover (FIDC), as depicted in **Fig 5.2** in neighboring TMTSF molecular chains.

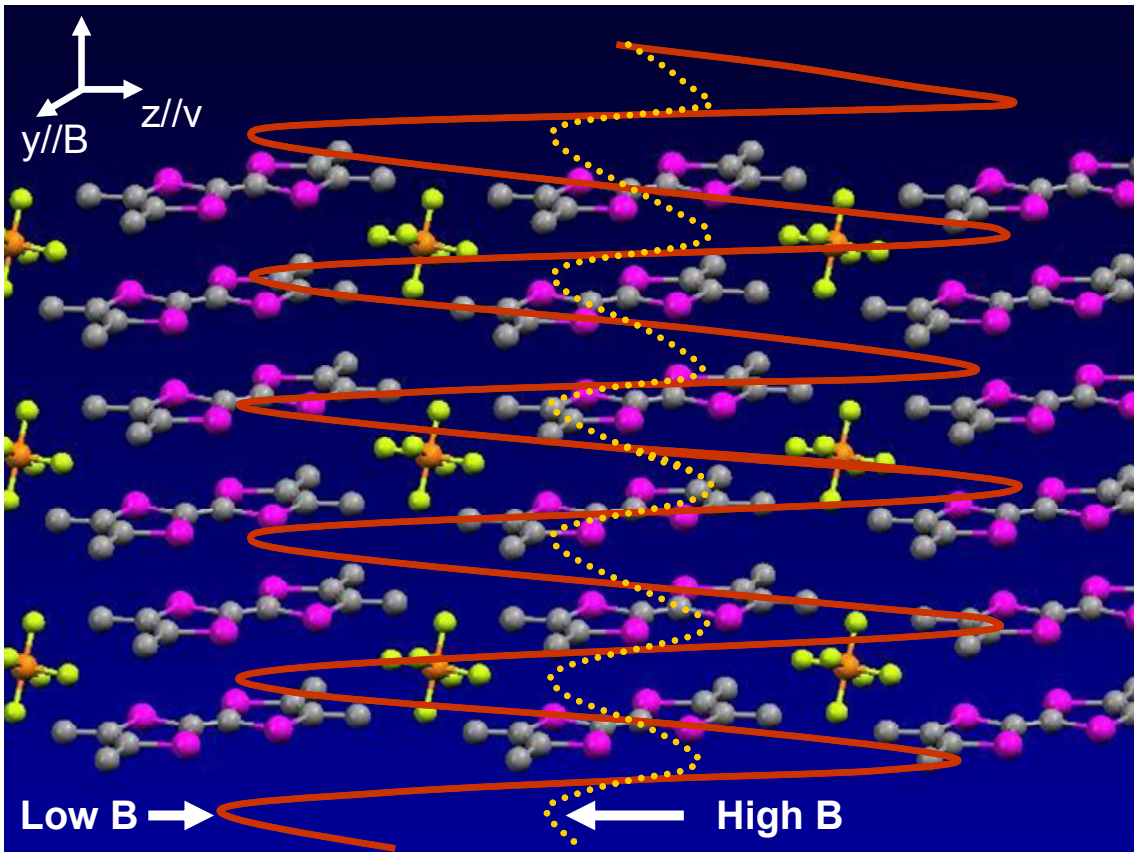

FIG 5.2 A schematic display of the field induced dimensional crossover (FIDC) mechanism. The electron motion in the vicinity of single chain is displayed here for simplicity. The amplitude of oscillatory motion along the *z*-direction is proportional to *1/B* when *B//y*. Therefore, with a sufficient field, the electron motion becomes localized within the *x-y* plane, as depicted by the dotted line.

In a strong magnetic field, when $\hbar\omega_c >> t_c$, a crossover from a 3D Abrikosov vortex lattice to a 2D Josephson one is said to take place. In this crossover regime, the ability of magnetic field parallel to the plane to break Cooper pairs is reduced, and eventually, orbital frustration vanishes, leading, in theory, to the reentrance of superconductivity at very high field [5.13, 5.14, 5.15, 5.16]. The *H-T* phase diagram according to the FDIC concept is shown in **Fig 5.3**.

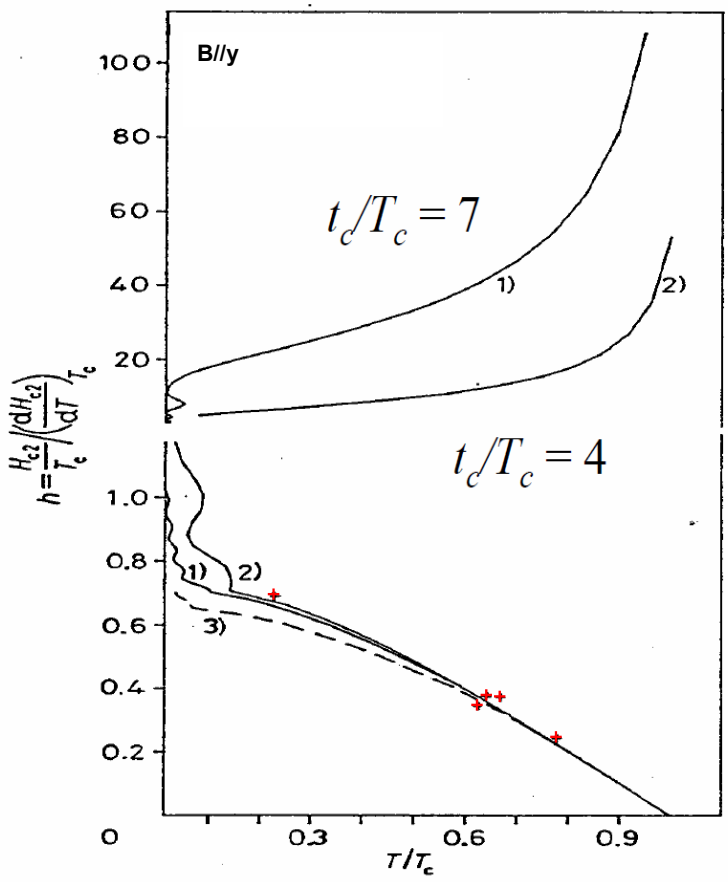

FIG. 5.3 *H-T* phase diagram where FIDC quenches orbital pair breaking effect. Curve 1 and 2 are for triplet pairing with $t_c/T_c = 7$ and 4 respectively for *B//y*-axis. Where as curve 3 is for single pairing with $t_c/T_c = 7$. The cross marks are the experimental data for $(TMTSF)_2ASF_6$ at $P = 11$ kbar. For $(TMTSF)_2ClO_4$, $t_c/T_c \sim 7$ [5.13].

In fact, evidence for such a dimensional crossover effect and a potential re-entrance of the superconductivity for field parallel to the *y*-axis have been observed by Lee *et al.* [5.2-5.4]. They found that the temperature where the onset of superconductivity in $(TMTSF)_2ClO_4$ is observed did not follow the conventional *H-T* phase diagram. The *H-T* phase diagram instead shows strong upward curvature at low *T* and H_{c2} for *H//y* (*H//b'*) is several times larger than the Pauli paramagnetic limit at the lowest *T*. A more

extensive study on $(TMTSF)_2PF_6$ by Lee *et al.* [5.5, 5.6] shows conventional anisotropic behavior of $H_{c2}^{a} > H_{c2}^{b'} > H_{c2}^{c^*}$ near T_c, but with an unconventional crossover occurring at high field, with $H_{c2}^{b'}$ growing larger than H_{c2}^{a} and showing no signature of saturation, also shown in **Fig. 5.4**.

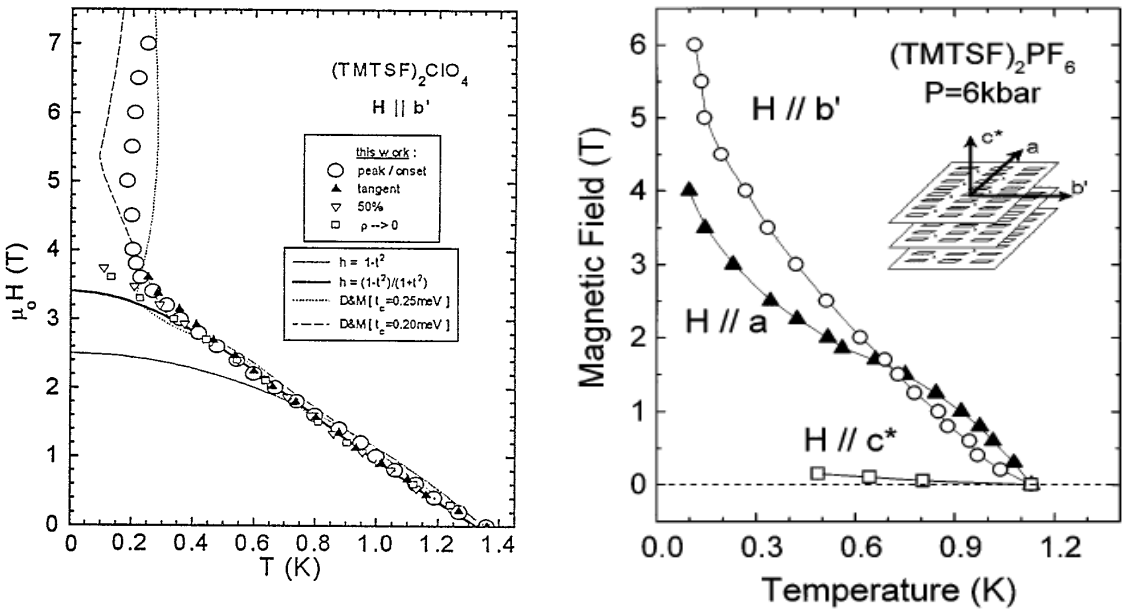

FIG. 5.4 *H-T* phase diagram in (left) $(TMTSF)_2ClO_4$ for the field along *y (b')*-axis [5.5] and (right) $(TMTSF)_2PF_6$ for field aligned along the *x* ***(a)***, *y****(b')***, and *z* ***(c^*)*** directions [5.6].

The upper critical fields shown in **Fig. 5.4** were obtained from resistivity measurements. Later, simultaneous resistivity and magnetic measurements using a microcantilever magnetometer to record the magnetic torque, were carried out by Oh and Naughton on $(TMTSF)_2ClO_4$ [5.17]. They found that the upper critical fields measured by resistivity and magnetization coincided. Furthermore, Ha *et al.* [5.18] made measurements on crossed bicrystals of $(TMTSF)_2ClO_4$ for a tunneling experiment. They observed a prominent zero-bias conductance peak (ZBCP), which they interpreted as

consistent with unconventional superconductivity. These recent experiments provide some additional evidence of unconventionality, in particular spin triplet (*p*- or *f*-wave) superconductivity in the $(TMTSF)_2X$ organic superconductors.

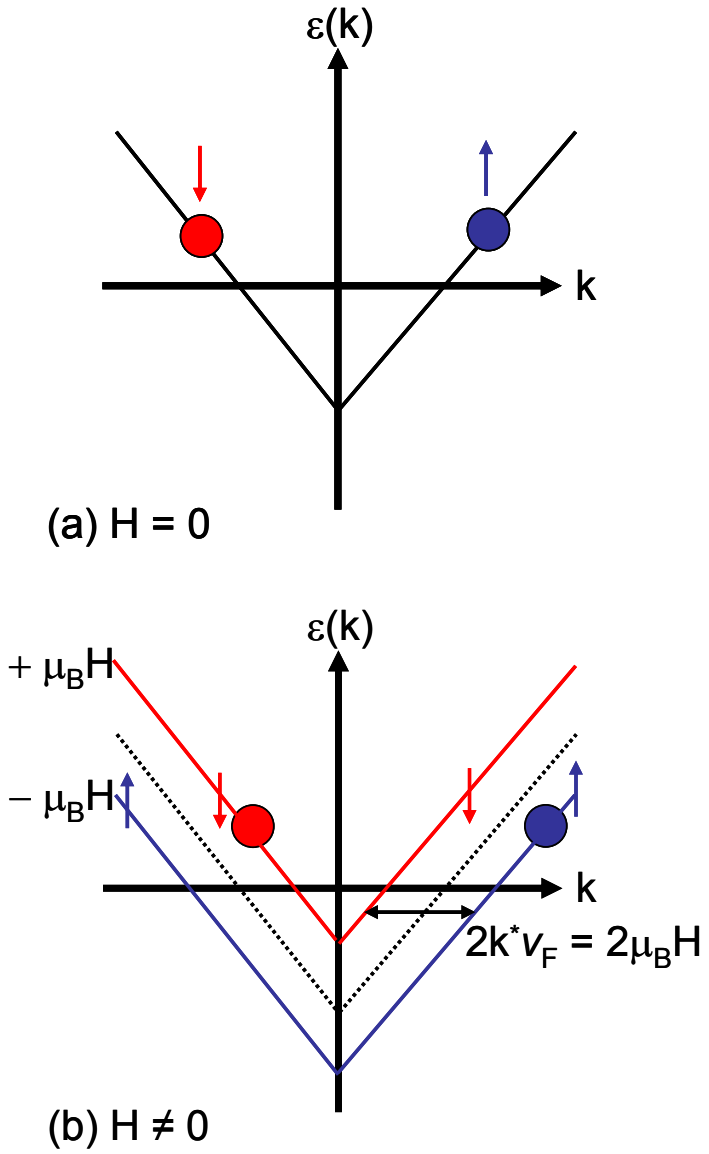

FIG. 5.5 A 1D electron spectrum near the Fermi level. The arrows represent spin up or down.

There may be another mechanism besides triplet superconductivity to explain the observed anomalous H_{c2}. Fulde and Ferrell, and independently Larkin and Ovchinnikov, often referred to as FFLO or LOFF, were the first to realize that the destructive influence of Pauli paramagnetism can be mitigated by displacing the Fermi sphere of spin up (↑) and spin down (↓) electrons, relative to each other, by a wave vector, which is roughly given by $k_F(\uparrow) - k_F(\downarrow) = 2k^*$ [5.19, 5.20]. **Fig. 5.5** shows a 1D electron spectrum near the Fermi level under zero **(a)** and a large enough **(b)** magnetic field. If one can pair electrons with opposite signs, one (↑) at $k_{TOT} = k_F + k^*$ and the other (↓) at $k_{TOT} = -k_F + k^*$ then the total momentum of the pair will be $2k^*$ (as opposed to $k_{TOT} = 0$ for the conventional case). Therefore, by moving the Fermi surface by an amount k^*, the pairing condition for spin singlet superconductivity, which requires that opposite spins with equal and opposite momentum and equal energy should be paired, can be fulfilled over part of the Fermi surface. However, electrons can not pair at all on the other parts of the Fermi surface.

According to FFLO, this non-uniform superconducting state with finite momentum is more stable than the uniform solution, if the Zeeman energy is large enough. An inhomogeneous order parameter which has been considered by Larkin and Ovchinnikov [5.20], is given by $\Delta(r) = \Delta(x, y)\cos Qz$, where the vector Q serves as a pseudo-momentum for the Cooper pairs in the magnetic field. Such a FFLO state have been reported in the Q2D organic superconductor κ-(BEDT-TTF)$_2$Cu(NCS)$_2$ [5.21], though this remains up for debate. Note also, the experimental evidence for the existence

of FFLO state in $CeCoIn_5$, a strongly anisotropic heavy Fermions compound and superconductor has been reported [5.22].

Recently, Shinagawa et al., [5.23] showed the ^{77}Se NMR Knight shift at low fields revealing the decrease in spin susceptibility (χ_s) consistent with singlet spin pairing most likely with gap nodes. However, the H-T phase diagram still remains puzzling. Also, the study on the in-plane anisotropy of the onset of superconductivity in $(TMTSF)_2ClO_4$ by Yonezawa et al., [5. 24] reported the evidence for a transition with in the superconducting state and attributed it to shifting of the symmetric principal axis away from the one of the which points along *y* at low fields, shifts away from this direction around 3T but evolves back toward the *y*- axis at higher fields, consistent with the singlet scenario. The possibility remains, therefore, that superconductivity in $(TMTSF)_2X$ is spin singlet, perhaps with a FFLO state or perhaps with a crossover in high magnetic field between the conventional singlet and unconventional singlet or spin triplet.

In the next subsections, we will discuss our upper critical field measurements carried out in $(DMET)_2I_3$, which has similar anisotropy and crystal structure as the $(TMTSF)_2X$ Bechgaard salts.

5.3 Upper Critical Field in $(DMET)_2I_3$

As mentioned, interpretation of the unusual the upper critical field behavior in Bechgaard salts, especially along the principal axes, is still debatable. Therefore, it worthwhile investigating $H_{c2}(T)$ in other Q1D systems with similar crystal structure and anisotropy. Here, we have measured the upper critical field of $(DMET)_2I_3$ along the three principal axes. To measure $H_{c2}(T)$ along these axes, the sample needs to be aligned along the direction of the field with high accuracy. As discussed in Chapter 3, we have employed a dual-axis rotator, which allows us to align a sample in any desired direction, with precision $\delta\theta$ = 0.003° and $\delta\phi$ = 0.0025°. We have used the external rotator (goniometer) to find the sample *x*-*y* plane [in case of $(DMET)_2I_3$, this is the *b*-*a'* plane]. From our AMRO measurements, we found that the resistivity of the sample has a local minimum when the magnetic field is along the *x*-*y* plane. We measured the resistance of the sample, rotating the sample in a plane perpendicular to this plane, as shown in **Fig 5.6**. Then, the external goniometer was set at a fixed position where the resistance is minimum and the internal sample stage was rotated using a stepper motor to find the precise *y*-axis. From the same AMRO measurements, the resistance of the sample was maximal when the field was along the *y*-axis, as shown in **Fig. 5.7**. Thus, the resistance of the sample itself is a good way (perhaps the only way) to find the precise alignment of the magnetic field along the principal axes. Once we were able to find the precise *y*-axis of the sample, successive 90 degree rotation of goniometer and stepper motor allowed us to find the *z* and *x*-axes with high precision *i.e.*, $\delta\phi$ = 0.05° and $\delta\theta$ = 0.05°.

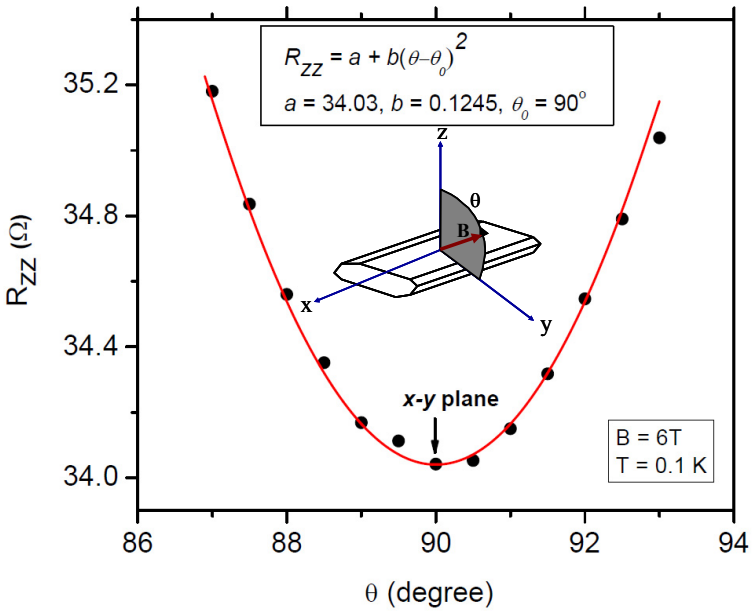

FIG. 5.6 The measured resistance of the sample when the field is rotated in the plane perpendicular to *x*-*y* plane at 6T and 0.1 K. The local minimum was observed when the field crossed the *x*-*y* plane. The measured data point was fitted with a polynomial of second order (red line) and local minimum was identified as *x*-*y* plane.

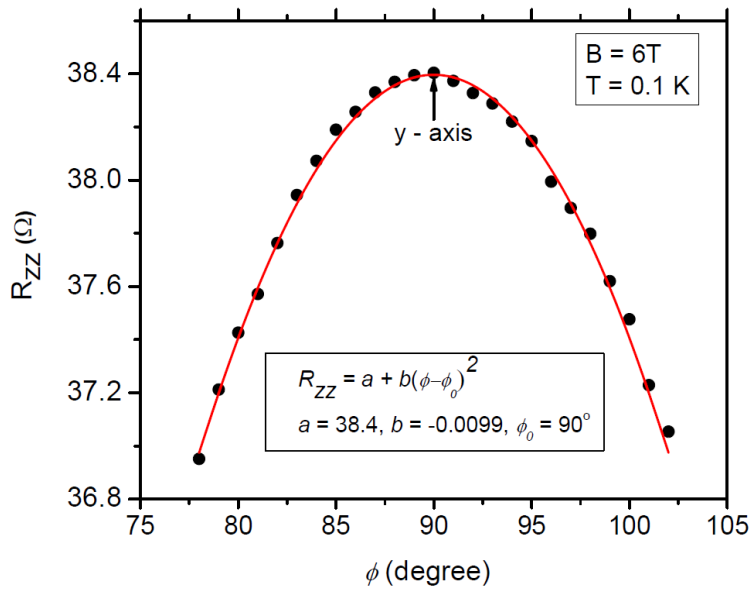

FIG. 5.7 The measured resistance of the sample when the field is rotated in the *x*-*y* plane at 6T and 0.1 K. The local maximum was observed when the field is along the *y*-axis. The measured data point was fitted with a polynomial of second order (red line) and local maximum was identified as *y*-axis.

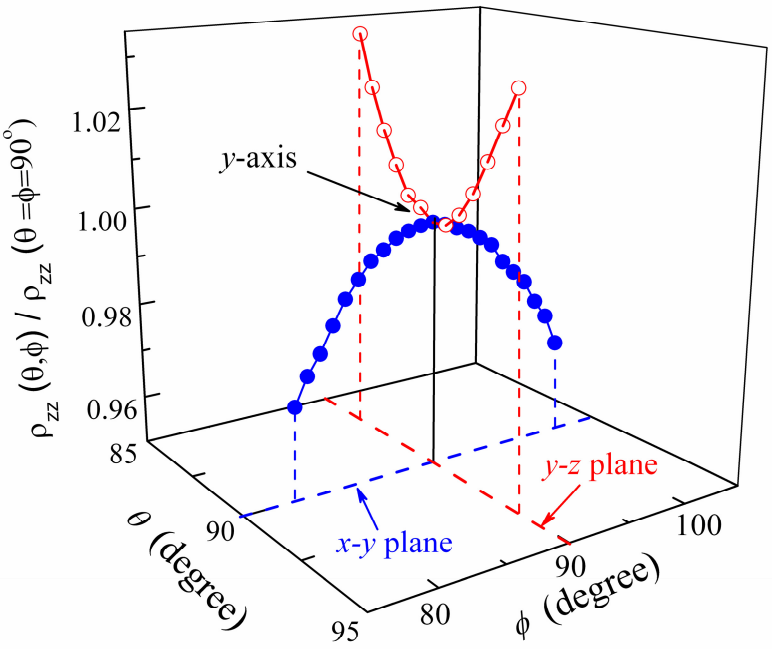

Fig. 5.8 Summarizing **Fig 5.6** and Fig **5.7** in a single plot. The resistance of the sample shows the local minima for the field rotation in *y*-*z* plane and the resistance of the sample shows the local maxima for the field rotation in *x*-*y* plane. The intersection of these two rotation plane is *y*- axis.

Once the magnetic field was aligned as accurately as possible along the *y*-axis, the magnetic field was brought back to 0T. Resistivity versus magnetic field measurements were then recorded at a number of fixed temperatures, using low excitation amplitude AC current. The typical current used in the measurements was 1 μA, corresponding to current density ~ 10^{-3} A/cm^2. The measurement was also done for higher (5 μA) and lower (0.1μA) current to see if there was any sign of Joule self-heating. It was found that there was no significant Joule heating in this current range so that 1μA current was used during all the measurements. **Fig. 5.9** shows the interlayer resistance versus magnetic field at different temperatures for field along the *y*-axis. From preliminary measurements, it was found that the upper critical field is very low. Therefore, for more precise

measurement of the critical field, the magnetic field was scanned from negative to positive field. The data shown in **Fig. 5.9** have a very large noise level. To remove the noise level, the curve was digitally smoothed using the 50 point "adjacent averaging" option in Origin 7.1 data analysis software. **Figure 5.10** shows a comparison of the smoothed with raw data for one particular temperature (T = 0.1K), giving an indication of the veracity of smoothed result. **Fig 5.11** shows the systematic shift of H_{c2} with temperature using the smoothed results. Similar measurements were made for field along the most conducting direction (*x*-axis) as shown in **Fig. 5.12**.

The transition out of the superconducting state, upon increasing the magnetic field, is seen as a gradual rise of resistance, ending in a quasi-linear dependence on field in the normal metal state. Since there is not any well defined rule to extract the upper critical field from such experiments, we have employed different criteria: O (superconducting onset), J (upper junction point), M (mid point of transition), Y (lower junction point) and Z (zero resistance point), as shown in **Fig. 5.13**. In addition, for some upper critical field data points the sample was cooled down to the base temperature with constant magnetic field along the *x*-axis**. Figure 5.14** shows the *H-T* phase diagram for the upper critical field obtained using these criteria. Since all curves show the similar temperature dependence, we have plotted the upper critical field versus the temperature taking in to account the mid point criterion as shown in **Fig. 5.15**. Recalling that the upper critical field is anomalous for the field parallel to the (*b'*) *y*-axis in $(TMTSF)_2X$, so much of the present study was focused on measurements of H_{c2} along this axis. Similar criterion were taken to extract the upper critical field for the field along *x* and *z*- directions.

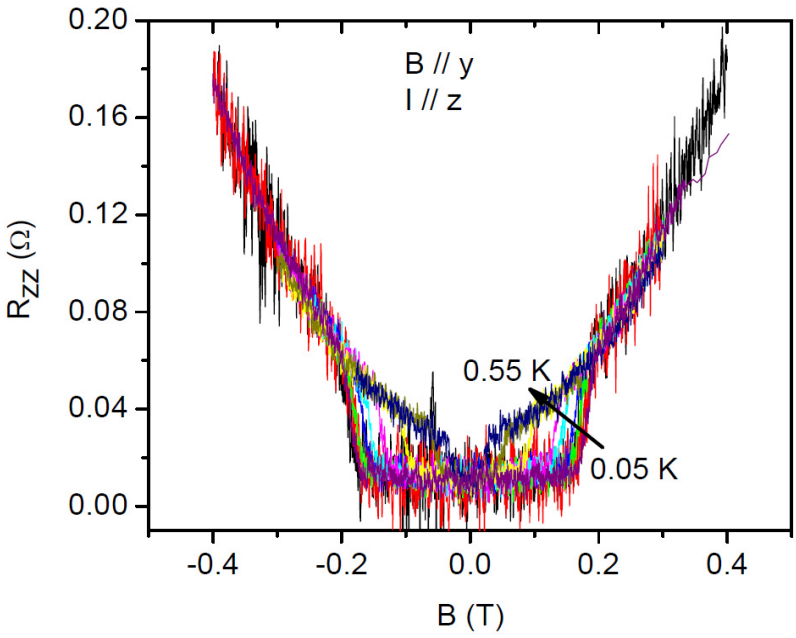

FIG. 5.9 The raw data for the magnetic field dependent interlayer resistance at different temperatures when the field is parallel to the *y*-axis.

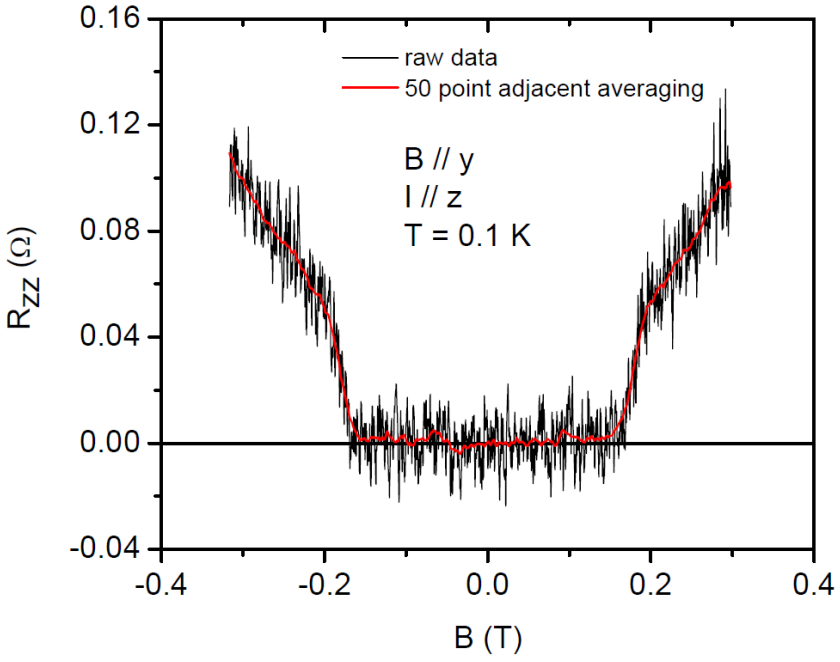

Fig. 5.10 comparison of the smoothed with raw data for one particular temperature (T = 0.1 K), giving an indication of the veracity of smoothed result.

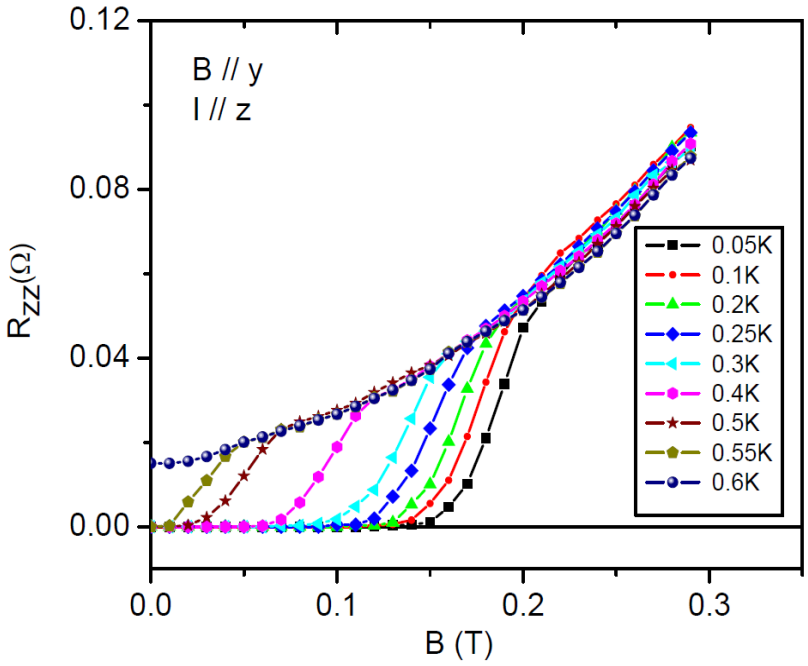

FIG. 5.11 The smoothed data for the magnetic field dependent interlayer resistance at different temperatures when the field is parallel to the *y*-axis showing the systematic shift of H_{c2} with temperature.

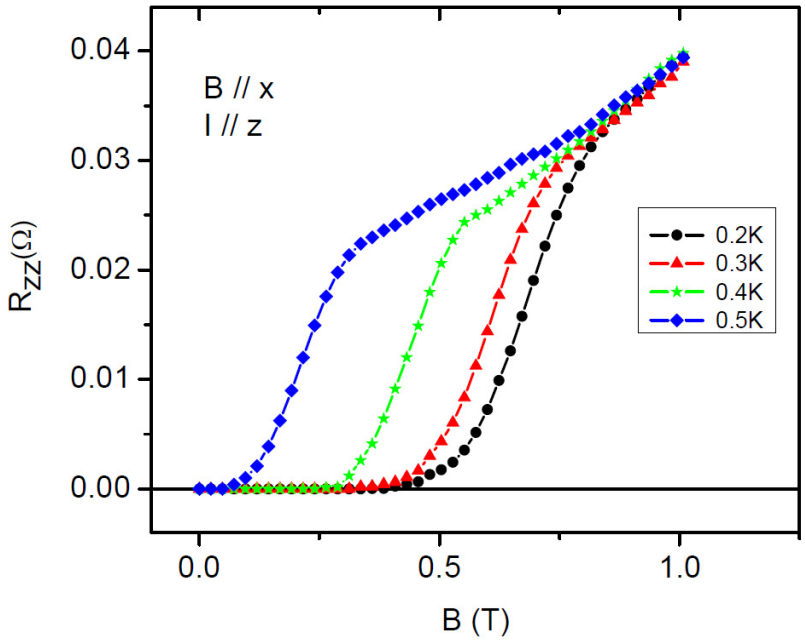

FIG. 5.12 Determination of H_{c2} from resistance versus magnetic field data. employed different criteria: *T* (superconducting onset), *J* (upper junction point), *M* (mid point of transition), *Y* (lower junction point) and *Z* (zero resistance point).

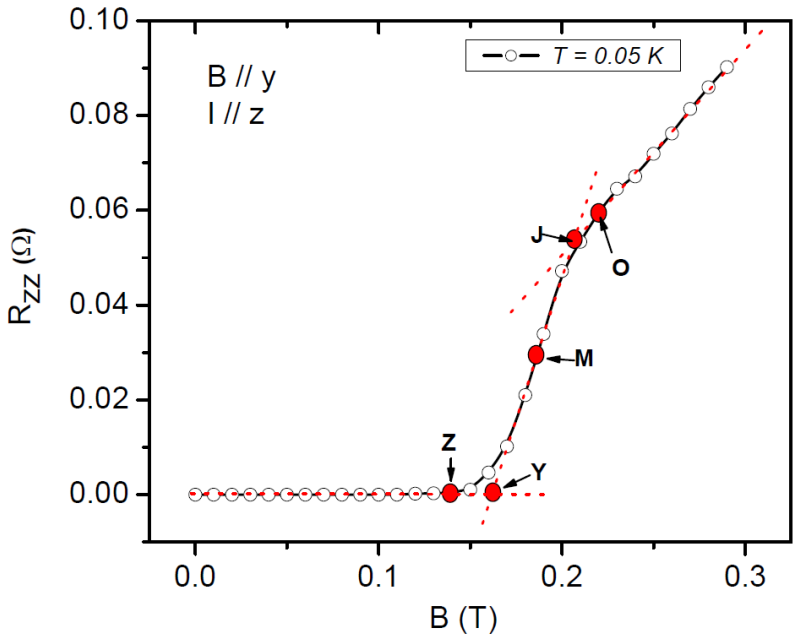

FIG. 5.13 Magnetic field dependent interlayer resistance at different temperatures when the field is parallel to the *x*-axis. Data points on the plots are interpolated from the measurements. The broad superconducting transition has been observed showing the systematic shift of transition.

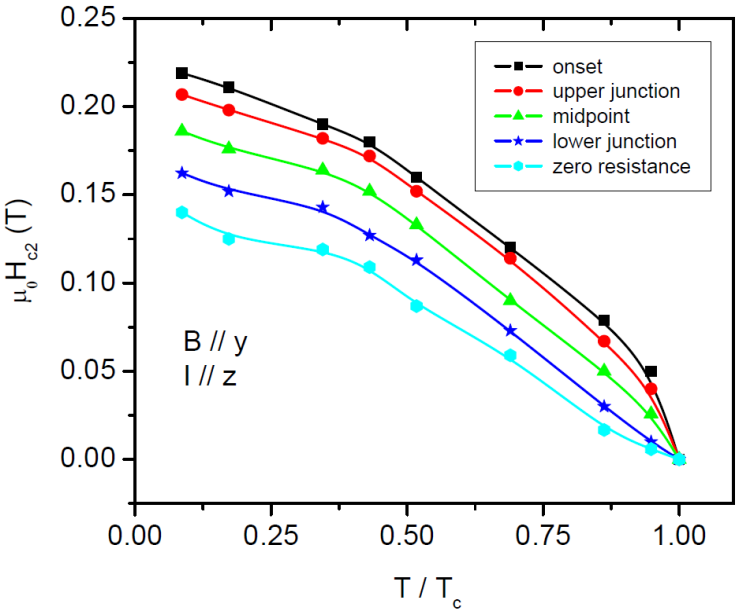

FIG. 5.14 *H-T* phase diagram for superconducting state of $(DMET)_2I_3$ for field aligned along the *y* – direction, for different H_{c2} criteria as described in **Fig. 5.12**, where *T* (superconducting onset), *J* (upper junction point), *M* (mid point of transition), *Y* (lower junction point) and *Z* (zero resistance point). The lines are guides to the eye.

Figure 5.15 shows a cumulative phase diagram for all three directions using the midpoint *(M)* criterion. The measured H_{c2} is fitted with the well-known Werthamer-Helfand-Hohenberg (WHH) formula, given by

$$H_{c2}(T) = H_{c2}(0)\left[1-\left(\frac{T}{T_c}\right)^2\right] \tag{5.4}$$

where $H_{c2}(0)$ is the zero temperature critical field. It is clear that, unlike the lack of saturation in $(TMTSF)_2ClO_4$ [5.5] and $(TMTSF)_2PF_6$ [5.6] $H_{c2}(T)$ saturates as T approaches zero for all directions *B//x, B//y*, and *B//z* in $(DMET)_2I_3$. That is, we do not observe any indication of FIDC in this material. We have extracted the estimated value of the zero temperature critical field along the three directions to be 0.79 T, 0.186 T and 0.019 T, respectively. Using the Ginzburg-Landau (G-L) relation, $H^i_{c2}(0) = \phi_0 / 2\pi\xi_j(0)\xi_k(0)$, where ϕ_0 is the flux quantum and $\xi_i(0)$ is the zero temperature anisotropic coherence length along the i^{th} direction, these $\xi_i(0)$'s can be obtained as $\xi_x(0)$ = 271.23 μm, $\xi_y(0)$ = 63.86 nm, and $\xi_z(0)$ = 6.52 nm. That is, the anisotropy of the coherence length is found to be $\xi_x : \xi_y : \xi_z$ = 41.2 : 9.8 : 1. On the basis of the tight binding approximation, this anisotropy, due to orbital effects, is related to the band structure anisotropy via $\xi_x : \xi_y : \xi_z = (a_x/2)t_x : a_y t_y : a_z t_z$, where a_i and t_i are the lattice parameters and transfer integrals, respectively [25]. Using the lattice parameters of $(DMET)_2I_3$ and the calculated coherence length anisotropy, we estimate the transfer integral anisotropy to be $t_x : t_y : t_z$ = 194 : 20 : 1. The same anisotropy ratio t_x/t_y = 9.7 was found in this material from the Yoshino angular effect measurements [26].

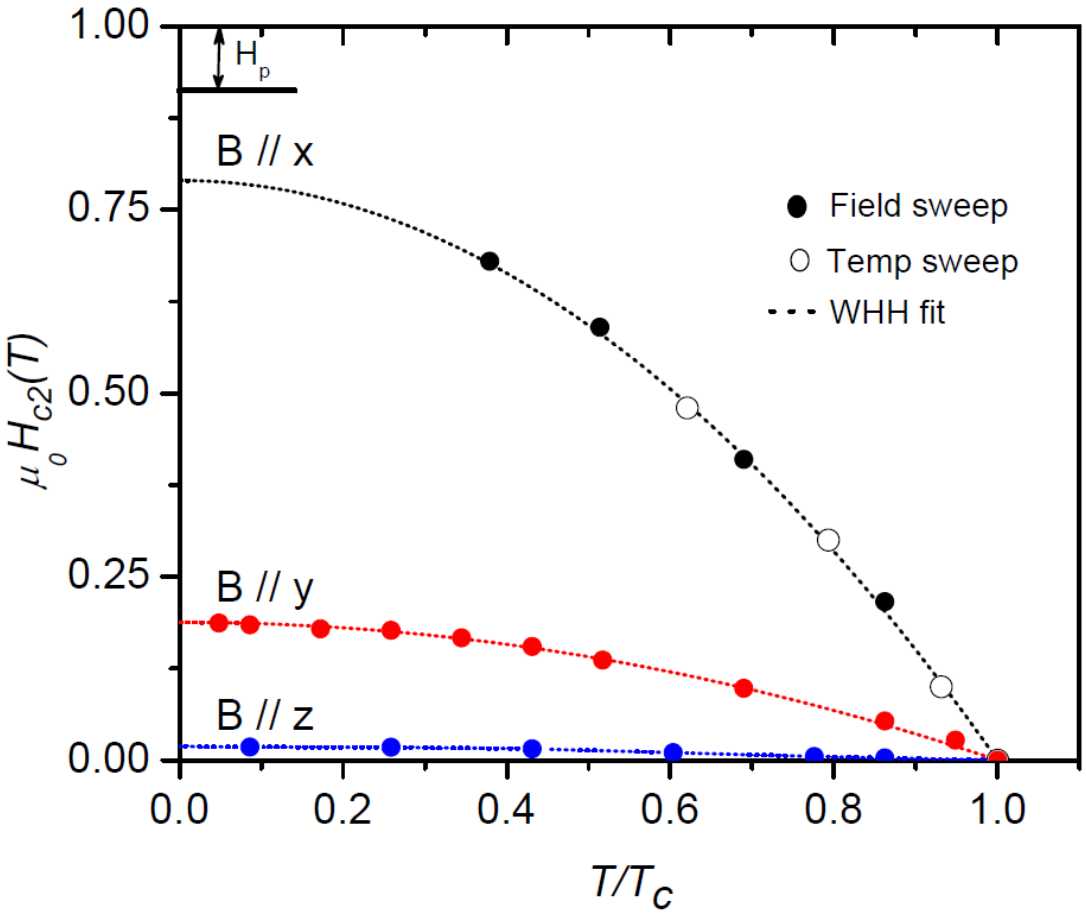

FIG. 5.15 *H-T* phase diagram in $(DMET)_2I_3$ for the field aligned along the *x*, *y*, and *z* axes – direction calculated using midpoint 'M' criterion. The dotted line is calculated using WHH formula. The Pauli paramagnetic limit (H_p) for isotropic *s*-wave pairing and in the absence of strong spin-orbit coupling is estimated to be 0.9 -1 T.

There are two pair breaking effects of magnetic field in superconductivity, of orbital and spin origin. When the interlayer coherence length in a Q1D superconductor is comparable to the interplane distance, *i.e.*, $\xi_z(0) \sim c^*$ at sufficient high magnetic field, FIDC can suppress orbital pair breaking and allow superconductivity to persist. This may be the case in $(TMTSF)_2X$ (X = ClO_4 and PF_6). However, in $(DMET)_2I_3$, the interplane coherence length $\xi_z(0)$ is about four times the 1.55 nm interlayer distance, suggesting that

FIDC does not occur. On the other hand, the spin pair breaking Pauli limit in a 3D system is given by $H_p(T=0) = 1.84T_c(H=0)$ for isotropic s-wave pairing [5.11, 5.12] in the absence of strong spin-orbit coupling, or $1.58T_c(H=0)$ for the case of anisotropic singlet pairing [5.28]. Using the observed superconducting transition temperature, T_c = 0.58 K, H_p becomes 1 T and 0.9 T within these two limits. The extrapolated value of H_{c2} along all three axes is smaller than these calculated values of H_p, as shown in **Fig. 5.15**. Therefore, the upper critical field in $(DMET)_2I_3$ does *not* exceed the paramagnetic limit, in contrast to the case of $(TMTSF)_2X$. Curiously, the nature of superconductivity in $(DMET)_2I_3$, from the viewpoint of H_{c2}, appears to be conventional, quite unlike the isostructural Bechgaard salts.

We have also measured the upper critical field anisotropy within the *y*-*z* plane, between perpendicular and parallel to the conducting plane, at 0.05 K, as shown in **Fig. 5.16**. $H_{c2}(\theta)$ has a sharp peak around the *y*-axis, with an anisotropy $\gamma = \frac{H_{c2}^{//}}{H_{c2}^{\perp}}$ of about 10. This ratio is close to the experimentally-observed value of $\gamma \sim 8$ for $(TMTSF)_2PF_6$ at 0.07 K and $\gamma \sim 17$ at 0.75 K [5.8]. Also, plotted in **Fig. 5.16** are fits to the anisotropic effective-mass G-L theory [5.29] given by

$$\left(\frac{H_{c2}(\theta)\sin\theta}{H_{c2}^{\perp}}\right)^2 + \left(\frac{H_{c2}(\theta)\cos\theta}{H_{c2}^{//}}\right)^2 = 1 \qquad (5.4).$$

Here, $H_{c2}^{\perp}$ and $H_{c2}^{//}$ are the upper critical field perpendicular and parallel to the *x*-*y* plane, respectively. The critical field parameters used for the curve are $H_{c2}^{\perp}$ = 0.019 T and $H_{c2}^{//}$ = 0.186 T. There is fairly good agreement between the data and Eq. (5.4) for field near the *y* and *z*-axes. However, in the *y*-*z* plane the data are skewed from Eq. (5.4). More

measurements may be needed to conclude any further, though it turns out that it is rare to find strong agreement across the full angular regime in highly anisotropic superconductors.

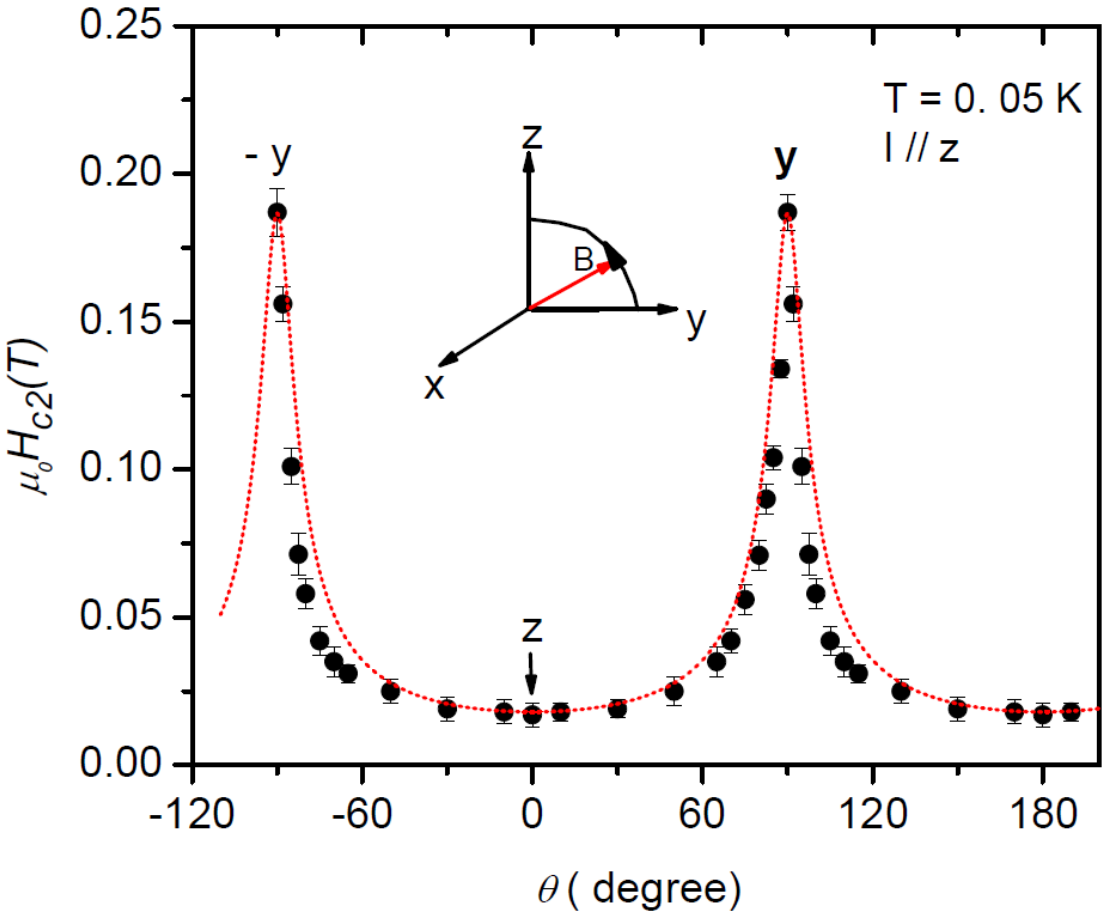

FIG. 5.16 Angular dependence of upper critical fields taken at 0.05 K along the *y*-*z* plane. The dotted line is the fit to anisotropic effective-mass G-L theory.

5.4 Conclusion

The temperature dependence of the upper critical magnetic field $H_{c2}(T)$ of the Q1D molecular organic superconductor $(DMET)_2I_3$ has been measured, along three principle axes *x (b), y (a'),* and *z (c*)*, for the first time. Although $(DMET)_2I_3$ has strong structural and electronic similarity to the $(TMTSF)_2X$ (X = ClO_4, PF_6) system, as well as exhibits all other ground states observed therein, the $H_{c2}(T)$ dependence in $(DMET)_2I_3$ shows conventional G-L saturation at low temperature ($T \ll T_c$). This lead us to conclude that the superconductivity in $(DMET)_2I_3$ is conventional spin singlet, and thus different from the possible triplet superconductivity in the Bechgaard salts. This may motivate future work in the $(TMTSF)_2X$ (X = ClO_4, PF_6) system to fully understand the unconventional behavior seen in upper critical field.

5.5 References

[5.1] D. Jerome, A. Mazaud, M. Ribault, and K. Bechgaard, J. Phys. Lett. **41**, L92 (1980).

[5.2] M. Y. Choi, P. M. Chaikin, S. Z. Haung, P. Hean, E. M. Engler, and R. L. Greene, Phys. Rev. B, **25**, 6208 (1982).

[5.3] M. Takigawa, H. Yasuoka, and G.Saito, J. Phys. Soc. Jpn. **56**, 873 (1987).

[5.4] A. G. Lebed, JETP Lett., **44**, 114, (1986).

[5.5] I. J. Lee, A. P. Hope, M. J. Leone, and M. J. Naughton, Applied Superconductivity, **2**, 10-12, 753 (1994).

[5.6] I. J. Lee, A. P. Hope, M. J. Leone, and M. J. Naughton, Synth. Met. **70**, 747 (1995).

[5.7] I. J. Lee, M. J. Naughton, G. M. Danner, P. Chaikin, Phys. Rev. Lett. **78**, 18, 3555 (1997).

[5.8] I. J. Lee, P. M. Chaikin, and M. J. Naughton, Phys. Rev. B, **65**, 180502 (2002).

[5.9] I. J. Lee, S. E. Brown, W. G. Clark, M. J. Srouse, M. J. Naughton, W. Kang, and P. M. Chaikin, Phys. Rev. Lett. **88**, 017004 (2002).

[5.10] K. Murata, M. Tokumoto, H. Anzai, K. Kajimura, and T. Ishiguro, J. Appl. Phys. **26** Suppl. 26-3, 1367 (1987).

[5.11] A. M. Clogston, Phys. Rev. Lett. **9** 266 (1962).

[5.12] B. S. Chandrasekhar, Appl. Phys. Lett. **1**, 7 (1962).

[5.13] L. I. Burlachkov, L. P. Gor'kov, and A. G. Lebed, Europhys. Lett. **4**, 941 (1987).

[5.14] N. Dupuis, G. Montambaux, and C. A. R. Sa de Melo., Phys.Rev. Lett. **70**, 2613 (1993).

[5.15] N. Dupuis and G. Montambaux, Phys. Rev. B **49**, 8993 (1994).

[5.16] N. Dupuis, Phys. Rev. B **51**, 9074 (1995).

[5.17] J. I. Oh and M. J. Naughton, Phys. Rev. Lett. **92**, 067001 (2004).

[5.18] H. I. Ha, J. I. Oh, J. Moser, and M. J. Naughton, Synth. Met. **137**, 1215 (2003).

[5.19] P. Fulde and R. A. Ferrell, Phys. Rev. **135**, A550 (1964).

[5.20] A. I. Larkin and Y. N. Ovchinnikov, JETP, **20**, 762 (1965).

[5.21] R. Lortz, Y. Wang, A. Deumer, P. H. M. Bottger, B. Bergk, G. Zwicknagl, Y. Nakazawa, and J. Wosnitza, Phys. Rev. Lett. **99,** 187002 (2007).

[5.22] H. A. Radovan, N. A. Fortune, T. P. Murphy, S. T. Hannahs, E. C. Palm, S. W. Tozer, and D. Hall, Nature **425**, 51 (2003).

[5.23] J. Shinagawa, Y. Kurosaki, F. Zhang, C. Parker, S. E. Brown, D. Je´rome, J. B. Christensen, and K. Bechgaard, Phys. Rev. Lett. **98,** 147002 (2007).

[5.24] S. Yonezawa, S. Kusaba, Y. Maeno, P. Auban-Senzier, C. Pasquier, K. Bechgaard, and D. Je´rome, Phys. Rev. Lett. **100,** 117002 (2008).

[25] L. P. Gorkov, and d. Jerome, J. Physique Lett. 46, L643 (1985).

[26] H. Yoshino, K. Saito, H. Nishikawa, K. Kikuchi, K. Kobayashi, and I. Ikemoto., J. Phys. Soc. Jpn. **66**, 2410 (1997).

[5.28] Y. Hasegawa and H. Fukuyama, J. Phys. Soc. Jpn. **56**, 877 (1987).

[5.29] W. E. Lawrence and S. Doniach, in *Proceedings of Twelvth International Conference on Low Temperature Physics*, Kyoto, 1970, edited by E. Kanda (Keigaku, Tokyo, 1971), p. 361.

Chapter 6

Conclusions and Future Works

6.1 Conclusion

Quasi-one-dimensional (Q1D) molecular conductors are highly anisotropic materials which show remarkable oscillatory magnetotransport phenomena with respect to crystal orientation in a strong magnetic field [1 , 2]. Several types of angular magnetoresistance oscillations (AMRO) have been observed in Q1D conductors. In the prototypical Q1D conductors based on the TMTSF molecule, Lebed "magic angle" (LMA) resonances [3,4,5,6,7], Danner-Kang-Chaikin (DKC) oscillations [8, 9] and the Yoshino angular effect (YAE) [10,11,12] have been observed for field rotations about the three principle axes., respectively In addition, more complex "Lee-Naughton" oscillations [13] were observed when the magnetic field was rotated through arbitrary, out-of-plane directions [12,13,14].

While such AMRO effects have been detected in several Q1D materials, their origin(s) and relationships to each other have puzzled researchers for over two decades. For example, while numerical calculations of magnetoconductivity using the Boltzmann transport equation for a Q1D system qualitatively reproduce the observed AMRO [10], several other theoretical models introduced to explain interlayer AMRO in Q1D systems, quasi-classical and quantum [15,16,17,18,19,20,21,22,23,24], qualitatively explain only some of the observed effects (DKC, YAE, and LN). Curiously, these theories have consistently failed to simulate the initially predicted [3,4], and detected [5,6], Lebed effect. The models in Refs. 21-23 result in identical expressions for the interlayer

conductivity, though from slightly different starting assumptions, each yielding a series of resistivity minima for integer values of an index n in the Lebed relation $\tan\theta = n\,a_y / a_z$, where θ is the magnetic field angle between lattice directions a_y and a_z.

According to these models, each n^{th}-order oscillation is modulated by an equivalent order Bessel function that is itself a function of the magnetic field ratio B_x/B_z, x and z being the intrachain and interplane (the most and least conducting) directions, respectively. However, when the field is rotated in the y-z plane (*i.e.* perpendicular to the Q1D chains, x), the presumed optimal situation for the Lebed effect, all Bessel functions vanish, with the exception of $n = 0$, and the resulting resistivity has a smooth, featureless angular variation with field, with *no* Lebed oscillations. In spite of this fact, the Lebed effect has recently been suggested to be the "only fundamental angular effect" [25], with the remaining effects (DKC, YAE, and LN) being simple modulations of this. This seems arguable since, experimentally, Lebed oscillation amplitudes have been anecdotally observed to *decrease* (some becoming immeasurably small) as the field rotation plane approaches the "preferred" y-z plane where, again, the effect is expected to be *strongest* [12, 25].

To date, all available theoretical models [15-26] have employed an orthorhombic or cubic approximation to the actual triclinic crystal structure of the materials in which the AMRO effects have been seen. In this dissertation, we have simulated electrical conductivity via numerical calculations employing the *actual* triclinic lattice parameters of a Q1D conductor, $(DMET)_2I_3$, and measured its interlayer magnetoresistance. We show that all AMRO effects appear in both theory and experiment and, moreover, now match in the Lebed rotation plane with respect to the overall magnetoresistance and the

presence of LMA features, including their still somewhat curious diminishment upon approaching the *y*-*z* plane [27].

Furthermore, we have measured the temperature dependence of the upper critical magnetic field of the quasi-one-dimensional molecular organic superconductor $(DMET)_2I_3$, for magnetic field applied along the intrachain, interchain, and interplane directions. The upper critical field tends to saturation at low temperature for field in all directions and does not exceed the Pauli paramagnetic limit (H_p) in any direction. Superconductivity in $(DMET)_2I_3$ thus appears to be conventional spin singlet, in apparent contrast to the status of the isostructural Bechgaard salts. There, H_{c2} was found to significantly exceed H_p in the in-plane, interchain direction, interpreted as either a signature of spin triplet or an FFLO inhomogeneous singlet state.

The study of several aspects of AMRO and superconductivity in Q1D systems still remains an active area of research. Issues such as the diminishing of the LNL oscillations in the *y*-*z* plane, the non-symmetry of the amplitudes and number of oscillations, the validity of one electron theory in such strongly correlated electron systems, and the curious difference between superconductivity in the closely-related DMET and TMTSF systems are left for future investigations.

6.2 References

[1] T. Ishiguro, K. Yamaji, and G. Saito, *Organic Superconductors*, 2nd Ed. (Springer-Verlag, Berlin, 1998).

[2] *The Physics of Organic Superconductors and Conductors*, Andrei Lebed (Ed.), Springer Series in Materials Science, Vol. 110 (2008).

[3] A. G. Lebed, JETP Lett. **43**, 174 (1986).

[4] A. G. Lebed and P. Bak, Phys. Rev. Lett. **63**, 1315 (1989).

[5] T. Osada *et al.*, Phys. Rev. Lett. **66**, 1525 (1991).

[6] M. J. Naughton, O. H. Chung, M. Chaparala, X. Bu, and P. Coppens, Phys. Rev. Lett. **67**, 3712 (1991); M. J. Naughton, O. H. Chung, L. Y. Chiang, and J. S. Brooks, Mater. Res. Soc. Symp. Proc. **173**, 257 (1990).

[7] W. Kang, S. T. Hannahs, and P. M. Chaikin, Phys. Rev. Lett. **69**, 2827 (1992).

[8] G. M. Danner, W. Kang, and P. M. Chaikin, Phys. Rev. Lett. **72**, 3714 (1994).

[9] I. J. Lee and M. J. Naughton, Phys. Rev. B **58**, R13343 (1998).

[10] T. Osada, S. Kagoshima, and N. Miura, Phys. Rev. Lett. **77**, 5261 (1996).

[11] H. Yoshino *et al.*, J. Phys. Soc. Jpn. **64**, 2307 (1995).

[12] M. J. Naughton, I. J. Lee, P. M. Chaikin, and G. M. Danner, Synth. Met. **85**, 1481 (1997).

[13] I. J. Lee and M. J. Naughton, Phys. Rev. B **57**, 7423 (1998).

[14] H. I. Ha, A. G. Lebed, and M. J. Naughton, Phys. Rev. B **73**, 033107 (2006).

[15] K. Maki, Phys. Rev. B **45**, R5111 (1992).

[16] T. Osada, S. Kagoshima, and N. Miura, Phys. Rev. B **46**, 1812 (1992).

[17] A. G. Lebed, J. Phys. I **4**, 351 (1994).

[18] S. P. Strong, David G. Clarke, and P. W. Anderson, Phys. Rev. Lett. **73**, 1007 (1994).

[19] R. H. McKenzie and P. Moses, Phys. Rev. Lett. **81**, 4492 (1998).

[20] H. Yoshino and K. Murata, J. Phys. Soc. Jpn. **68**, 3027 (1999).

[21] T. Osada, Physica E (Amsterdam) **12**, 272 (2002); T. Osada and M. Kuraguchi, Synthetic Metals, **133-134**, 75 (2003).

[22] B. K. Cooper and V. M. Yakovenko, Phys. Rev. Lett. **96**, 037001 (2006).

[23] A. G. Lebed and M. J. Naughton, Phys. Rev. Lett. **91**, 187003 (2003).

[24] A. G. Lebed, H. I. Ha, and M. J. Naughton, Phys. Rev. B **71**, 132504 (2005).

[25] W. Kang, T. Osada, Y. J. Jo, and H. Kang, Phys. Rev. Lett. **99**, 017002 (2007).

[26] A. G. Lebed, N. N. Bagmet, and M. J. Naughton, Phys. Rev. Lett. **93**, 157006 (2004).

[27] P. Dhakal, H. Yoshino, J. I. Oh, K. Kikuchi, and M. J. Naughton, Phys. Rev. Lett. **105**, 067201 (2010).